Strål
säkerhets
myndigheten
Swedish Radiation Safety Authority

Research

2019:15

3D Thermo-Mechanical Coupled Modelling of Thermo-Seismic Response of a Fractured Rock Mass related to the Final Disposal of Spent Nuclear Fuel and Nuclear Waste in Hard Rock

Report number: 2019:15 **ISSN:** 2000-0456
Available at www.stralsakerhetsmyndigheten.se

SSM perspective

Background

When assessing the long-term safety of a repository for spent nuclear fuel it is important to consider future earthquakes. Previous studies by Yoon et al. (2014, SSM Report 2014:59) and (2016, SSM Report 2016:23) investigated the fracture responses due to heat and earthquakes at major deformation zones using a 2D thermo-mechanical coupled model that uses a Particle Flow Code (PFC2D, Itasca). The 2D approach limits the investigation to horizontal and vertical cross sections of the Forsmark site and the model is not able to handle interactions of steeply dipping and gently dipping faults. Thus, the 2D approach is not capable to address the question if an occurrence of an earthquake at a gently dipping fault, could reactivate some of the large, steeply dipping faults. To explore thermally and/or seismic induced fracture slip of the repository fracture system, this study was performed with 3D thermo-mechanical coupled modelling using Particle Flow Code 3D v4 (PFC3D v4). Importantly, before the 3D thermo-mechanical coupled modelling could be performed, a 3D geological model of the Forsmark site had to be created representing the repository fracture system and relevant deformation zones.

Results

The aim of the research is to explore 3D earthquake simulation and the heat load from the spent nuclear fuel and its potential impact on the repository fracture system. Three scenarios were investigated:

- heating scenario, heat load inducing repository fracture slip
- earthquake scenario, seismic load inducing repository fracture slip
- earthquake scenario under thermal phase.

The simulated impact of the heat generated from the deposited spent nuclear fuel induces slip in the repository fracture system. Further, the fracture dilation during the heating is irreversible.

The scaling parameters of the simulated fault rupture agree well with the earthquake fault empirical scaling relations. Coseismic slip distributions of the activated faults show triangular and asymmetric pattern and sharp increase/drop of displacements at the location of intersection with neighbouring faults. The results show high resemblance to the observations of slip distribution of natural earthquake faults. The results demonstrate that the workflow Yoon et al. developed for simulation of dynamic fault rupture (earthquake event) based on the discrete element model and PFC3D v4 well capture the characteristics of the natural earthquake faults. The performed modelling shows that, under present day stress conditions, the secondary fracture displacement in the repository volume due to seismic loads is more sensitive to the distance where the primary seismic fault occurs than to the size of the primary seismic fault.

The performed modelling also shows that the impact of an earthquake event occurring during the early time of repository heating (50-100 years) amplifies the shear displacements of the repository factures by a factor of 10 to 1000 compared to shear displacements induced by the heat load alone.

Relevance

Canister failure due to shear load is included in SKB's main scenario for the safety case for the planned repository for spent nuclear fuel in Forsmark. Thus, it is important to understand possible causes for shear movements in the repository volume and the response of the canister to these movements. This study explores how:

- repository fracture behaves under the influence of heat loads
- repository fracture behaves under the influence of seismic loads
- repository fracture behaves if an earthquake coincides with the heat load.

Therefore, the study is important for SSM's understanding of shear movements in the repository volume and their impact in the continued review of SKB's application for a spent nuclear fuel repository in Forsmark.

Need for further research

The PFC3D v4 simulations resulted in unexpected large fracture slip in the repository volume compared to the PFC2D simulations. The reason for this needs to be explored in future research. The thermal modelling can potentially be improved by comparing the PFC3D v4 thermal modelling results with published analytical close form solutions. In addition, the far field response to the heating of the repository should be included in future work in order to examine how the heat is dissipated in the model. Further work is also required in the model to define the damage zone and fault core, which were not done in this study. When modelling the fault stability during future glacial cycles, further work is also needed to include the impact from fluid pressure on the fault activation.

Project information

Contact person SSM: Carl-Henrik Pettersson and Flavio Lanaro
Reference: SSM 2014-3668 / 3030045-14

Strål
säkerhets
myndigheten
Swedish Radiation Safety Authority

2019:15

3D Thermo-Mechanical Coupled Modelling of Thermo-Seismic Response of a Fractured Rock Mass related to the Final Disposal of Spent Nuclear Fuel and Nuclear Waste in Hard Rock

Date: September 2019
Report number: 2019:15 **ISSN:** 2000-0456
Available at www.stralsakerhetsmyndigheten.se

Project Final Report

3D Thermo-Mechanical Coupled Modelling of Thermo-Seismic Response of a Fractured Rock Mass related to the Final Disposal of Spent Nuclear Fuel and Nuclear Waste in Hard Rock

Jeoung Seok Yoon, Arno Zang

Helmholtz Centre Potsdam
GFZ German Research Centre for Geosciences
Potsdam, Germany

September 2019

Reference number: SSM2014-3668
Project number: 3030045-14

Contents

Executive Summary

In this numerical modelling research project, we investigated the impacts of possible sources of loading on the safety of the proposed underground repository at Forsmark Sweden for final disposal of spent nuclear fuels.

We discuss three sets of scenarios where the long-term safety of the repository can be affected. Firstly, the heat generated from the canisters containing the spent nuclear fuels is considered and results in repository rock mass expansion, displacement of the repository fractures and possibly reactivation of nearby faults. Secondly, an earthquake event at nearby large deformation zones is considered which generate a seismic loading on the repository rock mass. Thirdly, an earthquake event occurring during the time when the repository rock mass is under heating is considered.

A three-dimensional discrete element modelling code, Particle Flow Code 3D v4 (PFC3D v4) is chosen for the simulation. The code enables modeling of thermo-mechanical coupled process (conductive heat flow, resulting rock expansion and therefore thermal stress) and dynamic fracturing process (seismic wave generated from a rupturing source propagates and attenuates). Moreover, the code enables implementation of discrete fracture network in a heterogeneously modelled rock mass. Therefore, a discrete fracture embedded in the model is also heterogeneously represented. The fault damage zone is mimicked applying smooth joint contacts.

We studied the possible impacts of the heat loading to the repository fracture system. To do so, we developed a thermo-mechanical coupled simulation workflow and conducted two end-member disposal scenarios: deposition of all canisters and closure at the same time, deposition of canisters in panel-by-panel sequence. We studied the possible impacts of the earthquake events (dynamic fault rupture) occurring at large deformation zones near the repository site. To simulate a fault rupture with magnitude close to 6 or larger, we generated a large geological model of Forsmark site where the major deformation zones that are well-known by the site investigation are included and represented heterogeneously. In the earthquake modelling scenarios, the considered time span extends to 70k years from present to take into account of possible changes in the *in-situ* stress field affected by future glaciation and deglaciation. In particular, we studied the impact of nearby gently dipping fault located above the repository rock volume when it ruptures under glaciation and deglaciation periods. Lastly, we studied the impact of a nearby fault rupture during the time of the repository heating.

From the heating scenario, it is found that the repository fracture system undergoes heat induced slip which show rapid increase of those repository fractures located within the repository panel rock volume during 50-100 years. The fracture system located outside the repository panel rock volume then slip slowly after 100 years as the generated heat propagates. We found that the fracture slip is irreversible and we interpret that it is due to dilatational behavior of the fractures that are intersected by one another.

From the earthquake scenario, it is found that the seismic impact to the repository fracture system is large when the steeply dipping deformation zone undergoes strike-slip faulting during the glaciation period. We interpret that it is due to increased anisotropic stress state formed by the fore-bulging effect resulting from an approaching ice cover which lowers the minimum horizontal stress. In case of a rupturing event of a gently dipping fault, the seismic impact to the repository fracture system is more pronounced when a gently dipping fault undergoes reverse faulting during deglaciation period where the ice sheet retreats. We interpret that it is

due to unloading of the overburden stress by ice sheet melting which results in stress state more favorable for reverse faulting. Therefore, climate change can have an impact on the long-term safety of Forsmark repository.

From the earthquake scenario under thermal phase of the repository, it is found that the repository fractures slip less, possible due to the disturbed stress field by the heating.

We studied the source parameters of the simulated fault rupture and compared with empirical scaling relation of natural earthquake faults. It is found that the rupture parameter, e.g. rupture area, moment magnitude and slip, agree well with the empirical scaling relation of natural earthquake faults. Moreover, fault slip distribution undergoing dynamic faulting shows asymmetric and triangular pattern and sharp slip contrast at the location of intersection with neighboring faults as can be observed in natural earthquake faults. This result is in contrast to symmetric fault slip profiles simulated in other studies where the fault is represented as a planar structure embedded in an elastic rock body. The results demonstrate that the workflow we developed for simulation of dynamic fault rupture (earthquake event) on the basis of discrete element model and PFC3D v4 well captures the characteristics and mechanics of the natural earthquake faults.

All the results of earthquake scenarios assume activation of faults that are close to the repository site (hypocenter distance < 5 km from the repository rock volume). It should be noted that the probability of occurrence of earthquake at those faults is very low.

1. Project introduction

1.1. Background

To be able to assess the long term safety of a repository for disposal of radioactive wastes and spent nuclear fuels, it is necessary to consider all possible threats that could impair the physical integrity of the disposal facility. First type of the threat is environmental, which is an earthquake event. The effect of an earthquake relevant to the repository safety is the earthquake induced shear displacement of a rock fracture crossing the deposition borehole containing the nuclear waste canister. Second type of threat is man-made, which is the heat generated from the nuclear wastes. After the nuclear waste canisters are disposed underground, it results in thermal expansion of the repository rock mass and induces shear displacement of the rock fractures crossing the deposition borehole containing the nuclear waste canisters.

It is therefore necessary to estimate the impacts of both the heat (man-made) and earthquake (environmental) that can possibly occur at nearby fault system. To do so, one should rely on a simulation tool that can capture the thermal-mechanical and dynamically coupled processes. Moreover, to be applied to a safety analysis of an underground nuclear waste repository site, the simulation tool should be able to model complex geological system of the site, in particular, heterogeneity of the rock mass and the geological discontinuity system in various scales.

Lately in Sweden in 2011, the Swedish Nuclear Fuel and Waste Management Company (SKB) has submitted an application to the Swedish Government to obtain a construction license for a final repository for spent nuclear fuels at Forsmark. The application is currently under regulatory review by the Swedish Radiation Safety Authority (SSM) and by the Land and Environmental Court (Lanaro et al. 2015).

Yoon et al. (2014, 2016a, 2016b, 2017) have investigated the safety of the Forsmark repository against the heat generated by the disposed spent fuel and the earthquake events occurring at nearby faults by conducting 2D discrete element-fracture dynamic modeling using Particle Flow Code 2D version 4 (PFC2D v4). The key results of the two studies of Yoon et al. (2014, 2016a, 2016b) are summarized in Chapter 2.

In this project, we extend this modelling studies of Yoon et al. (2014, 2016a, 2016b) into a 3D setting. Compared to the previous studies, the model is enlarged in order to investigate the impacts of larger magnitude (Mw >6) earthquakes that may occur at large deformation zones near the Forsmark repository in the next few hundred years and during future glaciation.

To be comparable with previous 2D modelling results, we chose PFC3D v4 instead of PFC v5. The reason for use of a discrete element code is that it is able to simulate rock heterogeneity, complex brittle rock fracturing processes under different source of tectonic loading. Moreover, the discrete element code, PFC3D, has a significant advantage, in particular in our application, that structural complexity of the discontinuities in various scales (m-scale repository fractures and km-scale faults) can be embedded in a discrete element rock model.

1.2. Objectives

The objectives of the project are the followings.

(1) Generate a 3D geological model of Forsmark repository site with heterogeneously represented geological discontinuities;
(2) Investigate the impacts of the heat generated by the spent nuclear fuels to the repository fracture system;
(3) Investigate the impacts of magnitude, M> 6 earthquakes at nearby large deformation zones to the repository fracture system;
(4) Investigate the impacts of glaciation to the earthquake events and to the repository fracture system;
(5) Investigate the combined impact of an earthquake and the heat to the repository fracture system;
(6) Validate the simulated earthquake source parameters against empirical scaling relation of natural earthquake faults.

1.3. Work packages and the structure of the report

To achieve the above objectives, the project is divided into several work packages (WPs) which are the followings.

WP1: Generation of discrete element based 3D geological model of Forsmark repository site with heterogeneously modelled geological discontinuities (deformation zones and repository fracture system);

WP2: Analysis of the response of the repository fracture system induced by thermal loading;

WP3: Analysis of the response of the repository fracture system induced by fault dynamic rupture;

WP4: Analysis of the response of the repository fracture system induced by combined thermal loading and fault dynamic rupture;

WP5: Analysis of the shear displacement of single isolated and intersected fractures that are represented by smooth joint contact model in a discrete bonded particle model.

Chapter 2 summarizes the previous studies conducted by SKB-Posiva and SSM. Chapter 3 reviews seismicity of Sweden. Chapter 4 describes the development of the 3D geological model (WP1). Chapter 5 presents the concept of shear displacement analysis in this study (WP5). Chapter 6 lists the modelling scenarios. Chapter 7 describes the WP2 and compares the results with those of 2D modelling study by Yoon et al. (2016a). Chapter 8 presents the results of WP3 and also compares the results with those of 2D modelling studies by Yoon et al. (2014, 2016a, 2016b, 2017). Chapter 9 presents the results of WP4. In Chapter 10, we discuss several issues related to the comparison between the previous modelling studies and possible uncertainties in the results. Chapter 11 recommends several issues that are recommended for further study. Chapter 12 represents the conclusions of the study.

2. Summary of previous studies

2.1. SKB-Posiva modelling studies

There has been a number of modelling studies investigating the impacts of earthquake events to the repository fractures. The most relevant studies are by Fälth et al. (2010, 2015) for SKB and Posiva (organization responsible for the final disposal of spent nuclear fuel in Finland) where they used 3DEC (Itasca's three-dimensional distinct element code) and investigated the following questions:

- What are the static and dynamic impacts of an earthquake upon nearby fractures in terms of induced shear displacement?
- How does the induced shear displacement correlate to the distance from and the magnitude of the seismic source?

The earthquakes simulated were of reverse faulting type, but the SKB studies did not try to reproduce an expected typical post-glacial faulting event at Forsmark, Oilkiluoto or Laxemar. Instead, input data that control potentially important seismic parameters such as event magnitude and amount of stress drop are varied systematically in generic simulations to cover event ranges that are potentially relevant to the safety assessment.

To simulate an earthquake event, the fault rupture was initiated at a pre-defined location and programmed to propagate outward along the fault plane with a specified rupture velocity until the propagation is arrested at a the rupture area boundary. The models include large numbers of explicitly modelled host rock fractures with varying orientations at different distances from the earthquake fault as shown in Figure 2-1. The coseismic response of these target fractures, i.e. the induced target fracture slip, was the main outputs of their simulations.

The dynamic 3DEC simulations reported by Fälth et al. (2010) are briefly described as follows:

- Earthquakes were simulated on schematic, hypothetical, rectangular fault plane without couplings to the Forsmark site or to any other site.
- The area of the earthquake hosting faults range between 10 and 1000 km^2. In all cases, the entire fault area was activated (rupture area = fault area), and the moment magnitudes (Mw) ranged between 5 and 7.
- Stress fields were defined without couplings to Forsmark site, but were set in reverse faulting stress regime.
- The rupture initiated at the fault centre and programmed to propagate outward along the fault plane with a velocity corresponding (typically 70%) of the shear wave velocity.
- The rupture process was programmed as a controlled strength breakdown.
- Shear displacements on differently oriented 300 m diameter perfectly planar target fractures are analyzed.

They found that, fractures located close to the slipping fault move more than distant fractures. For the smallest distance between the activated fault and the target fractures considered in their models (200 m), the induced fracture slip was found to vary between 0 and 0.112 m, depending on the earthquake parameters (moment magnitude, stress drop, slip velocity etc.) and on the target fracture orientation and position relative to the hypocentre.

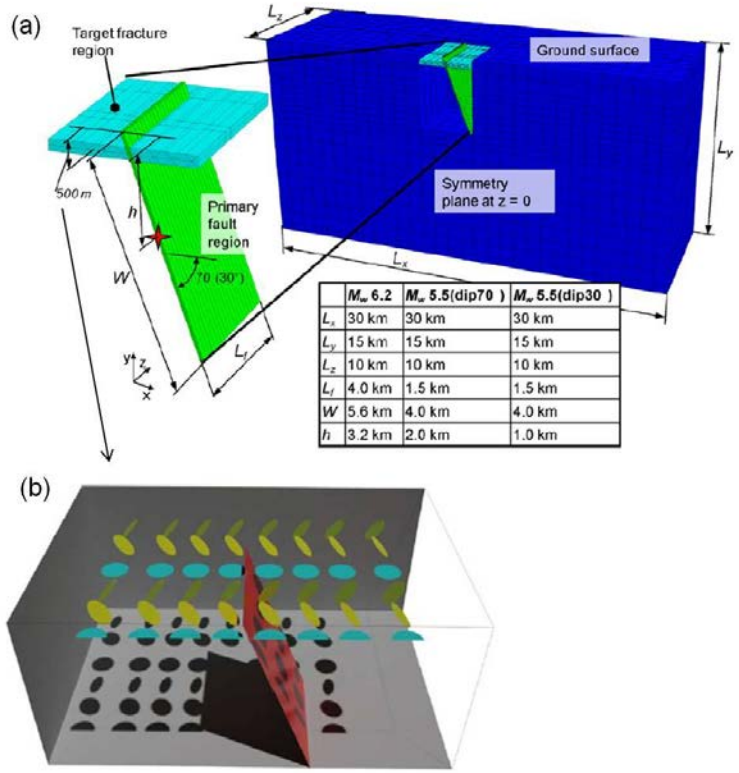

	M_w 6.2	M_w 5.5(dip70)	M_w 5.5(dip30)
L_x	30 km	30 km	30 km
L_y	15 km	15 km	15 km
L_z	10 km	10 km	10 km
L_f	4.0 km	1.5 km	1.5 km
W	5.6 km	4.0 km	4.0 km
h	3.2 km	2.0 km	1.0 km

Figure 2-1. (a) Geometric outlines of 3DEC model and (b) sketch of the circular target fractures located at different locations relative to the primary fault (from Fälth et al. 2010).

2.2. SSM's modelling studies

During the main review phase of the SKB's license application for construction of the final repository for spent nuclear fuel at Forsmark, SSM (Swedish Radiation Safety Authority) conducted a few numerical modelling studies aiming at investigation of the impact of earthquake events and the repository heat to the repository fractures. Those modelling studies used the PFC2D v4.

Yoon et al. (2014) have conducted 2D modelling study addressing one of several scenarios that could impair the physical integrity of the repository. They developed a method to simulate an earthquake event where strain energy stored at the specific fault is suddenly released. Due to two dimensionality of the modelling, those gently dipping faults were not included in the model and the effects of their activation on the shear displacement of the repository fractures could not be investigated. Also, the heat energy input was unrealistically high enough to create Mw> 2 earthquakes by the canister heat, and generate large shear displacement of the repository fractures.

Later, Yoon et al. (2016a) have revised the 2D modelling study. In this study, the heat energy input was properly adjusted to meet the two dimensionality of the model. Also, they investigated in detail the possibility of the effects of numerical artifacts in PFC2D when a planar fracture is represented by a collection of smooth joints, and when those fractures are densely populated and intersecting one another. The results

demonstrated that there is no risk of canister damage by the heat and the earthquake events simulated in the 2D modelling.

The most critical issue to the two previous modelling studies by Yoon et al. (2014, 2016a) is that the complex phenomena that can occur in the repository rock mass containing dense rock fractures in various scales and orientations can be difficult to simplify by the 2D modelling. Moreover, as there are several gently dipping faults near to the repository rock volume, it is necessary to include those in the assessment of the repository safety, which can only be done in a 3D modelling. Also, considering the high complexity of the geological structures at Forsmark, it is also necessary to model the local geology as realistically as possible, including the third dimensionality. These issues motivated this study.

3. Seismicity in Sweden

In this Chapter, we summarize a report by SKB (Bödvarsson et al. 2006) where the risks for future earthquakes in the vicinity of the proposed nuclear waste repository site at Forsmark is evaluated.

3.1. Spatial distribution of seismicity

Sweden is a low seismicity area and the seismic events are unevenly distributed as shown in Figure 3-1. Most earthquakes are observed in the south-west, around Lake Vänern, along the north-east coast and in Norrbotten. South-eastern Sweden is on the contrary relatively inactive. Some large earthquakes (M8) have occurred in Sweden. It is generally agreed that these events are connected to the late stage of previous ice age deglaciation.

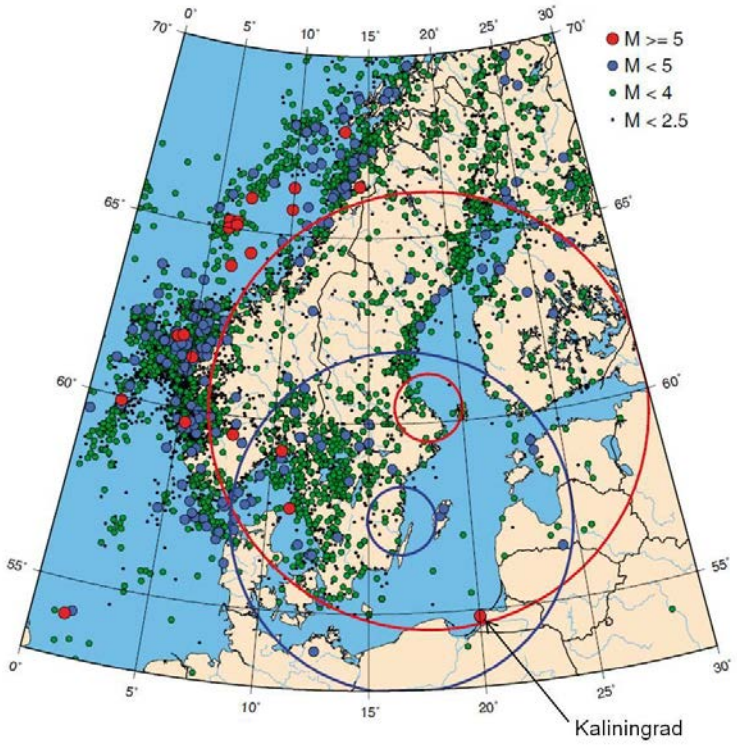

Figure 3-1. Known earthquakes in the Nordic region from 1375 to 2005. The large and small red circle have radius of 650 km and 100 km, respectively, from Forsmark (from Bödvarsson et al. 2006).

3.2. Future earthquake probabilities

Using the catalogue of earthquakes shown in Figure 3-1, Bödvarsson et al. (2006) evaluated occurrence rates of the observed earthquakes. The frequency-magnitude distribution, or Gutenberg-Richter relation, describes the number of events equal to or larger than a certain magnitude in a specific data set. The Gutenberg-Richter

relation is expressed as $logN=a-bM$, where M is the magnitude, N the number of events equal to or larger than magnitude M, 'a' is the intercept and 'b' is approximately 1.

Figure 3-2a shows frequency-magnitude relations of the observed earthquakes for the Forsmark area. The seismic events considered in the frequency-magnitude relation are located within 650 km radius (large red circle in Fig.3-1), to include the Kaliningrad event of 2004 (Fig.3-1). A least square fit to the slope of the frequency-magnitude plot gives the b-value of 0.75 for the SNSN (Swedish National Seismic Network) data (blue line) and 0.97 for the Nordic data (red line). Bödvarsson et al. (2006) evaluated that with approximately one M5 earthquake every 100 years (the Koster islands 1904 and Kaliningrad 2004), one M6 earthquake every 1000 years and one M7 earthquake every 10,000 years are expected.

Bödvarsson et al. (2006) compared the seismicity in the vicinity of the Forsmark area (small red circle in Fig.3-1, 100 km radius) with that in the larger area (large red circle in Fig.3-1). Probabilities of future earthquakes are evaluated using a regression line as shown in Figure 3-2b through the frequency-magnitude distribution and a model for earthquake occurrence to estimate actual probabilities. The regression line slightly over-estimates larger event. The recurrence time for M5 events is 25 years using the model. The recurrence times from the Gutenberg-Richter relation are used to calculate the probability of a certain magnitude event within a certain time period. Bödvarsson et al. (2006) calculated the occurrence probabilities of M5-M7 earthquakes within 650 km, 100 km, and 10 km radius from the Forsmark area. The results are shown in Table 3-1.

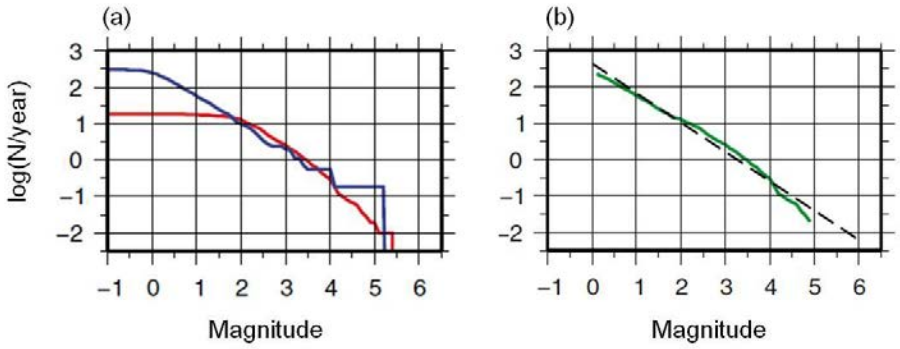

Figure 3-2. (a) Frequency-magnitude relation using number of events per year for the Forsmark area (blue line: SNSN data, red line: Nordic historical data from 1904 to 2005), (b) Frequency-magnitude relation using number of events per year in the 650 km radius around Forsmark (green line: spliced Nordic and SNSN data, dashed black line: maximum likelihood estimate of best fit) (from Bödvarsson et al. 2006).

The results demonstrate that within 100 km around Forsmark the recurrence time for a M5 event is 1,061 years, and the occurrence probability of a M5 event in 1,000 years is 61%. A M6 event is expected to occur in the same time span with a non-trivial probability, 14%. Within 10 km radius from the Forsmark area, the probability of a M5 earthquake drops to 0.94% in a 1,000 years and the probability of a M6 event is 0.15%.

Table 3-1. Occurrence probabilities (%) of M5 and M6 earthquakes within 650 km, 100 km and 10 km radius (R) from the Forsmark repository site (M: magnitude, T: recurrence time, t: exposure time) (modified after Bödvarsson et al. 2006).

R (km)	M	T (year)	t (year)					
			10	20	30	50	100	1000
650	M5	25	32.8	54.9	69.7	86.3	98.1	100
	M6	158	6.1	11.9	17.2	27.1	46.8	99.8
100	M5	1061	0.94	1.87	2.79	4.60	8.99	61.0
	M6	6696	0.15	0.30	0.45	0.74	1.48	13.9
10	M5	106,127	0.01	0.02	0.03	0.05	0.09	0.94
	M6	669,617	0.002	0.003	0.005	0.008	0.01	0.15

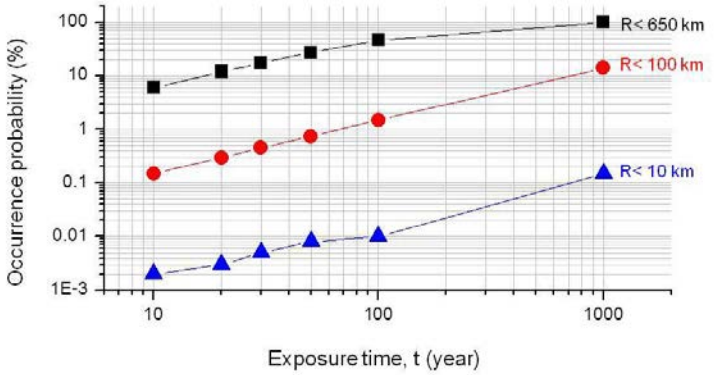

Figure 3-3. Variation in the occurrence probabilities (%) of M6 earthquakes within 650 km (black curve), 100 km (red curve) and 10 km (blue curve) radius from the Forsmark repository site with respect to the exposure time.

3.3. Summary and Discussion

From the analysis of magnitude-frequency distributions of the observed earthquakes, the results demonstrate that the probability of occurrence of M6 earthquake within 10 km radius from the Forsmark area is very low, 0.15% (Table 3-1). However, as pointed out in Bödvarsson et al. (2006), when using an area as small as 10 km range, geological considerations become important. This motivates our study as there are large deformation zones found within 5 km radius with high confidence as shown in Figure 3-4, which all are considered to be unstable (red) under present day stress condition. Therefore, as mentioned earlier in the objectives in Chapter 2, the geological model should be larger than the model presented in Yoon et al. (2014, 2016a, 2016b, 2017) and large enough to contain large deformation zones that can host M6 earthquakes.

During glacial reference cycle (approximately for the next 100k years), it is proposed that the earthquake seismotectonics will change from the interglacial (present) period, glacial period, and deglacial period. The frequency prediction of various earthquake magnitudes done by Bödvarsson et al. (2006) was done using

present seismicity rate, and do not take into consideration of the lower rates predicted during the glacial and higher rates during the deglacial periods (McCalpin 2013). SKB's analysis of future large earthquakes near Forsmark is based on field researches for postglacial faulting in northern Uppland which concluded that there is no evidence for large postglacial earthquakes near the repository, nor associated with the Forsmark, Eckarfjärden, and Singö deformation zones.

However, there is a conflicting conclusion by Mörner (2003, 2004) that Sweden was an area of high to super-high seismic activity at the time of deglaciation. McCalpin (2013) suggested an alternative way to estimate the frequency of M6 and M7 earthquakes in the Forsmark area is to identify evidence of postglacial faulting, such as fault scarps, liquefaction, landslides, and tsunamis. Studies of Mörner (2003, 2004) show that the seismic moment rates during the deglaciation period will be 100 to 1000 times larger than the present ones. If the results of Mörner's study (2003, 2004) are taken into account in the frequency prediction, the occurrence probabilities in Table 3-1 would increase. However, this task is beyond the scope of this study.

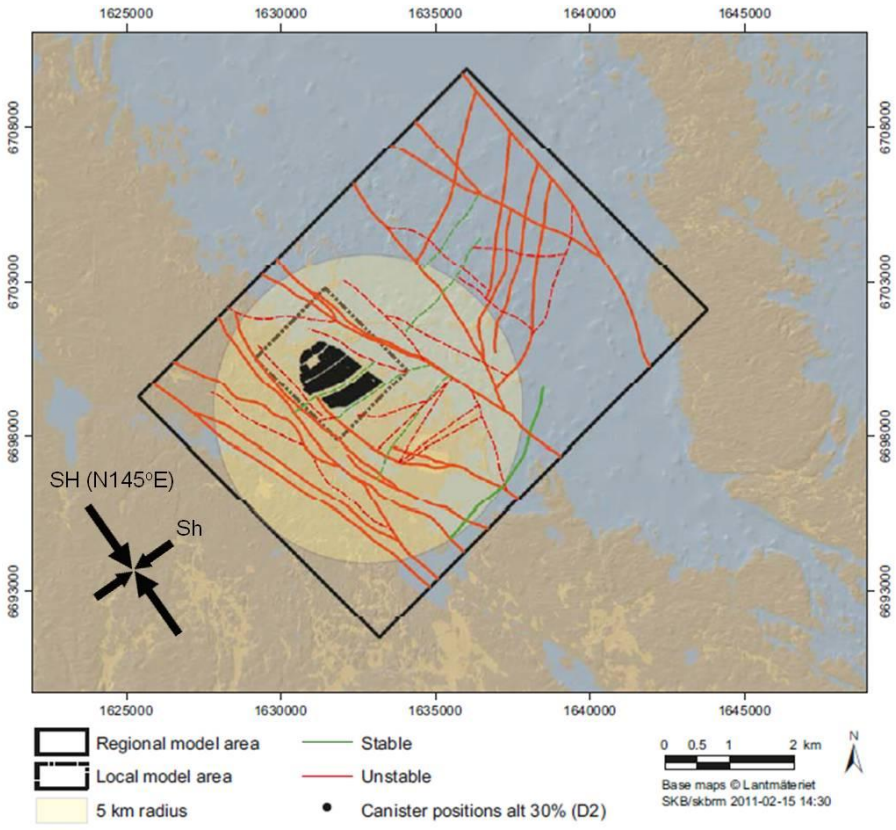

Figure 3-4. Stable and unstable deformation zones at Forsmark and the orientation of maximum and minimum horizontal stresses today at the depth of the repository (modified after SKB 2011).

4. Geological model of Forsmark repository site in 3D

This Chapter describes how the 3D geological models of the Forsmark repository site are developed which contain the geological discontinuities at various scales, e.g. the repository fracture system and the deformation zones (faults).

4.1. Local and Regional Scale Models and the deformation zones

Two models are generated. One is called Local Scale Model (LSM) and the other is called Regional Scale Model (RSM). LSM has similar dimensions as SKB's Local model area as shown in Figure 4-1. RSM has similar length and depth dimensions as SKB's regional model area. Table 4-1 lists the dimensions of the models.

Generating such large models with densely packed particles requires several hundreds of thousands of particles. The simulations require very long computing time and high computing performance. To increase the computing efficiency, we used Adaptive Continuum-DisContinuum (ACDC) method to create 3D geological models of Forsmark repository site. The ACDC method has been used in several other studies, such as Dedecker et al. (2007).

After a densely packed particle assembly is generated, then the geological discontinuities such as deformation zones and the repository fractures (Section 4.2) are embedded in the model. The deformation zones included in the LSM and the RSM are different in terms of their size. The LSM contains layout-determining deformation zones in SKB's Local Model Volume (LMV) as show in Figure 4-2a. The geometrical data of the deformation zones are extracted from the SKB's deterministic fault model and properly converted for implementation in the discrete element model as shown in Figures 4-3 and 4-4.

Due to significantly larger size of the particles in the RSM compared to those used in the LSM (see Table 4-1), only the large deformation zones shown in Figure 4-2b are included in the RSM in order to maintain proper resolution in the representation of the deformation zones. These large deformation zones are: ZFMWNW0001, ZFMNW0003, ZFMWNW0004, ZFMA1, ZFMA2, ZFMA3, which surround the repository site and are large enough to host M> 6 earthquake events.

Figures 4-3 and 4-4 are the top views of the 3D geological models of Forsmark repository site in different scales. The two sets of arrows indicate the orientations of the in situ maximum (SH) and minimum (Sh) horizontal stresses at the repository depth. The traces of the deformation zones and the fractures systems are shown in blue and red, respectively. The geological discontinuities are represented by the smooth joint contact model (Mas Ivars et al. 2011) which is described in more detail in Chapter 5. The discrete element model is generated bigger than the size of the SKB's LMV and RMV in order to implement energy absorbing boundary condition to the particles located outside the bounding boxes. This is described in Section 4.4.

In this report, deformation zones that are embedded in the LSM are called layout-determining deformation zones since they affect the geometry of a waste emplacement panels. The deformation zones that are embedded in the LSM and the RSM are listed in Table 4-2. The gently dipping deformation zones (ZFMA1, ZFMA2, ZFMA3) are not embedded in the 2D Forsmark modelling (Yoon et al.

2014, 2016a, 2016b, 2017). The surface trace length of the deformation zones ZFMA1, ZFMA2, and ZFMA3 are not given as they do not intersect the surface.

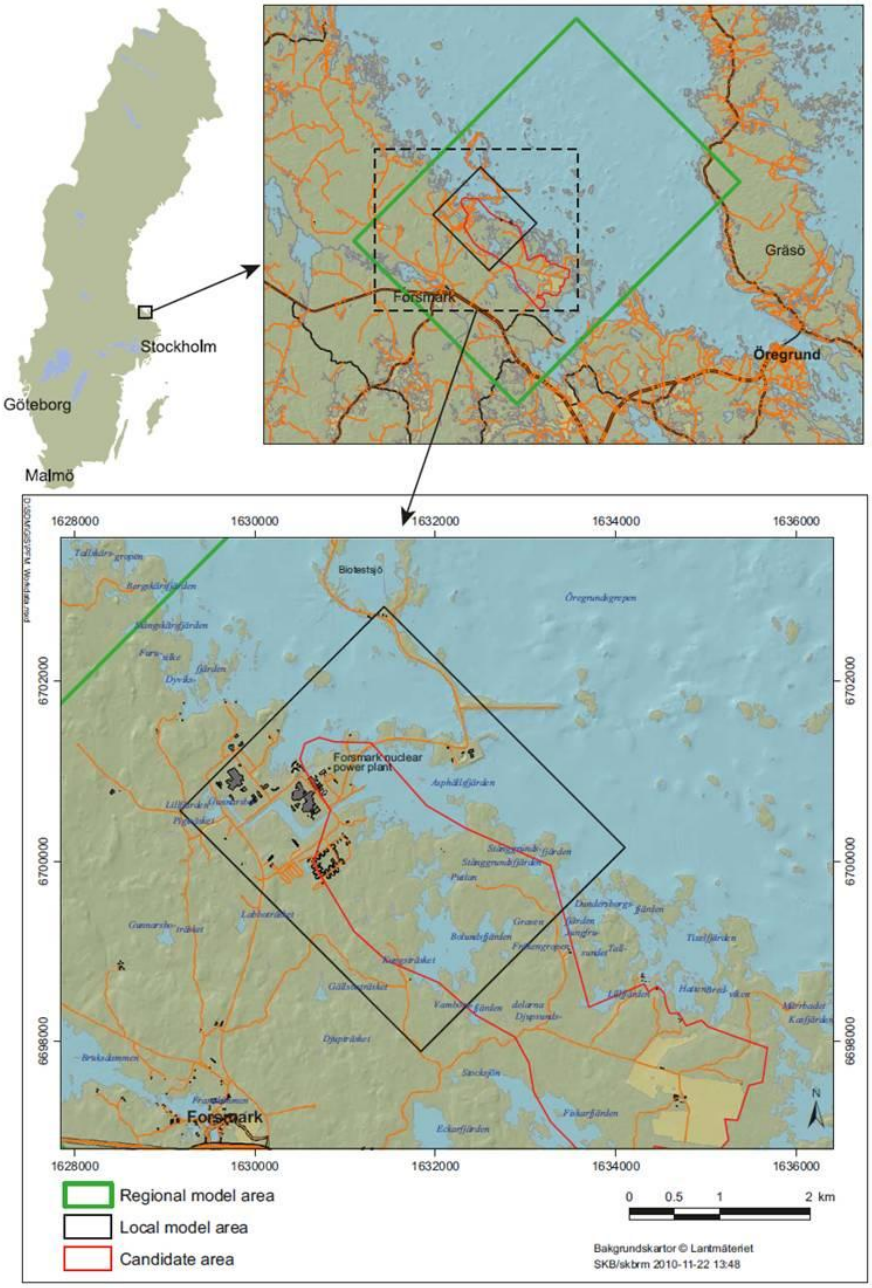

Figure 4-1. Location of the Forsmark candidate area (red) for site investigation and the Local and Regional model areas according to SKB (2011).

Table 4-1. Information of the 3D PFC numerical models.

Descriptions	LSM (Fig.4-3)	RSM (Fig.4-4)
Length x Width x Depth (km)	6.6 x 6.0 x 2.4	16.5 x 13.5 x 2.25
Average particle diameter (m)	33	104
Minimum particle diameter (m)	25	80
Number of particle	421,616	548,739
1 ACDC cell size (m) in x,y,z	600 x 600 x 600	1500 x 1500 x 750
Number of cells in x,y,z directions	11, 10, 4	11, 9, 3

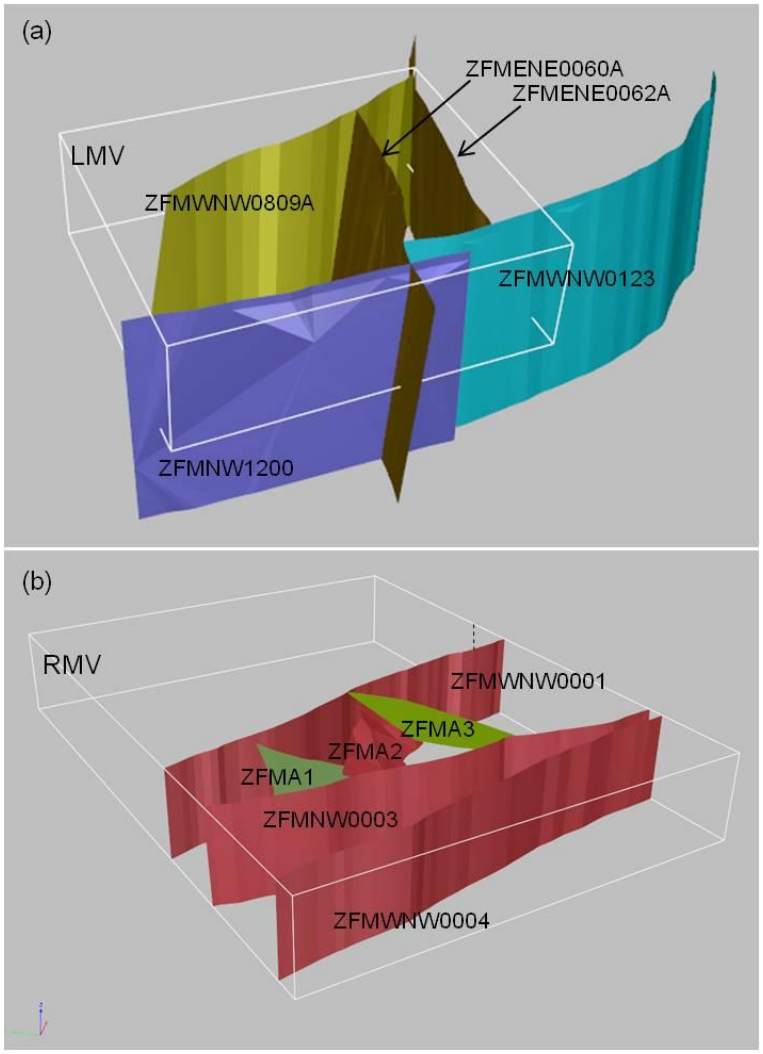

Figure 4-2. SKB's (a) Local Model Volume (LMV) and (b) Regional Model Volume (RMV) and the deformation zones to be embedded in the PFC3D models.

Table 4-2. Modelled surface areas of the deformation zones embedded in the Local and Regional Scale Models and the field observations data (surface trace length, width, strike and dip) of the deformation zones compiled by SKB (Stephens et al. 2007).

Deformation zones	Modelled surface area (km^2)	Surface trace length (m)	Strike (deg)	Dip (deg)
Local Scale Model				
ZFMWNW0123	5.11	5,086	117	82
ZFMENE0062A	8.74	3,543	058	85
ZFMWNW0809A	11.42	3,347	116	90
ZFMENE0060A	8.42	3,120	239	85
ZFMNW1200	10.69	3,121	138	85
Regional Scale Model				
ZFMA1	38.36	NA	082	45
ZFMA2	18.34	NA	080	24
ZFMA3	31.48	NA	046	22
ZFMWNW0001 (Singö)	55.14	30,000	120	90
ZFMNW0003 (Eckarfjärden)	55.87	30,000	139	85
ZFMWNW0004 (Forsmark)	52.80	70,000	125	90

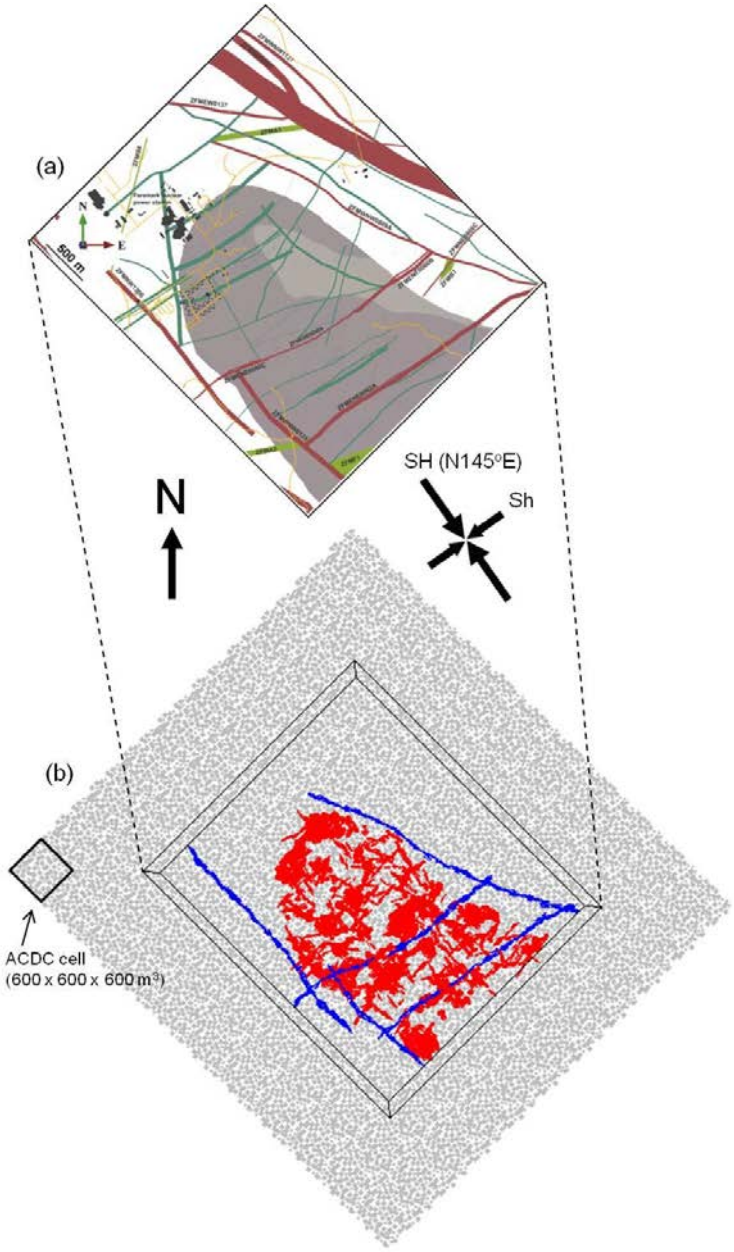

Figure 4-3. (a) Integrated geological model showing the deformation zones (Stephens et al. 2015, gray region: repository rock volume, red: steeply dipping or vertical deformation zones with surface trace length > 3 km, dark-green: steeply dipping or vertical deformation zones with surface trace length < 3km, green: gently dipping deformation zones) and (b) Local Scale Model (LSM) containing the deformation zones and the fracture system represented by the smooth joints (red: repository fractures, blue: deformation zones, grey: particles) at the repository depth.

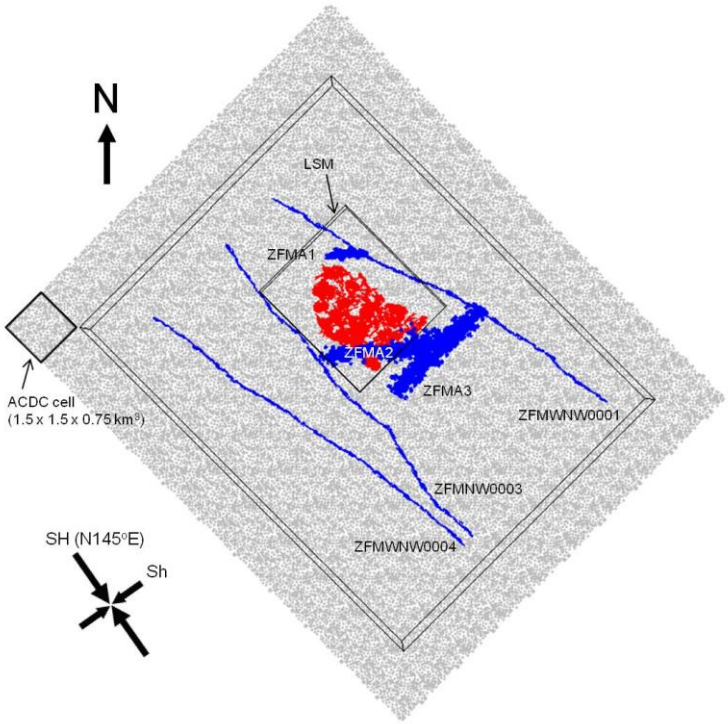

Figure 4-4. Regional Scale Model (RMS) containing the large deformation zones and the repository fractures represented by the smooth joints (red: repository fractures, blue: deformation zones, gray: particles) at the repository depth.

4.2. Repository discrete fracture system

Natural pre-existing fractures in the repository rock mass are implemented as Discrete Fracture Network (DFN) and embedded in the models. The DFNs are stochastically generated (Fig.4-5a) within the repository rock volume (grey shaded region in Fig.4-3a). The DFN model used in the 2D modelling studies by Yoon et al. (2014, 2016a, 2016b, 2017) (Fig.4-5b) is the trace of the 3D DFN at the repository depth.

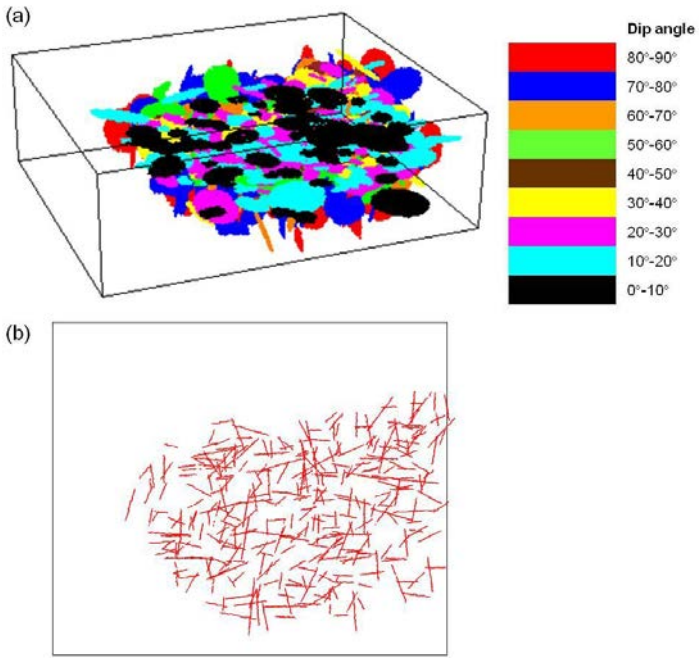

Figure 4-5. (a) Stochastically generated DFN realization within the repository rock volume and (b) DFN traces at the depth of the repository in the 2D modelling of Yoon et al. (2014, 2016a, 2016b, 2017).

The fractures that are stochastically generated by the DFN generator are planar disks (Fig. 4-5a). However, unlike in other modelling codes (e.g. UDEC, 3DEC, Fracod2D), when a planar fracture is embedded in a PFC discrete element model, the fracture is represented by a collection of smooth joints as shown in Figure 4-6 (Mas Ivars et al. 2011). In such case, the smooth joints overlap one another. Due to this irregular structural, fracture properties are adjusted, which is done in two steps as described below.

In the step 1, the size effect of the fracture is taken into consideration. This is necessary as the fracture size implemented in the models range from 200 m to 600 m and the fracture properties are often obtained by laboratory tests. The calibration is done by using the diagram shown in Figure 4-7 (modified after Morris et al. 2013), where the laboratory test obtained fracture stiffness (normal and shear) of a laboratory sample (size 10-30 cm) are properly lowered to a level that can represent fractures at several hundred meters scale at a normal stress of 1 and 10 MPa.

$$K_n\left(\frac{\mathrm{MPa}}{\mathrm{mm}}\right) = 7420 * L(\mathrm{cm})^{-0.631} \qquad \text{Equation (4-1)}$$

For Step 2 calibration, we used the calibration procedure suggested by Itasca (Mas Ivars and Bouzeran 2013) that relates the theoretical size of a disk fracture and the actual size of the fracture when represented by a collection of smooth joints. The idea is that all the area-dependent micro-properties (normal stiffness and shear stiffness, cohesion and tensile strength) of each smooth joint contact have to be calibrated in order to reproduce the desired macro property at the discontinuity plane scale. We considered two types of discontinuity area:

- The “theoretical discontinuity area”, A_{th}: the discontinuity geometrical area, Equation (4-2).
- The “real discontinuity area”, A_{real}: the sum of local area of the *n* smooth joint contacts composing the discontinuity plane, Equation (4-3).
- The ratio between the two, A_{ratio}, Equation (4-4).

$$A_{th} = \pi r_f^2 \qquad \text{Equation (4-2)}$$

$$A_{real} = \sum_{i=1}^{n} sj_A(i) \qquad \text{Equation (4-3)}$$

$$A_{ratio} = {}^{A_{real}}/_{A_{th}} \qquad \text{Equation (4-4)}$$

where, r_f is the repository fracture radius and $sj_A(i)$ is the area of the i-th smooth joint.

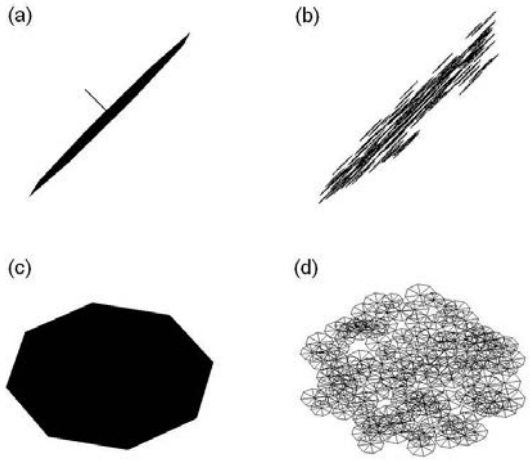

Figure 4-6. Disk fracture (side view: a, front view: c) and representation by a collection of smooth joints (side view: b, front view: d).

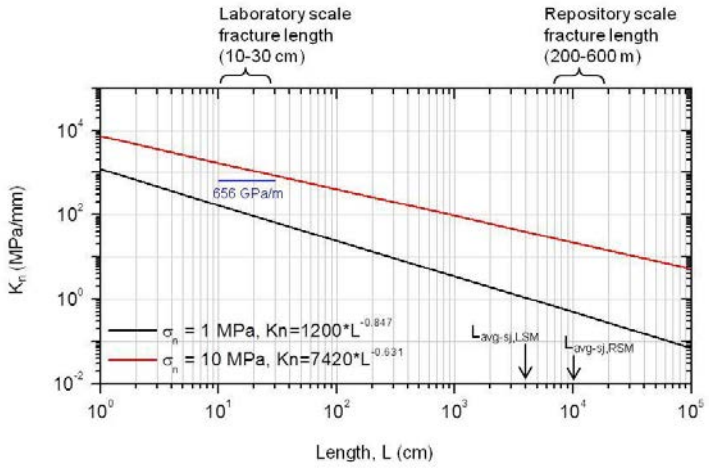

Figure 4-7. Fracture length (cm) and normal stiffness Kn (MPa/mm) relations under 1 MPa (red) and 10 MPa (black) normal stress conditions used for the Step 1 calibration.

The properties of the fractures and the deformation zones are listed in Table 4-3. In both 2D and 3D models, the discontinuity planes are formed by numerous smooth joint contacts that are overlapping. Therefore, usually, A_{real} is larger than A_{th}. The area ratio A_{ratio}, is used for calibration of the mechanical properties as shown in Table 4-4.

Table 4-3. Mechanical properties of the repository fractures (from Hökmark et al. 2010) and the deformation zones (from Glamheden et al. 2007).

Mechanical properties	Repository fractures	Deformation zones
Normal stiffness, Kn (MPa/m)	656e3	200e0
Shear stiffness, Ks (MPa/m)	34e3	15e0
Friction coefficient, tan(°)	0.6*	0.6*
Dilation angle, ψ (°)	3.2	0.0
Tensile strength, σ_t (Pa)	0.1e6	0.1e6
Cohesion, c (Pa)	0.5e6	0.4e6
Friction angle, ϕ (°)	35.8	31.5

* Assumed

Table 4-4. Calibration of macro properties of the fractures using A_{ratio}.

Mechanical properties	Macro properties	Micro properties
Normal stiffness, Kn (Pa/m)	Kn,macro	Kn,macro/A_{ratio}
Shear stiffness, Ks (Pa/m)	Ks,macro	Ks,macro/A_{ratio}
Friction coefficient, tan(°)	-	-
Dilation angle, ψ (°)	-	-
Tensile strength, σ_t (Pa)	σ_t,macro	σ_t,macro/A_{ratio}
Cohesion, c (Pa)	c,macro	c,macro/A_{ratio}
Friction angle, ϕ (°)	-	-

Due to difference in the particle size used in the LSM and in the RSM, the mechanical parameters of the smooth joints that represent the repository fractures and the deformation zones are adjusted differently. Table 4-5 lists the mechanical properties of the smooth joints that are calibrated through Step 1 and Step 2 calibrations for the repository fractures in the LSM and in the RSM, respectively.

Table 4-5. Mechanical properties of the repository fractures and of smooth joints in the LSM models that are calibrated in two steps.

Parameters	Repository fracture	Step 1 Calibration	Step 2 Calibration
Local Scale Model			
Kn (MPa/m)	656e3	39.6e3	22.0e3
Ks (MPa/m)	34e3	2.05e3[1)]	1.14e3
μ (-)	0.6	0.6	0.6
ψ (°)	3.2	3.2	3.2
σ_t (Pa)	0.1e6	0.1e6	0.06e6
c (Pa)	0.5e6	0.5e6	0.28e6
ϕ (°)	35.8	35.8	35.8
Regional Scale Model			
Kn (Pa/m)	656e9	22.2e9	13.2e9
Ks (Pa/m)	34e9	1.15e9*	0.69e9
μ (-)	0.6	0.6	0.6
ψ (°)	3.2	3.2	3.2
σ_t (Pa)	0.1e6	0.1e6	0.06e6
c (Pa)	0.5e6	0.5e6	0.28e6
ϕ (°)	35.8	35.8	35.8

* The shear stiffness, Ks, is also reduced by three orders of magnitude as an approximation.

4.3. Repository panels

The heat generated from the canisters containing the spent nuclear fuel affects the repository rock and the fractures. In the 2D modelling (Yoon et al. 2016a), the thermal power curve of a full size canister provided by SKB (Fig.4-8, black curve) was modified to meet the two dimensionality of the modelling condition (Fig.4-8, red curve).

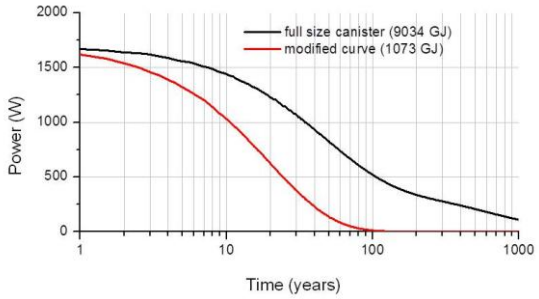

Figure 4-8. Thermal power curve of a full size canister according to SKB (black curve) and the modified one for the PFC2D modelling (red curve).

In the 3D modelling, we use the full size canister thermal power curve (black in Fig. 4-8 and Equation (4-5)). Also, instead of using point heat source as done in the 2D modelling, we used plane heat sources by taking into account the distance between the deposition holes (Px) and the deposition tunnels (Py) as shown in Equation (4-6). The thermal power is then applied to the groups of particles at the locations of the panels.

$$f(t) = \sum_{i=1}^{7} a_i \exp(-t/t_i) \qquad \text{Equation (4-5)}$$

$$q = \frac{Q}{Px.Py} f(t) \qquad \text{Equation (4-6)}$$

where, f(t) defines the decay of the heat and the parameters a_i and t_i are found in Hökmark et al. (2010).

Heat power assigned to the particles at panel locations is also calibrated. In the 2D modelling, the group of particles at panel locations were treated as a collection of point heat sources and adjusted properly with scaling factors. The scaling factors were introduced in order to take into consideration of the size difference between the particles and the deposition holes (Yoon et al. 2016a).

In the 3D modelling, we take into account the areas of the panels (Fig.4-9a and Table 4-6) and treat the panels as plane heat source similarly to Claesson and Probert (1997) and Probert and Claesson (1997) (Fig.4-9b). Therefore, the thermal power input we used is in a form of flux with unit of W/m^2 and takes into consideration of full power of the canister (Q = 1700 W), the deposition hole spacing (Px = 6 m) and the deposition tunnel spacing (Py = 40 m). Using Equation (4-6), the panel area (Table 4-6) is multiplied and assigned to the groups of particles acting as heat generating panels. However, due to the fact that the heat source of a plane panel (with unit of m^2) is assigned to a group of particles, a reduction factor is

introduced to properly adjust the over-estimated heat power. The reduction factor is calculated from the theoretical panel plane area and the sum of surface area of the particles to which heat power is input. Therefore, the final form of heat input assigned to the particles is given in Equation (4-7):

$$q = pan * \frac{Q}{Px.Py} f(t) \qquad \text{Equation (4-7)}$$

where, 'pan' is geometrical area of the panels listed in Table 4-6.

To check if the heat power input is properly calibrated, we perform a heat loading test where the panels are heated simultaneously. In this test the thermal evolution modelling is done in thermal condition only, i.e. without coupling to mechanical analysis. The distribution of the temperature increase at 50 and 200 years after start of heat release are shown in Figure 4-10.

The results we obtained are lower than what is found in Hökmark et al. (2010) where the highest temperature increase at the centre of Panel A is 28 degrees at 50 years and 20 degrees at 200 years.

Table 4-6. Geometrical surface areas of the repository panels (plane heat sources in Fig. 4-9a).

	Geometrical area (km^2)
Panel A	0.098
Panel B	0.489
Panel C	0.797
Panel D	0.601

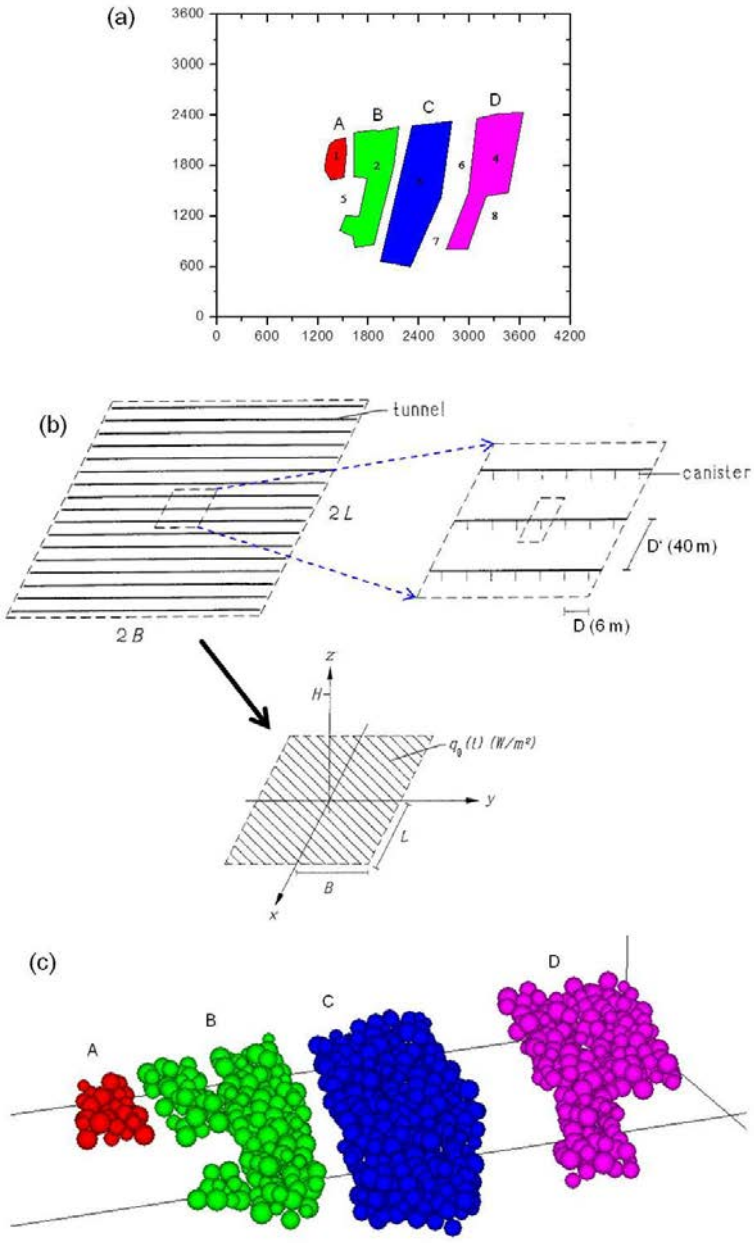

Figure 4-9. **(a)** Repository panels treated as plane heat sources, (b) rectangular plane heat source model of Claesson and Probert (1997), and (c) particles constructing the panels and treated as volume heat sources.

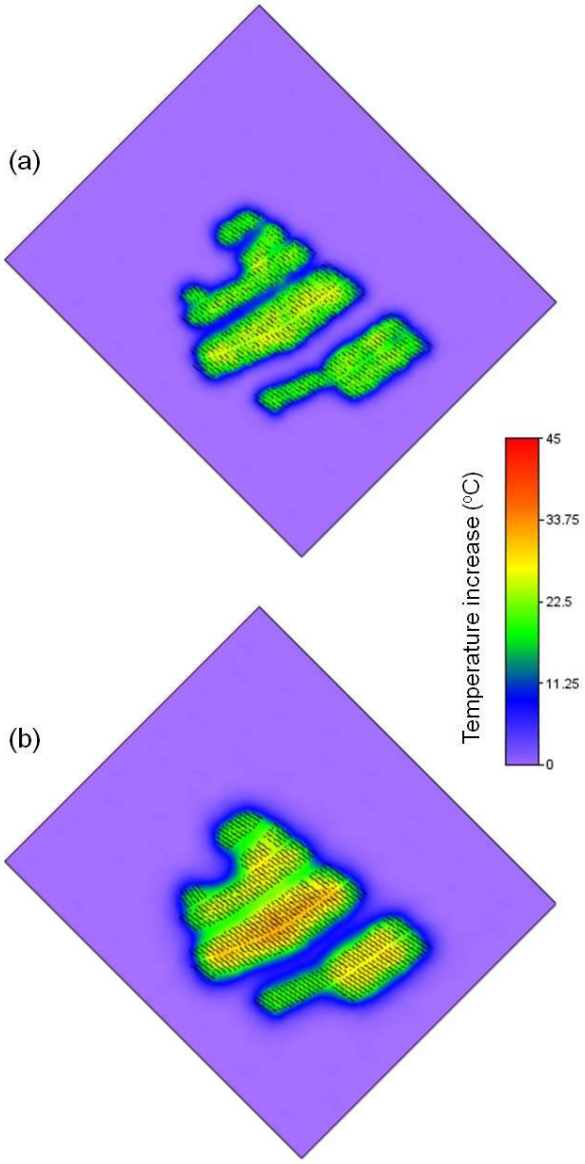

Figure 4-10. Distribution of rock temperature increase obtained in the PFC3D model (a) 50 years and (b) 200 years at the depth of the repository after start of simultaneous panel heating.

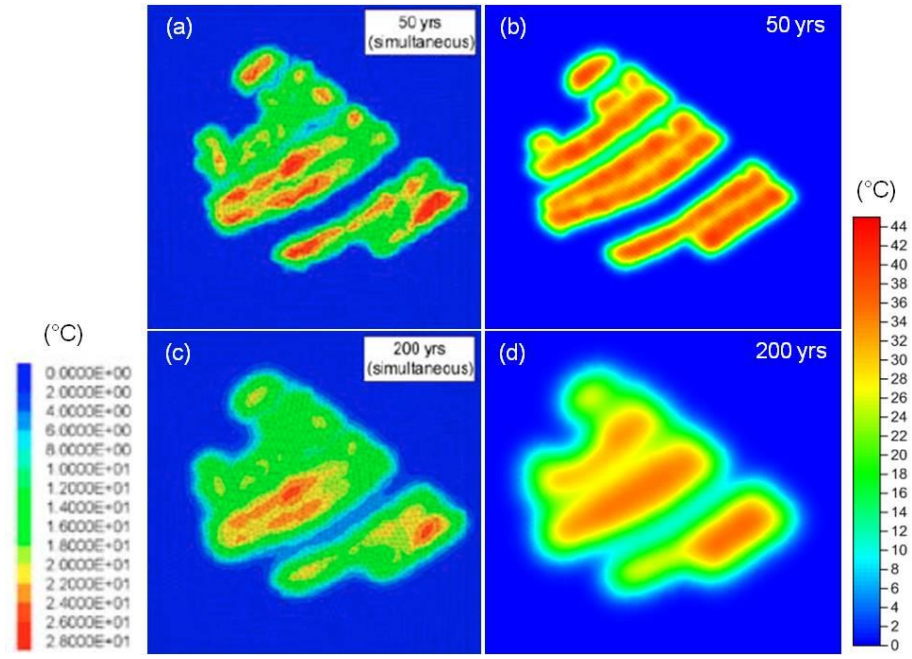

Figure 4-11. Distribution of rock temperature increase simulated in 3DEC modelling (left figures) by Hökmark et al. (2010) and in PFC2D modelling (right figures) by Yoon et al. (2016a) at (a) 50 years and (b) 200 years after start of simultaneous panel heating.

4.4. *In-situ* stress and its evolution during glaciation

Three *in-situ* stress fields are used for different modelling cases. The reverse faulting stress field is defined as present day most likely stress model "Stress Model 1, S1" where the maximum horizontal stress (SH) is 40 MPa, the minimum horizontal stress (Sh) is 22 MPa and the vertical stress (Sv) is 13 MPa at the repository depth (Martin 2007). Considering the pore fluid pressure at repository depth, ca. 5 MPa at 500 m, the resulting effective stresses at the repository depth are 35, 17, and 8 MPa, for SH, Sh, and Sv, respectively (Fig.4-12).

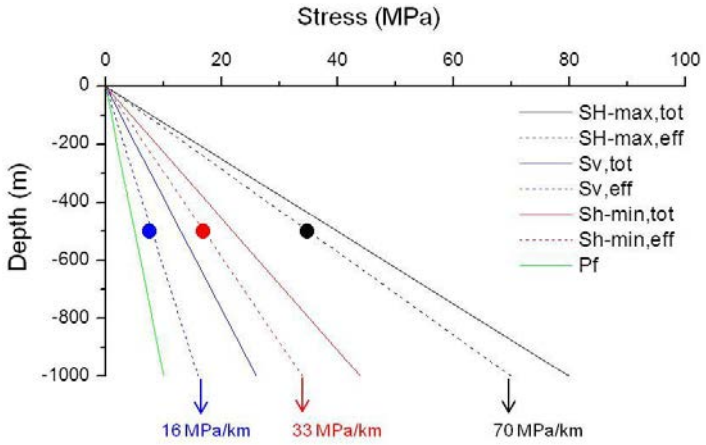

Figure 4-12. Depth variation of the in situ stresses (total and effective) of the present day most likely stress model (S1) and the values (dots) at the depth of the repository.

The *in-situ* stress fields that might evolve during next glacial cycle (time up to 70k years from present) are based on a reconstruction of the Weichselian glaciations (Lund et al. 2009). Figure 4-13 is used where the glacially induced changes of the *in-situ* stress components are read from the curves and added to the *in-situ* stress components of present day stress model. Table 4-7 lists the magnitudes of each *in-situ* stress components of the stress models: (i) S1: Present day most likely stress model (Martin 2007); (ii) S2: Glacially induced stress model in relation to forebulge in front of the ice cover (glaciations); (iii) S3: Stress model in relation to the ice cover retreat (deglaciation). Also, the ratios between the effective stresses are presented, which are used for choosing which fault should be activated in the earthquake simulations. In the ice forebulge stress model (S2), the ratio of principal horizontal stresses (SH'/Sh') becomes larger than that of the present day stress model (S1). This is due to the effect of forebulge induced by the extension of the side of the ice cover, which consequently lowers the minimum horizontal stress (-5 MPa). In such stress condition, some steeply dipping faults are destabilized rather than those gently dipping. Therefore, as it will be discussed in Chapter 6, the large steeply dipping faults are chosen to be activated in the earthquake simulations. In the ice cover retreat stress model (S3), the ratio of horizontal and vertical stresses (SH'/Sv' and Sh'/Sv') increase significantly. In such stress condition, the gently dipping faults are more sensitive to destabilization.

We assumed that the increments of the stress components in Figure 4-13 and Table 4-7 are oriented parallel to the principal stress directions of the present day stress model. However, it should be noted that, at the time of deglaciation with remarkably high seismicity, the glacial isostatic processes could lead to a totally new geodynamic regime; new horizontal stress direction (Mörner 2004). This issue is discussed later.

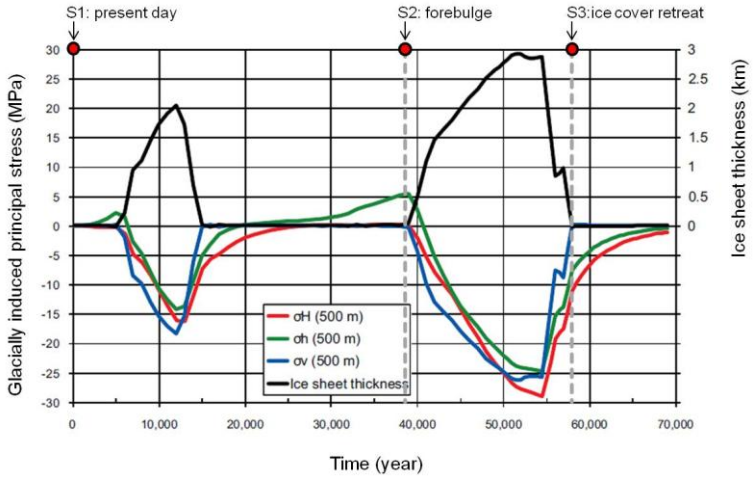

Figure 4-13. Glacially induced increments of the principal stresses at the repository depth during the Weichselian glaciation (modified after Hökmark et al. 2010).

Table 4-7. *In-situ* stresses of the stress model at the depth of the repository: Present day most likely stress model (S1), Glacially induced stress model by ice cover forebulge (S2), Stress model induced by ice cover retreat (S3).

Stresses (MPa)		Stress models		
		S1: present day	S2: forebulge by ice cover	S3: ice cover retreat
Stress increments	ΔSH	0	0	+11
	ΔSh	0	-5	+7
	ΔSv	0	0	0
Target effective stresses	SH’	35	35	46
	Sh’	17	12	24
	Sv’	8	8	8
Simulated stresses (relative difference,%)	SH’	33.7 (3.7%)	34.4 (1.7%)	42.5 (6.2%)
	Sh’	17.1 (0.6%)	12.7 (5.8%)	22.4 (6.7%)
	Sv’	8.3 (3.8%)	8.4 (5.0%)	7.8 (2.5%)
Stress ratios	SH’/Sh’	2.0	2.7	1.9
	SH’/Sv’	4.1	4.1	5.4
	Sh’/Sv’	2.1	1.5	2.9
k = (SH’+Sh’)/2Sv’		3.1	2.8	4.2

4.5. Dynamic fault rupture

To simulate a fault rupture and an earthquake event, we used the method developed in Yoon et al. (2014, 2016a, 2016b, 2017) where the deformation of the particle contacts (smooth joint contacts) along the earthquake hosting fault is locked during the initial *in-situ* stress loading of the model (Step 1 – Locking). In this way, the strain energy from the loading accumulates at the smooth joints of the deformation zone. The strain energy is then released by instantaneously unlocking the particle contacts (smooth joint contact) of the deformation zone (Step 2 – Unlocking), which results in generation of a seismic wave. The seismic wave then travels through the model, and at the same time attenuates due to the damping in the model (Step 3 – Propagation & Attenuation). We confirmed, in the 2D modelling of a single fault trace dynamic rupture simulation, that a seismic wave is generated from the ruptured fault trace and propagate and attenuates. Also by monitoring the temporal evolution of the stresses at several particles from the ruptured trace, we confirmed that the modelling can also simulate transfer of dynamic and static stresses, similar to a natural earthquake faulting (Belardinelli et al. 1999).

To prevent seismic wave reflection from model boundaries, the following procedure is developed. Figure 4-14 and Figure 4-15 show the Multiple Damped Layers (MDL) located outside the Local Scale Model and the Regional Scale Model, respectively. The MDL concept is developed and implemented in the model in order to simulate energy absorption by the far-field. This measure is taken in order to absorb, as much as possible, the seismic waves both in high and low frequencies that could be reflected back after reaching the model boundaries. Several tests were made to optimize the combination of the relevant parameters, such as, number of MDL, layer thickness, and the damping coefficient of the particles in each MDL that can effectively mitigate the effect of reflecting wave.

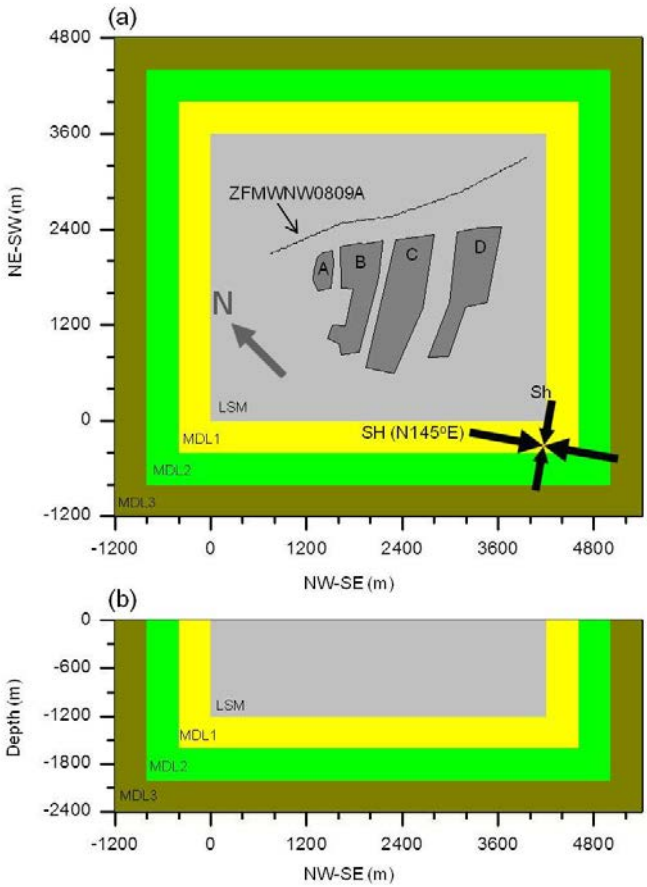

Figure 4-14. (a) Top view and (b) side view of the Local Scale Model with Multiple Damped Layers (MDL). Trace of ZFMWNW0809A is shown in the top view for reference.

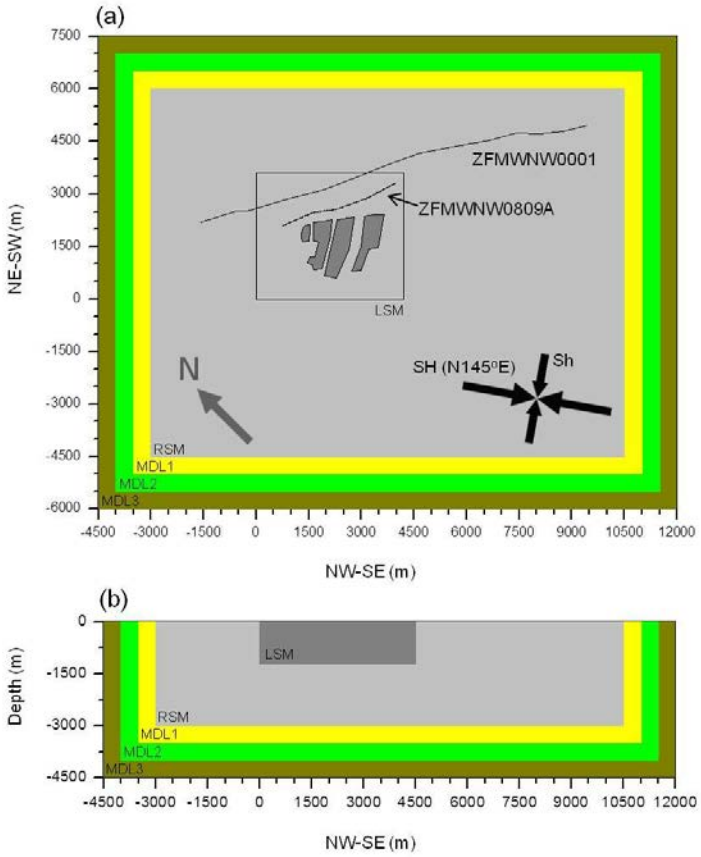

Figure 4-15. (a) Top view and (b) side view of the Regional Scale Model with Multiple Damped Layers (MDL). Traces of ZFMWNW0001 and ZFMWNW0809A are shown in the top view for reference.

5. Analysis of fracture shear displacement

In this Chapter, we discuss different concepts and methods (continuum model vs. discontinuum model) to analyze fracture shear displacement. Section 5.1 presents the results of FRACOD2D (Shen 2014) analysis and Section 5.2 presents the results of PFC3D modelling. The focus is given to the comparison of shear displacement profiles for different degrees of model complexity considering: fracture geometry (single planar vs. multiple segmented) and material property (elastic medium without fracture propagation vs. inelastic medium with fracture propagation).

5.1. Shear displacement of a single fracture in continuum model: FRACOD2D analysis

Shear displacement of a fracture embedded in an elastic rock model (Young's modulus E = 60 GPa and Poisson's ratio ν = 0.2) is tested using FRACOD2D (Shen 2014). Figure 5-1 shows the model, where on the left side the fracture is planar whereas in the right side the fracture is represented by a collection of smaller joints that are aligned parallel to the main fracture orientation. The left model fracture is referred to as 'single-planar fracture', and the right one is referred to as 'multiple segmented fracture'. The latter is considered to be more natural as rock fractures are usually irregular, non-planar or have other imperfections that prevent shear movements or have asperities that can be sheared off during slip events.

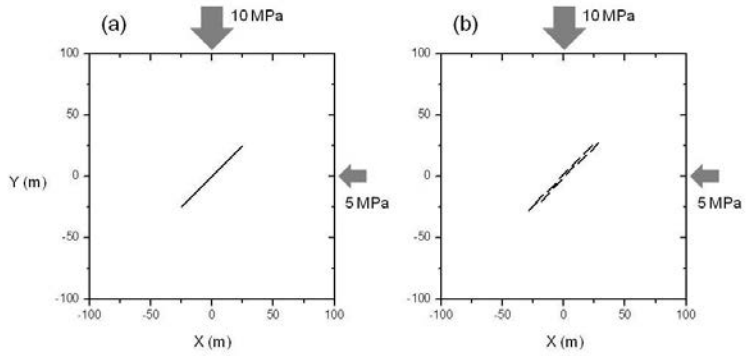

Figure 5-1. Single fracture represented as (a) a single planar segment and (b) multiple segments embedded in a continuum model and subjected to 10 MPa and 5 MPa biaxial stresses.

In addition to the geometrical complexity of the fracture, we also tested the fracture shear behaviour under variation of material property: Elastic vs. Inelastic. In the *elastic rock model*, the fracture is not allowed to propagate at the tips. This is done by setting a high fracture toughness (K_{IC} = 2.5 GPa√m and K_{IIC} = 4 GPa√m) to prevent the fracture from propagating at the tips under the given external loads. In the *inelastic rock model*, the fracture is allowed to propagate at the tips by setting K_{IC} = 2.5 MPa√m and K_{IIC} = 4 MPa√m. Therefore, in total, four cases are simulated with FRACOD2D.

The first set of results is shown in Figure 5-2 where the shear displacement of a single planar fracture is plotted with respect to normalized distance from the fracture

centre. The red curve shows the absolute displacement of the fracture in the elastic medium. The maximum displacement of 3.96 mm is monitored at the centre. In case of the propagated fracture shown by the blue curve, the maximum displacement at the centre is 4.18 mm, indicating that the maximum displacement increases by 6%. When the normalized displacements are compared (Fig.5-2b), it shows that the displacement near the fracture ends increases due to fracture propagation.

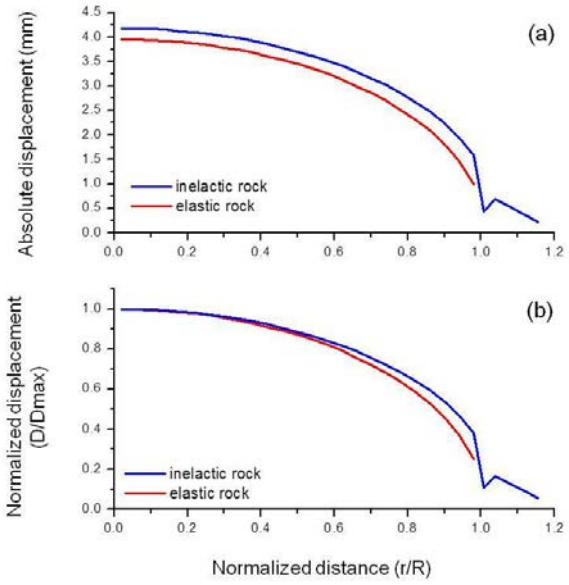

Figure 5-2. FRACOD2D modelling results showing (a) absolute shear displacement and (b) normalized shear displacement (D/Dmax) vs. normalize distance from the fracture centre (r/R) of the single planar fracture embedded in elastic (red) and inelastic rock (blue).

The second set of results is presented in Figure 5-3, where the shear displacement profiles of the multiple segmented fracture are plotted with respect to the normalized distance from the fracture centre. For comparison, the shear displacement profile of the single planar fracture without fracture propagation (Fig.5-2) is shown in red. In case of the multiple segmented fracture, the normalized displacement profile does not follow the parabolic profile (red curve) but concentrates in the range between a factor 0.6 and 1 of the maximum displacement and uniformly distributed along the entire fracture length. In case when a multiple segmented fracture is embedded in inelastic medium (with fracture propagation) the displacement profile is more widely distributed (Fig.5-3b). It implies that the maximum shear displacement does not always take place at the fracture centre, but can occur near the fracture ends if a rock fracture resembles the multiple segmented fracture.

The reason for larger displacement near the fracture ends can be explained as follows. In case of the single planar fracture, stress concentrates at the fracture tips as shown in Figure 5-4a. However, as the fracture tips are pinned and the propagation is not allowed, the energy given by the external loading is mostly spent in displacing the fracture and therefore the displacement records the maximum at the fracture centre. However, in case of the multiple segmented fracture (Fig.5-4b), the stress concentration at the two extreme ends is not as significant as in case of the single planar fracture. This is due to the fact that the energy provided by the external load is partitioned by the multiple segments, and therefore the amount of stress

concentration at the extreme ends of the fracture is less than that of the single planar fracture. The result implies that if there are more segments used in representing a fracture, the overall displacement profile could show less displacement at the centre and larger displacement near the fracture ends.

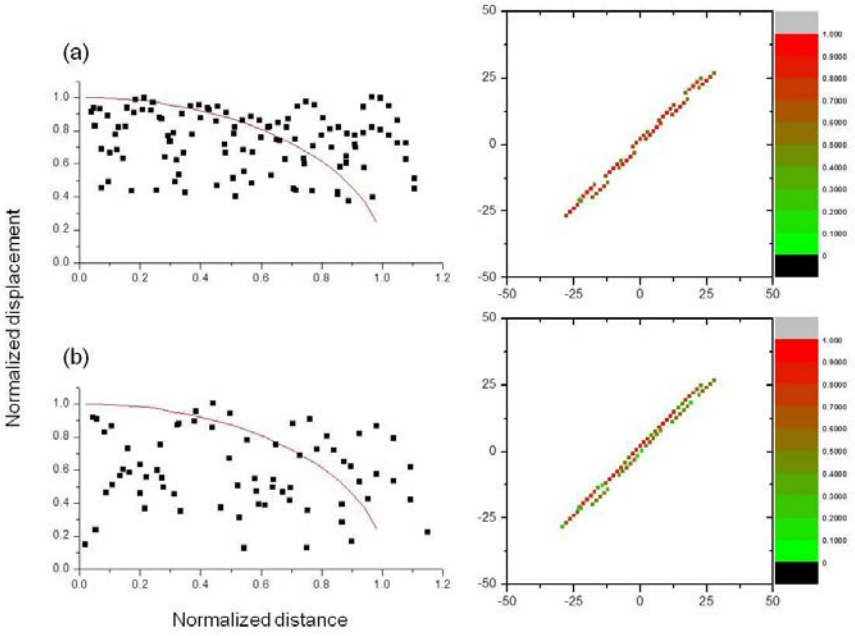

Figure 5-3. FRACOD2D modelling results showing normalized shear displacement of the segments composing the fracture embedded in (a) elastic rock (no fracture propagation) and (b) inelastic rock (fracture propagation). The right figures show each segment which is colored according to their normalized displacement from the fracture centre.

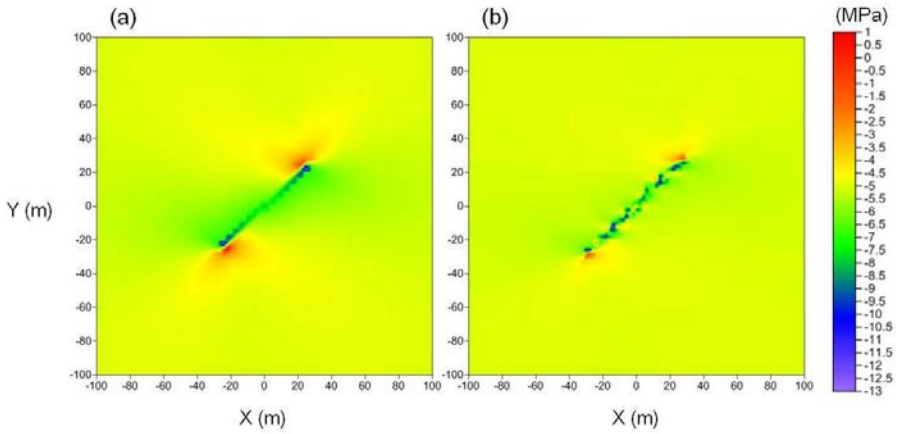

Figure 5-4. Distribution of maximum principal stress in an elastic rock model containing (a) a single planar fracture and (b) a multiple segmented fracture.

The absolute displacements of the segments of the multiple segmented fracture are compared in Figure 5-5. The result shows that the displacement increases generally in case when the fracture segments propagate and interact with other neighbouring fracture segments and form longer continuous fractures (coalescence).

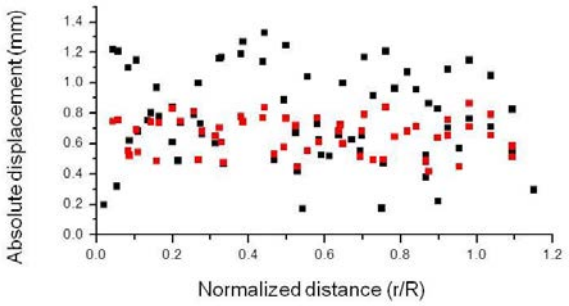

Figure 5-5. Absolute displacement of the segments of the multiple segmented fracture embedded in the elastic (red) and inelastic (black) models.

5.2. Fracture shear displacement of a fracture in a discontinuum model: PFC3D analysis

We performed another sets of fracture modelling using PFC3D v4. In the FRACOD2D modelling where the modelled fracture is embedded in a continuum medium, it is seen that the displacement profiles significantly deviate from the parabolic profile if the modelled fracture is represented as a multiple segmented fracture, and shows especially large displacement near the fracture ends.

In PFC3D modelling, the fracture is represented by a collection of smooth joints (Mas Ivars et al. 2011), which are embedded in a discontinuum medium represented by a collection of rigid spheres. The spheres are bonded at their contacts with finite stiffness and strength which can fail in different modes (Mode I in tension and Mode II in shear).

In this section we discuss how shear displacement of a fracture represented by a collection of smooth joints (referred to hereafter as a 'smooth joint fracture' changes due to the effects of: (i) particle size with respect to a fracture size, (ii) fracture intersection, and (iii) insertion order of the intersecting fractures.

5.2.1. Effect of smooth joint resolution on shear displacement

Three sets of models are generated here to test the effect of particle size relative to the fracture size (i.e. smooth joint resolution for representation of a fracture) on a fracture shear displacement. The models are 3x6x3 cm^3 in size and densely packed with three different particle size distributions with minimum particle radius of 0.5 mm, 0.75 mm, and 1 mm. Then, an inclined disk fracture is embedded with radius of 1.25 cm, 1 cm, and 0.75 cm, respectively. For this test, in total, 9 models are setup. Figure 5-6 shows one set of models with an inclined fracture with radius of 0.75 cm embedded at the centre of the models densely packed with particles with various radii. The models are referred to as fine- (Fig.5-6a), intermediate- (Fig.5-6b), and coarse- (Fig.5-6c) resolution models. The bottom figures are side views of the

smooth joint distributions. As the figures show, due to different particle size distribution, the patterns of smooth joint distributions are different. It is seen that the finer the particle resolution, the smaller the size of the smooth joints, and the narrower the width of the smooth joint clusters in the direction normal to the fracture plane.

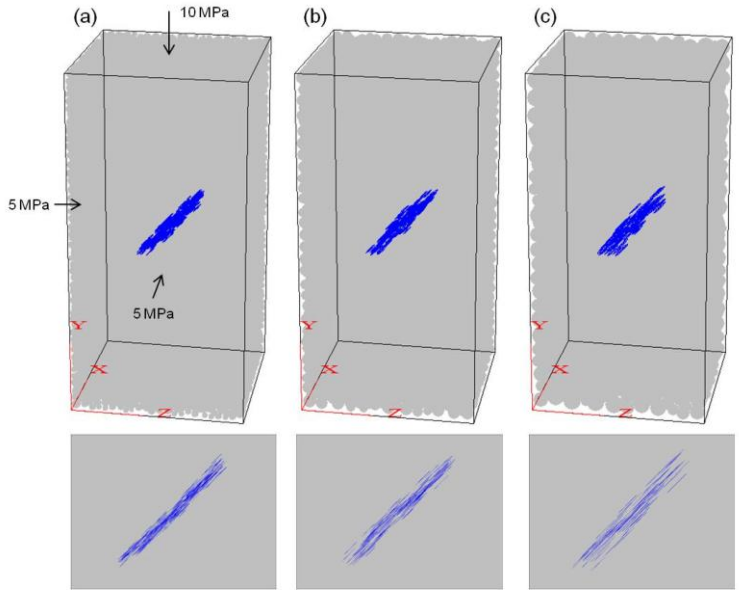

Figure 5-6. Densely packed particle assembly with different particle size distribution (minimum particle radius of (a) 0.5 mm, (b) 0.75 mm, (c) 1 mm) and with an inclined fracture embedded at the centre. The bottom figures show the side views.

The models are then loaded triaxially with 10 MPa vertical stress (σ_{zz}) and 5 MPa lateral stress (σ_{xx}=σ_{yy}). Figure 5-7 shows the shear displacement of the smooth joints with respect to their distance from the fracture centre. The numerical results show that, in general, the smooth joint shear displacement is large at the fracture centre and tapers towards the tips. The solid lines plotted in the figure are the analytically determined shear displacement distribution of a planar fracture with identical radius using the following analytical solution (Segedin 1951):

$$u(r) = \frac{8}{\pi(2-\nu)}\frac{(1-\nu)}{G}\Delta\tau\sqrt{a^2 - r^2} \qquad \text{Eqn. (5-1)}$$

where, G is the shear modulus of the rock model, ν is Poisson's ratio and $\Delta\tau$ is the applied shear stress on a fracture, a is the fracture radius, and r is the distance of the occurrence point of the shear displacement from the fracture centre. The elastic constants E, G, and ν of the models in Figure 5-6 are determined from uniaxial compression tests. The analytically determined shear displacement shows parabolic profile with maximum at the fracture centre and tapering toward the fracture tips.

The analytical solution, Eqn. (5-1), expresses the shear displacement distribution of a perfectly planar and frictionless fracture embedded in an elastic medium. Therefore, the energy given by the external loading is spent mostly on displacing the fracture and therefore it results in the largest displacement at the fracture centre.

However, in the PFC3D models, the fracture is not planar and the bonded particle assembly also deforms by the external loading. The energy provided by the external loading is then partitioned by the slip of the smooth joints.

The numerical results show that the displacement profile is rough and the degree of fluctuation becomes more significant with increasing particle size, i.e. in the coarser resolution model (Fig.5-7c). Moreover, the shear displacement profile of the largest fracture (red profile) is generally higher for the case of a coarse particle resolution model. The reason for such large shear displacement and high irregularity is due to the gap between the smooth joints. The gap between the smooth joints (inter-segment area in 2D or volume in 3D) is larger as the particle resolution becomes coarser. And as the gap between the smooth joints becomes larger, there are more rigid particles in the area between the smooth joints, which results in higher stress concentration. Higher concentration of stress at the inter-segment volume results in large shear displacements of the segments (smooth joints) near the stress concentration.

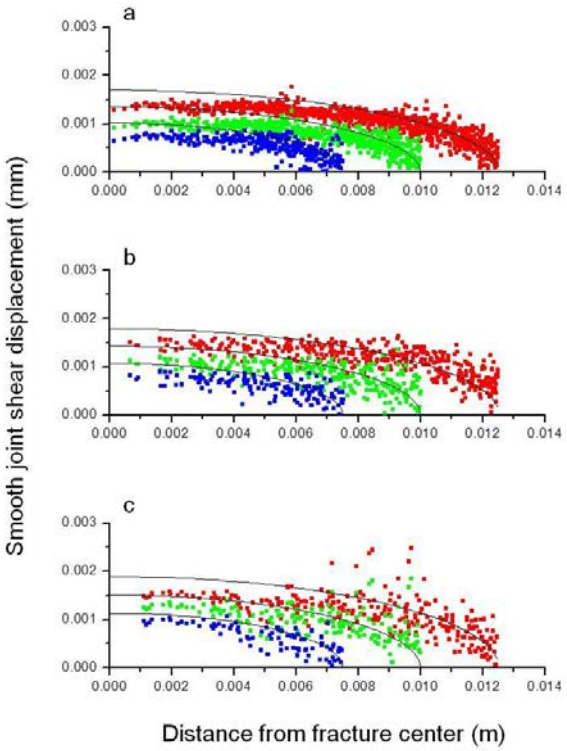

Figure 5-7. Shear displacement of the smooth joints of the fractures embedded in (a) fine resolution, (b) intermediate resolution, and (c) coarse resolution models. The solid lines represent analytically determined shear displacement of a planar fracture with same size.

5.2.2. Effect of rattlers on shear displacement

Yoon et al. (2016a) have demonstrated that the shear displacement profile of a fracture in a 2D model deviates from the parabolic profile that is analytically calculated, and the degree of deviation becomes larger when the fracture is

intersecting other fractures. It was found that such displacement spikes at the intersection locations occur due to presence of particles that become detached from the surrounding particles, therefore so called “rattler particles”. A numerical algorithm for detecting and deleting rattler particles is developed and tested in a 2D model with five intersecting fractures as shown in Figure 5-8a. The results show that the displacement spikes (Fig.5-8b) disappear after eliminating the rattler particles from the model (Fig.5-8c), and become similar to the results of FRACOD2D modelling (Fig.5-8d).

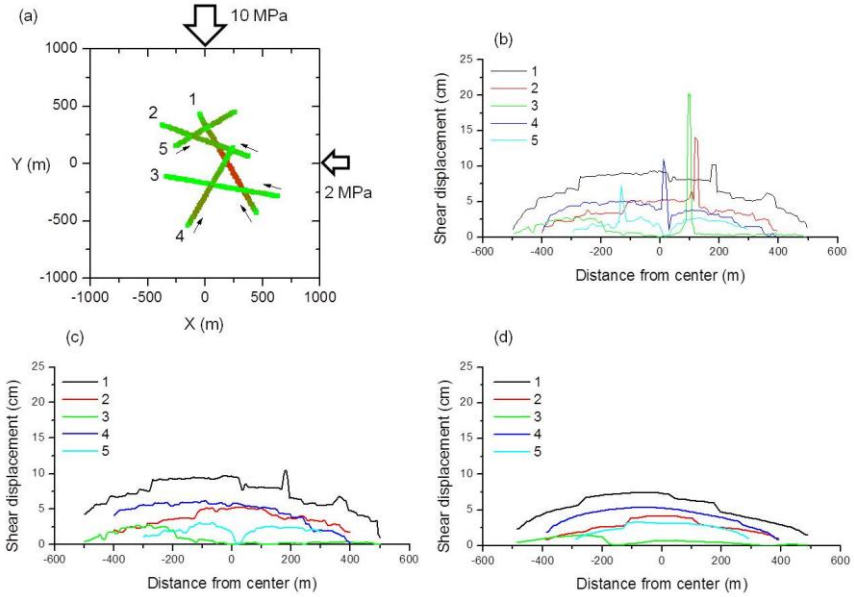

Figure 5-8. (a) 2D model with five intersecting fractures and loaded 10 MPa axially and 2 MPa laterally, (b) shear displacement distributions of five intersecting fractures before deleting and (c) after deleting the rattler particles, and (d) shear displacement distributions obtained from FRACOD2D modelling (Yoon et al. 2016a).

We also applied the algorithm to the 3D PFC model with five intersecting fractures. The 3D model is shown in Figure 5-9 with axial stress (σ_{zz}) of 10 MPa and lateral stress ($\sigma_{xx}=\sigma_{yy}$) of 2 MPa. The shear displacement distributions of the fractures are shown in Figure 5-10 with respect to the distance of the smooth joint from the fracture centre. The results show that there are several smooth joints with significantly large shear displacement, but these shear displacements are eliminated by deleting the rattler particles. However, there still exist several smooth joints, especially at fracture 1 and fracture 3, showing sharp increase and drop of the displacements.

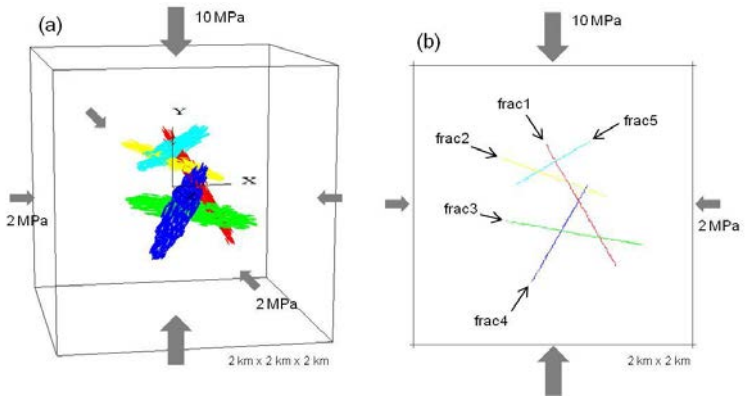

Figure 5-9. (a) 3D model with embedded five intersecting fractures and subject to triaxial loading and (b) the equivalent 2D model (Yoon et al. 2016a).

Mean shear displacements are calculated for the fractures and presented in Table 5-1. The values in the left column are the mean displacement before deleting the rattler particles (Fig.5-10, left figures), and those in the right column are the mean displacement after deleting the rattler particles (Fig.5-10, right figures). The results show that the relative differences are between 2 and 10%.

Also, median shear displacements are calculated for the fractures and presented in Table 5-2. The values in the left column are the median displacement before deleting the rattler particles (Fig.5-10, left figures), and those in the right column are the mean displacement after deleting the rattler particles (Fig.5-10, right figures). The results show that the relative differences are negligible.

The results demonstrate that median value of the smooth joint shear displacements provides robustness for determination of a representative shear displacement of fractures that are made up of many smooth joints and intersected by neighboring fractures. This result supports our decision for use of median over mean, which is discussed later in Section 5.4.

Table 5-1. Mean shear displacements of the fracture: before deleting the rattler particles (left column) and after deleting the rattler particles (right column).

	Mean shear displacement (cm)		Relative difference (%)
	Before	After	
Fracture 1	5.10	4.91	3.7
Fracture 2	2.51	2.52	0.4
Fracture 3	1.17	1.09	6.8
Fracture 4	2.36	2.33	1.3
Fracture 5	1.38	1.38	0.0

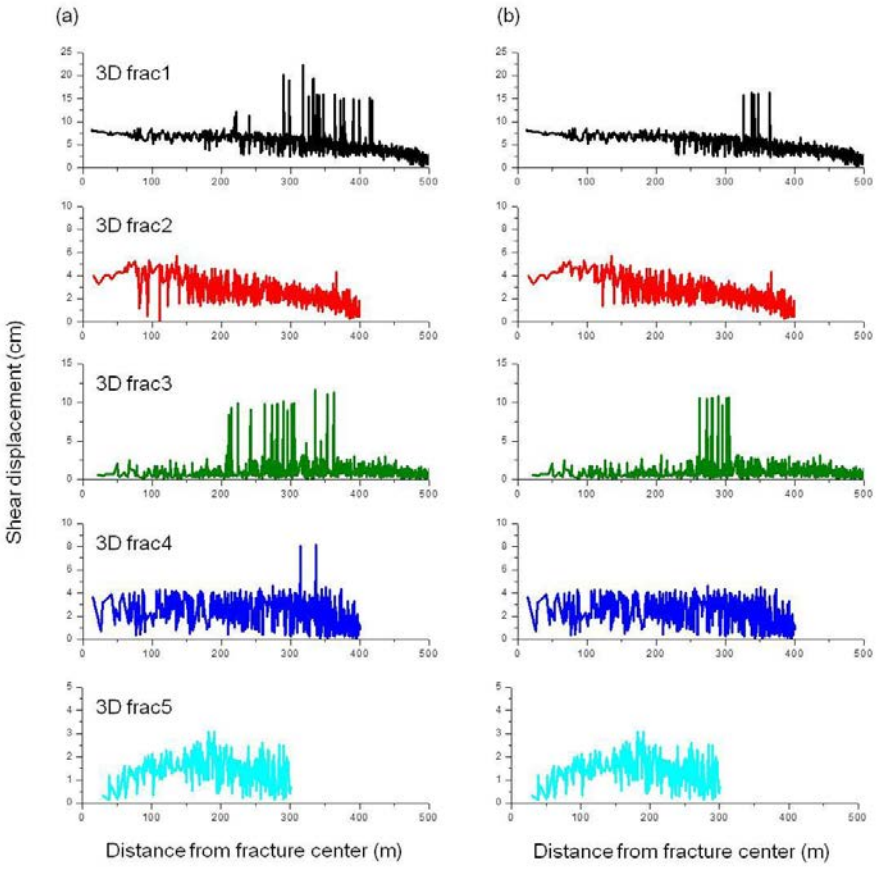

Figure 5-10. Shear displacement of the smooth joints of the 3D fractures (a) before and (b) after eliminating the rattler particles.

Table 5-2. Median shear displacements of the fracture: before deleting the rattler particles (left column) and after deleting the rattler particles (right column).

	Median shear displacement (cm)		Relative difference (%)
	Before	After	
Fracture 1	5.10	5.01	1.8
Fracture 2	2.31	2.32	0.4
Fracture 3	0.83	0.83	0.0
Fracture 4	2.48	2.47	0.4
Fracture 5	1.38	1.38	0.0

5.2.3. Effect of fracture embedding sequence on shear displacement

There is an additional aspect that influences the fracture shear displacements when the fractures are intersecting. It is the sequence in which the fractures are embedded in a bonded particle assembly. One example is shown in Figure 5-11 where the blue fracture is embedded first among the eight fractures (Fig.5-11b), embedded last (Fig.5-11c) and embedded 5th (Fig.5-11d).

When the blue fracture in Figure 5-11 is embedded first, the smooth joints assigned to the blue fractures are not affected by the subsequent fractures, and therefore the fracture area is A_{pfc} = 1.522e-3 m^2 and the area ratio is A_{ratio} = 2.15. When the blue fracture is embedded at the last (Fig.5-11c), the trace of the blue fracture is terminated at the locations of the intersection. In this case, the fracture area becomes A_{pfc} = 1.373e-3 m^2 and the area ratio A_{ratio} = 1.94.

In such way, an extreme case may exist where the area ratio of a fracture becomes smaller than 1 if the fracture is embedded at the last in a highly densed discrete fracture network, such as in the DFN model shown in Figure 4-5. In such case, these fractures can be rejected in the analysis.

The models are then triaxially compressed by 10 MPa vertical stress (σ_{zz}) and 5 MPa lateral stresses (σ_{xx}=σ_{yy}). Figure 5-12 compares the distribution of the smooth joint shear displacement of an inclined blue fracture. In case when the fracture is isolated, the shear displacement distribution shows the maximum at the centre and tapers towards the tip (Fig.5-12a) and the distribution is in general smooth. When the blue fracture is intersected by other fractures the shear displacement distribution becomes irregular with many local displacement heterogeneities which occur mostly at the intersection locations (Fig.5-12b, c, d). The median displacements are calculated and shown by the red horizontal lines in Figure 5-12. The median displacements of the blue fracture are listed in Table 5-3. When a fracture is isolated without any interactions with others, the median shear displacement is 1.67e-3 mm. The median displacements of the blue fractures are 1.34e-3 mm and 1.23e-3 mm when embedded first and last, respectively. In case when the blue fracture is embedded in 5th, the median displacement is 1.26e-3 mm. The results show that the median displacement of a fracture tends to be lower when the fracture is intersected by other fractures. However, in case when the fracture is intersected by other fractures, the displacement profile shows many locally occurring large displacements.

The maximum displacements are listed in Table 5-3. The results demonstrate that a fracture shear displacement embedded in a bonded particle model significantly depends on their embedding sequence in the model. The fact that the shear displacement distribution becomes more heterogeneous with locally large displacement at intersecting locations implies that it is more conservative to take into consideration, in a safety assessment of underground facility in a fractured rock mass where the rock fracture displacement is of concern, the complex fracture network system (like in this study) as intersecting fractures results in larger displacements than to take only individual fractures that are isolated (like in Fälth et al. 2010, also shown in Fig.2-1).

Taking this observation into consideration, as pointed out by Mas Ivars et al. (2011), joint termination, joint intersection, and joint hierarchy must be considered when constructing a DFN and embedding it in a particle assembly model. Joints are created by specific stress mechanisms associated with geological events which generated different sets of joints in different orientations at different times. For example as shown in Figure 5-13, early joints tend to be long, relatively continuous, and in-filled with vein material, whereas later joints are cut by the earlier ones, and

are consequently shorter (Hudson & Cosgrove 1997). In cases where a joint hierarchy is evident, this can be accounted for in the order of joint insertion. The first joint inserted is always continuous in its entirety; while subsequent joints intersecting the first one has large asperities in the shared contacts at the intersections and therefore is discontinuous.

If there is any information on the hierarchy of the joints in the DFN for the Forsmark repository model (Fig.4-5a), the models should be regenerated with correct sequence of fracture insertion. However, since there is no data or evidence on the hierarchy of the joints in the repository rock volume at Forsmark site, we assume the DFN sequence as random.

Table 5-3. Area ratios of the blue fracture (A_{ratio}) and the median and maximum values of the shear displacement of the smooth joints of the blue fracture.

Insertion order of blue fracture	A_{ratio}	D_{med} (mm)	D_{max} (mm)	D_{max}/D_{med}
Isolated (Fig.5-11a)	2.15	1.67e-3	2.21e-3	1.32
12345678 (Fig.5-11b)	2.15	1.34e-3	4.62e-3	3.45
1234567**8** (Fig.5-11c)	1.94	1.23e-3	2.28e-3	1.85
1234**5**678 (Fig.5-11d)	2.05	1.26e-3	4.59e-3	3.64

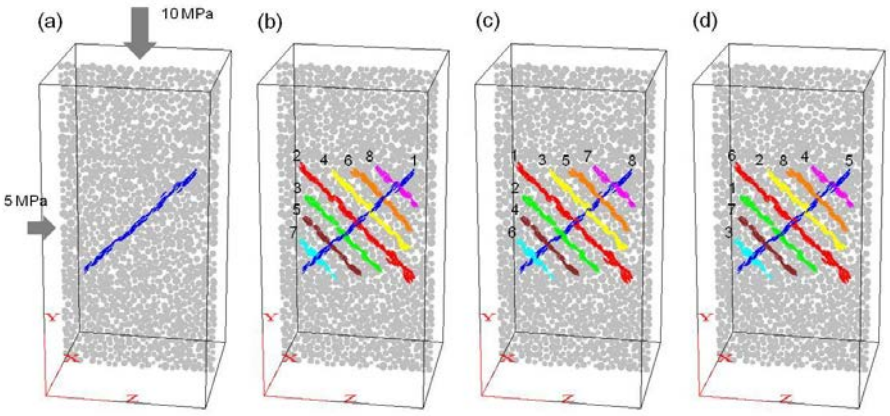

Figure 5-11. (a) Single fracture model and (b-d) eight fracture models with different fracture insertion orders denoted by the numbers in the figure.

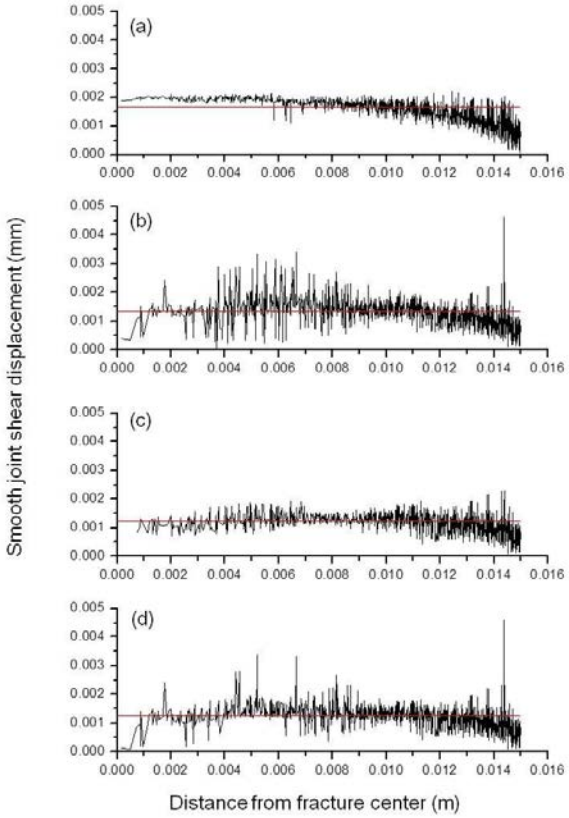

Figure 5-12. Shear displacement distribution of the blue fracture when (a) isolated, and when embedded (b) first, (c) last and (d) the fifth in the model.

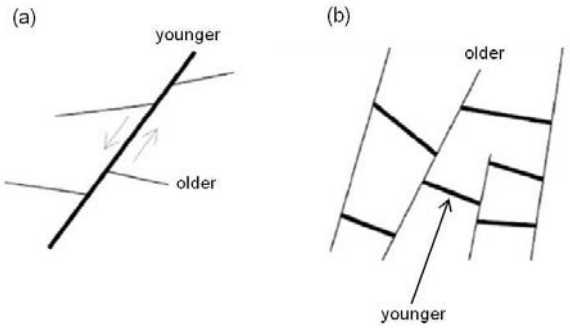

Figure 5-13. Joint interaction age determination runnels: (a) the shear fracture (younger) cuts and displaces another discontinuity set (older), (b) the discontinuity sets that terminate are younger and the set that stops the other from propagating is the older ones (from Mas Ivars et al. 2011).

5.3. Comparison of shear displacement: multiple segmented representation vs. single planar idealization

The test results shown previously demonstrate that a shear displacement distribution of a fracture modelled in PFC3D by a collection of smooth joints (referred to hereafter as '*multiple segment representation*') depends significantly on the particle size. In this section, we investigate how much a fracture shear displacement is affected by the particle size, and compare with the results of single planar idealized fractures (referred to hereafter as '*single planar idealization*').

We investigated the relation between the fracture area ratio (Eqn. 4-4, Section 4.2) and the fracture slip volume (m^3). Fracture slip volume (V_{slip}) of a single planar fracture showing parabolic profile is calculated by the following equation, Eqn. (5-2).

$$V_{slip} = \frac{2\pi}{3}\frac{8}{\pi(2-\nu)}\frac{(1-\nu)}{G}\Delta\tau a^3 \qquad \text{Eqn. (5-2)}$$

Slip volume of a multiple segmented fracture is calculated by Eqn. (5-3) below, which is a sum of the product of individual smooth joint area (m^2) and the smooth joint displacement (m).

$$V_{slip} = \sum_{i=1}^{n} sj_A(i) \times sj_d(i) \qquad \text{Eqn. (5-3)}$$

where, $sj_A(i)$ is the area of the i-th smooth joint and $sj_d(i)$ is the shear displacement of the i-th smooth joint.

Fracture slip volume that are calculated for a single planar fracture and a multiple segmented fracture are listed in Table 5-4, and their ratios ($V_{slip,ratio}$) are plotted in Figure 5-14a with respect to the fracture sizes and the particle minimum radii. The colours of the squares represent the $V_{slip,ratio}$.

The results show that the $V_{slip,ratio}$ increases with increasing particle size for a fixed fracture size, i.e. less number of smooth joints (segments) for representation of a fracture. Also, the $V_{slip,ratio}$ increases with increasing fracture size for a fixed particle size, i.e. larger number of smooth joints for representation of a fracture. It implies that a multiple segmented fracture constructed with smaller number of smooth joints (segments) but with large area, i.e. a fracture embedded in a coarse particle resolution model, the $V_{slip,ratio}$ is larger compare to a single planar fracture with equivalent size.

Fracture slip volume ($V_{slip,ratio}$) is plotted in Figure 5-14b with respect to the fracture area ratio (A_{ratio}), showing that $V_{slip,ratio}$ increases with A_{ratio}. Therefore, as $V_{slip,ratio}$ linearly depends on the shear displacement (d) which is affected by the numerical artefacts (resolution of smooth joints for representation of a fracture – Section 5.2.1, area ratio resulting from particle size and fracture insertion sequence – Section 5.2.3), we suggest that the shear displacement of a multiple segmented fracture be calibrated based on the fracture slip volume ratio which is a function of fracture area ratio.

We apply this calibration measure to the results of PFC3D modelling assuming that a multiple segmented fracture, which is represented by a collection of smooth joints, is equivalent to a single planar disk fracture.

Table 5-4. Fracture radius (R_{frac}), Minimum particle radius ($R_{p,min}$), Area ratio, analytically determined slip volume of a single planar fracture (V_{slip-s}) and of a multiple segmented fracture (V_{slip-m}) and the ratio of slip volume.

R_{frac} (m)	$R_{p,min}$ (m)	A_{ratio}	V_{slip-s} (m^3)	V_{slip-m} (m^3)	$V_{slip,ratio}$
1.25e-2	0.50e-3	2.18	5.56e-10	1.09e-9	1.96
1.00e-2	0.50e-3	2.18	2.84e-10	5.10e-10	1.80
0.75e-2	0.50e-3	2.15	1.20e-10	2.07e-10	1.73
1.25e-2	0.75e-3	2.18	5.86e-10	1.23e-9	2.10
1.00e-2	0.75e-3	2.19	3.00e-10	5.71e-10	1.90
0.75e-2	0.75e-3	2.27	1.26e-10	2.33e-10	1.85
1.25e-2	1.00e-3	2.28	6.19e-10	1.24e-9	2.00
1.00e-	1.00e-3	2.29	3.17e-10	6.82e-10	2.15
0.75e-2	1.00e-3	2.38	1.34e-10	2.54e-10	1.90

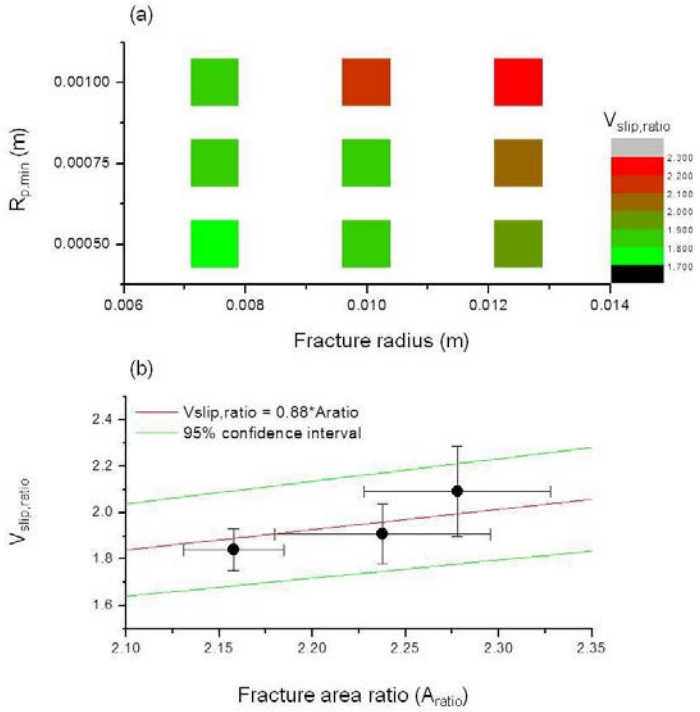

Figure 5-14. (a) Variation of fracture slip volume ratio with respect to the fracture size and the minimum particle radius and (b) linear scaling of the fracture slip volume ratio with increasing fracture area ratio.

5.4. Discussion

In this section, we compare the shear displacements of PFC3D fractures with the length-displacement scaling relations of natural fault-fracture systems. Median shear displacements of the multiple segmented fractures are calibrated using the relation between fracture slip volume and fracture area ratio, to provide lower bound fracture displacement for single planar idealization.

The simulation results are compared with the global data sets of fault-fracture displacement vs. length scaling as shown in Figure 5-15, which shows that the displacement (D) scales linearly with length (L) over seven orders of magnitude. The red boxes shown in the figures correspond to the length-displacement ranges shown in Figure 5-16 which is discussed below. The length vs. displacement data for natural faults are presented in Figure 5-15a. The linear scaling relation is described by the following equation (Cowie and Scholz 1992; Schlische et al. 1996, Schultz et al. 2006):

$$D = cL^n \qquad \text{Eqn. (5-4)}$$

where, the exponent n = 1 and the proportionality constant c = 1e-1, 1e-2, and 1e-3. The data plotted are the maximum displacement of the surveyed faults, and it shows that globally collected data sets are all below the linear scaling relation with the proportionality constant c = 0.1. Figure 5-15b shows the data sets for joints, veins, and igneous dikes, and the new scaling relations are given as dashed lines with same proportionality constant c = 0.1, 0.01, and 0.001, but the exponent n = 0.5.

We compare the results of one modelling case chosen among those presented in Chapter 6. The chosen modelling case concerns activation of ZFMA3 under present day stress condition (see Table 6-1). Figure 5-16 shows the shear displacement of the fractures that are crossing the repository depth (referred to as 'repository fractures'). Two sets of data are presented: mean shear displacements of multiple segmented fractures (red dots) and those for single planar idealization (green dots). Figure 5-16a shows the mean displacements of the two data sets, and Figure 5-16b shows the median displacements of the two data sets.

Comparing the PFC3D results (median displacements of multiple segmented fractures, Fig.5-16b) with the global data sets (Fig.5-15b) demonstrates that the simulated displacements of the repository fractures are below the globally collected data set. This observation is considered reasonable as the natural fractures of the globally collected data set may have undergone various types of loading, e.g. tectonic, seismic, aseismic, induced, over long time period, and therefore the data can be considered as an upper bound for the fracture displacements. However, a possibility that the slip of a few fractures induced by an earthquake faulting exceeds the upper bound scaling relation cannot be ruled out.

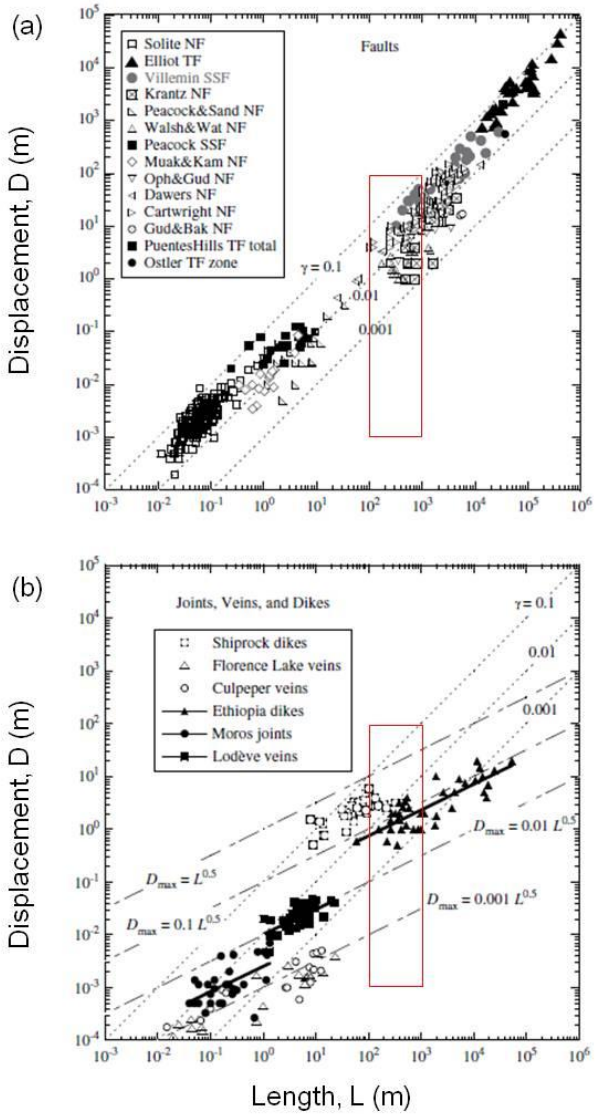

Figure 5-15. Length-displacement data of (a) faults from Cowie and Scholz (1992), Schlische et al. (1996), and Schultz et al. (2006), and (b) joints, veins, and dikes. The dotted lines are the linear scaling relations of the length and the displacement, Eqn. (5-4). Dashed lines are the linear scaling relations, Eqn. (5-4) with the exponent n = 0.5. The red boxes show the ranges of the displacement-length in Figure 5-16.

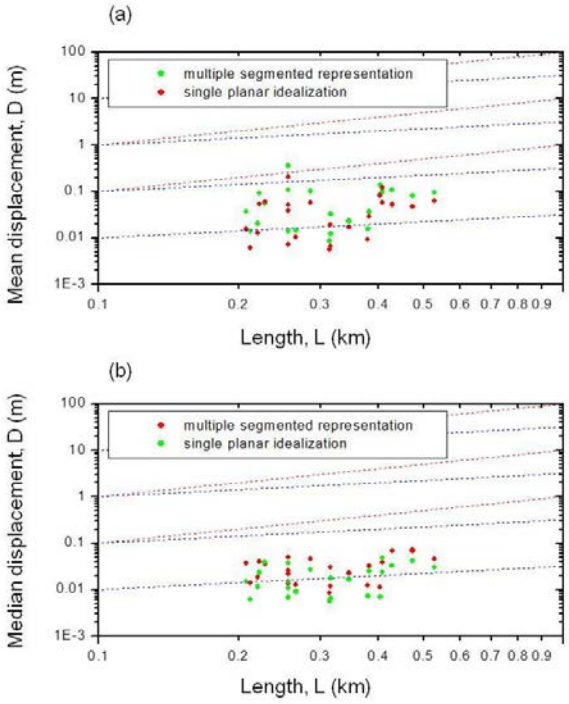

Figure 5-16. Distribution of (a) mean and (b) median slip displacements of the repository fractures (red dots: multiple segmented fracture, green dots: single planar idealization) induced by activation of ZFMA3 in the Regional Model Scale simulation. The red and the blue lines are the displacement vs. length scaling relations that are represented by Eqn. (5-4).

Whether the fractures are continuous or discontinuous (non-planar) can be discussed in terms of maturity of the geological discontinuities. In Figure 5-17, Perrin et al. (2016) discussed that as a fault accumulated more displacement, its discrete segments increasingly coalesce so as to form a through-going fault. This is commonly described as the accumulation of slip leading to a geometrically simpler fault.

In this study, as no information on the ages of the fracture network has been provided in the Forsmark repository rock volume, fracture planarity was randomly determined. This means that when a fracture is embedded in the particle assembly model, the fracture can be either represented as a plane-like structure (Fig.5-17b) or as a band-like structure (Fig.5-17c). However, in all cases, the fractures in the PFC3D model are discontinuous and have intersegment structures. This is the nature of fracture modelling in PFC using smooth joint model.

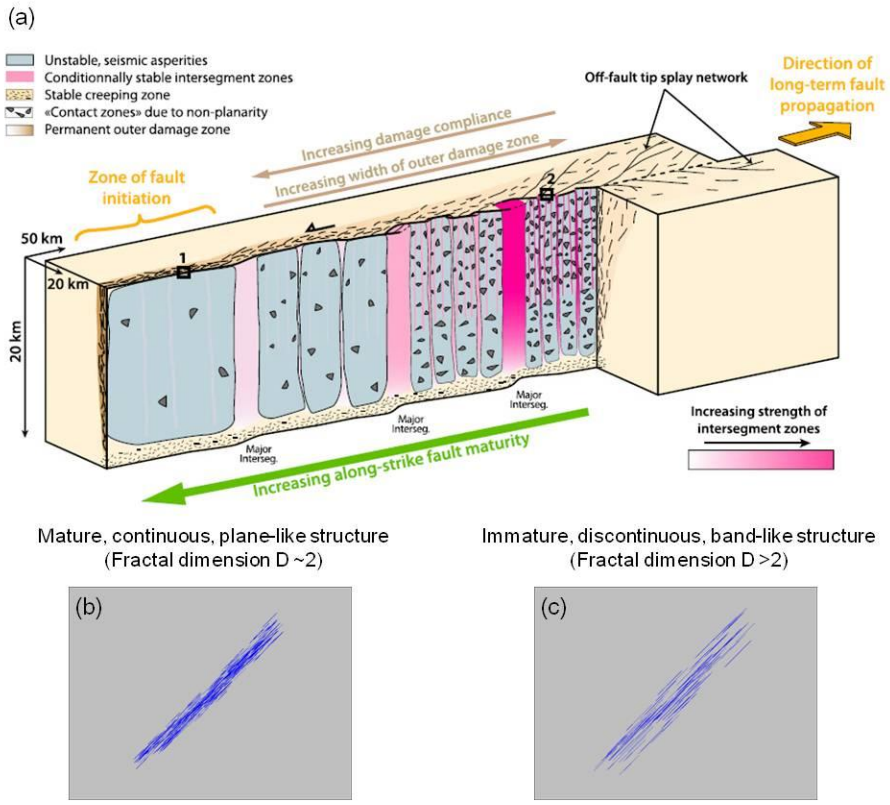

Figure 5-17. (a) Concept of along-strike evolution of off-fault damage, fault segmentation and fault planarity with increasing maturity along fault strike (Perrin et al. 2016), side view of a PFC3D fractures (b) with more continuous, plane-like structure and (c) with more discontinuous, band-like structure.

From the 2D modelling study of Yoon et al. (2016a), it was found that the displacement spikes that occur at the locations of fracture intersection are due to rattler particles, which were treated as a numerical artifact. Therefore an attempt was made to delete the rattler particles in the analysis of the fracture shear displacement and to make the slip profile same as those simulated in continuum based modelling, e.g. FRACOD2D (Fig.5-8).

Figure 5-18 shows schematics of the range of damage zones that are commonly found around strike-slip fault zones (Kim et al. 2004, Choi et al. 2012). The structures of the damage zone associated with earthquake faulting are: wing crack, pull-apart, synthetic or antithetic faults, rotated blocks and connecting faults, horsetail splays, isolated lenses, branch faults. Among these structures, especially rotated blocks within the damage zones: (i) Mode II (2D) and Mode III (3D) tip damage zone, (ii) wall damage zone, and (iii) linking damage zone (Fig.5-18a), could be a possible explanation for what is simulated in the PFC3D model.

A particle detached from the surrounding particles is analogous to a block detached from the surrounding blocks and fault planes and rotates, of which the movement (translational, rotational) is taken into account in the total displacement at the specific location. The number of detached blocks and their rotational movements may increase with increasing fault structural complexity, which is documented as large slip (horizontal slip or vertical throw) as, for example, shown in Figure 5-19 which is slip profiles of earthquake faults. The figure demonstrates that the sharp increase and drop of displacement occur along the discontinuity traces and especially at the locations of intersections (structural complexity) of geological

discontinuities (Milliner et al. 2016). The figure shows the slip profile of Landers earthquake fault and the slip variability (black line) depends highly on the surface trace complexity. The slip profile is smoother along the fault trace with less complex fault trace (less interaction with other faults). The slip profile becomes rough and spiky (sharp increase and drop) especially at those regions with high structural complexity.

It is often observed in natural fault systems as shown in Figure 5-19 that displacement jumps occur not only at the locations of fault-fault intersections but also locally along the fault trace. Such observations support the idea that the sharp increase/drop of displacement simulated in the PFC3D modelling (sharp increase and drop at the fracture intersection) to some extent mimics the natural phenomena, i.e. stress concentration at one specific point at the fault trace and at fault-fault intersection location leading to local damage and seismicity concentration and large slip.

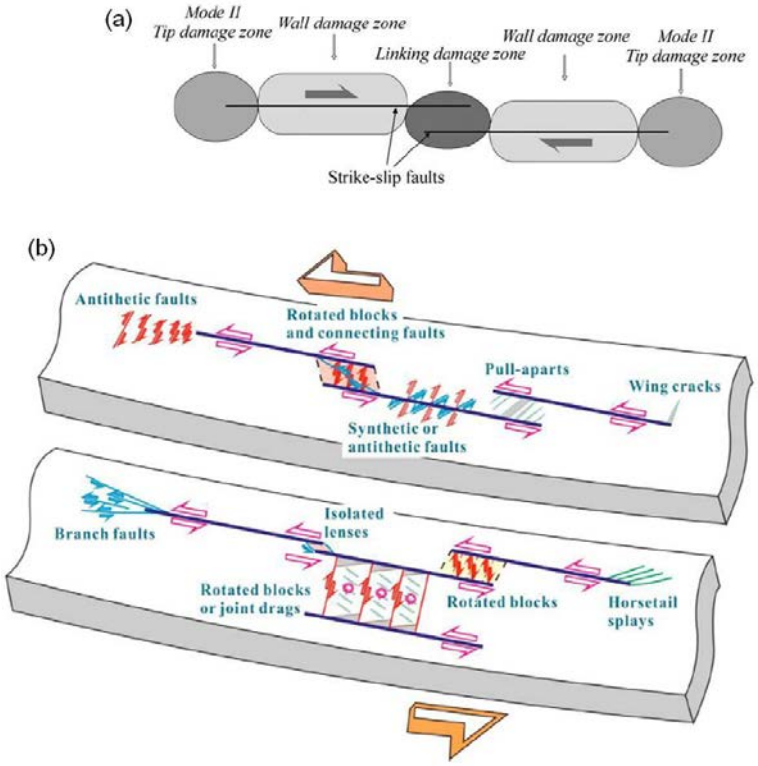

Figure 5-18. (a) Schematic diagram of the principal locations of damage zones around a strike-slip fault zone: classified into three main types: tip damage zone, linking damage zone, and wall damage zone (from Kim et al. 2004), (b) Schematic diagram showing structures that typically occur in damage zones around strike-slip faults. These structures include connecting faults, branch faults, wing cracks, pull-aparts, synthetic or antithetic faults, horsetail fractures, rotated blocks or joints drags, and isolated lenses (from Choi et al. 2012).

It is our conclusion from the analyses that the way of modelling rock fractures (and faults) in PFC3D as a collection of smooth joints, therefore resulting in a multiple segmented step-over structure, better mimics the natural rock fracture and faults. Therefore the results of PFC3D, to some extent, may describe the natural phenomena associated with earthquake faulting and fracture interaction.

However, we further exclude the possibility that such large displacement in particular at fracture intersection could attribute to numerical artifacts. Therefore, in the subsequent chapters where the main results of the modelling cases are shown, we present “median” shear displacement of the smooth joints that compose a fracture, instead of taking “mean”, as a representative value of shear displacement of a fracture.

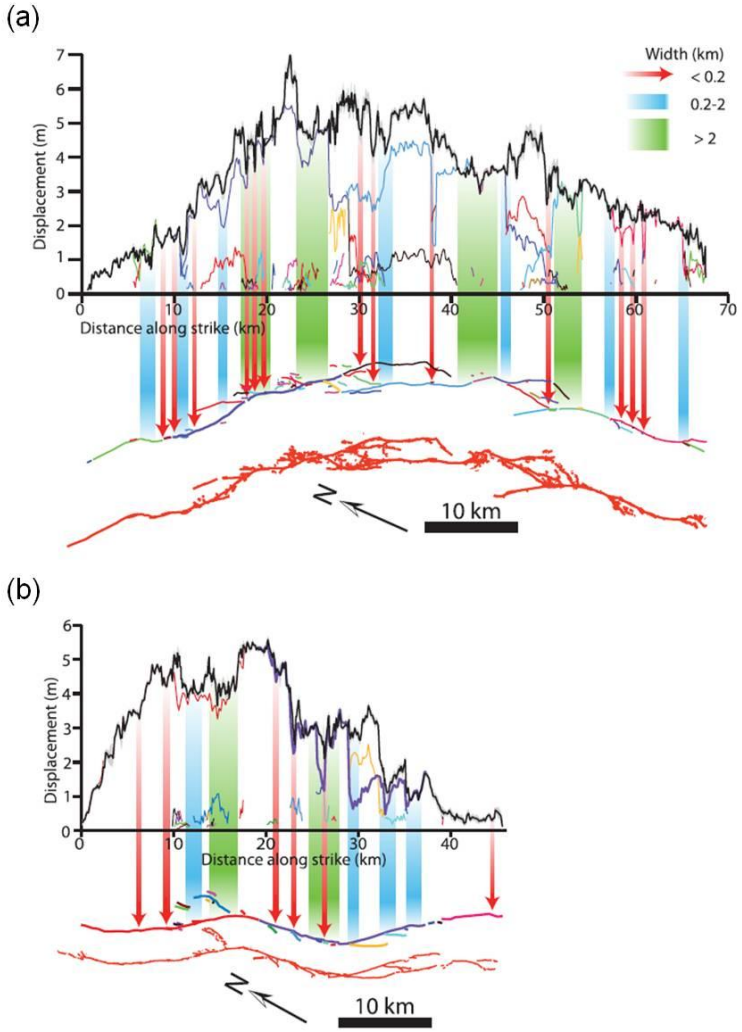

Figure 5-19. Correlation of slip variability (black line) to surface trace complexity. Slip profiles for (a) Landers and (b) Hector Mine earthquake faults (from Millier et al. 2016).

6. Modelling cases

In this Chapter, we present the modelling cases of which the results are presented in Chapters 7, 8 and 9. Table 6-1 lists the modelling cases with combinations of modelling conditions for the Local Scale Model (LSM) and the Regional Scale Model (RSM). The priority of the modelling cases has been chosen through discussion with SSM.

6.1. Local Scale Model (LSM)

For the Local Scale Model (LSM), in total, six modelling cases are setup of which the objectives are described below.

The first type of loading is thermal and two modelling cases are simulated. In the first case, the heat from the canisters is released simultaneously, assuming that all the canisters are disposed of in the deposition holes and closed at the same time. In the second case, the heat release is simulated in panel-by-panel sequence, assuming that the canister emplacement and closure of the deposition holes are done in panel by panel order, starting from panel A (Fig.4-9).

The second type of loading is seismic, which is generated by a dynamic rupture of a nearby fault. For this, we chose the deformation zone ZFMWNW0809A and activation under two *in-situ* stress conditions: present day most likely stress condition and the stress condition under the effect of forebulge induced by glacial ice cover.

The third type of loading is a combination of heat loading and seismic loading. Two modelling cases are chosen to study the effect of a fault dynamic rupture under the operational period of the repository. The times when the fault is ruptured are 50 years and 100 years after release of heat from the canisters.

6.2. Regional Scale Model (RSM)

For the Regional Scale Model (RSM), in total, five modelling cases are simulated.

Activation of ZFMWNW0001 (Singö fault) is simulated under present day *in-situ* stress condition and the stress condition under the effect of forebulge induced by the ice cover. Forebulge stress condition is chosen as it results in the highest stress anisotropy (SH'/Sh' = 2.7, see Table 4-7).

Activation of ZFMA3 (a large gently dipping deformation zone above the repository rock volume) is simulated under the present day *in-situ* stress condition and the stress condition under the effect of retreating ice cover (deglaciation). The *in-situ* stress condition induced by the retreating ice cover is chosen as the stress field becomes more favorable for reverse faulting than the stress condition at present day. This is indicated by the stress ratio k = 4.2 (Table 4-7).

Table 6-1. Modelling cases.

Source of loading	Local Scale Model	Regional Scale Model
Repository panel heat	• Simultaneous panel heating + Present day stress • Sequential panel heating + Present day stress	
Dynamic fault rupture	• ZFMWNW0809A rupture + present day stress • ZFMWNW0809A rupture + ice cover forebulge stress	• ZFMWNW0001 rupture + present day stress • ZFMWNW0001 rupture + ice cover forebulge stress • ZFMA2 rupture + present stress • ZFMA3 rupture + present stress • ZFMA3 rupture + ice cover retreat stress
Repository panel heat + Dynamic fault rupture	• Simultaneous heating 50 years + present day stress + ZFMWNW0809A rupture • Simultaneous heating 100 years + present day stress + ZFMWNW0809A rupture	

7. Modelling of repository heating and the impact to the repository fractures

In this Chapter, we present two modelling cases where the shear displacements of the repository fractures are induced by the decaying heat of the canisters containing the spent nuclear fuels. The first modelling case concerns a scenario where all the canisters are emplaced at the deposition holes and closed at the same time, and therefore the start time of the heat release for all canisters is the same (referred to hereafter as 'simultaneous panel heating'). The second modelling case concerns a scenario where the emplacement of the canisters is completed in a panel by panel sequence starting with panel A (referred to hereafter as 'sequential panel heating'). For some of the modelling cases conducted in this study, we compare the result with 2D modelling study by Yoon et al. (2016a).

7.1. Spatio-temporal distribution of rock temperature increase

The distribution of rock temperature increase at several selected times resulting from simultaneous panel heating is shown in Figure 7-1. Simultaneous heating is rather an unrealistic scenario. However, the impact on the repository is estimated to be the maximum, and therefore this modelling case is suggested as an end-member case.

Figure 7-1 and 7-2 show the temporal and spatial distribution of the temperature increase in the rock mass at different selected times after start of simultaneous and sequential panel heating, respectively. The distributions shown in the vertical and the horizontal sections indicate that the temperature increase is localized at the location of the deposition holes/tunnels at the early stage of heating. The heat propagates outward, and at the same time the temperature in the panel areas decreases. For comparison with the 2D modelling results (Yoon et al. 2016a), Figure 7-3 shows the rock temperature increase simulated by PFC2D.

Rock temperature increase monitored at the centre of panels (Fig.4-9a, points 1-4) at several selected times are shown in Figure 7-4a and in Figure 7-5a, for the simultaneous panel heating and for the sequential panel heating, respectively.

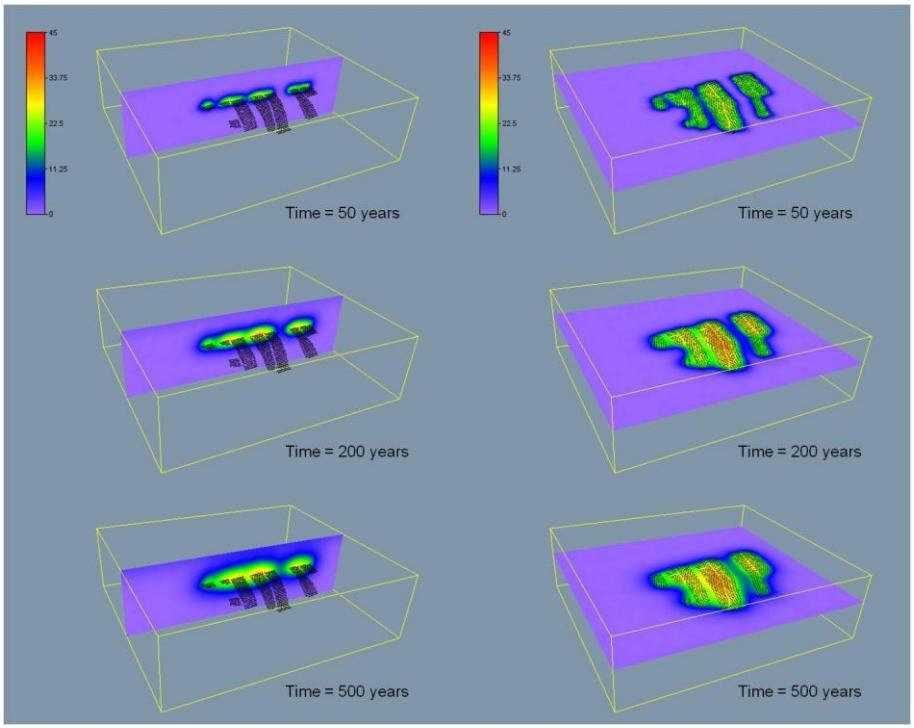

Figure 7-1. Distribution of rock temperature increase at 50 years, 200 years, and 500 years after start of simultaneous panel heating shown on a vertical section (left) and on a horizontal section (right) at the depth of the repository.

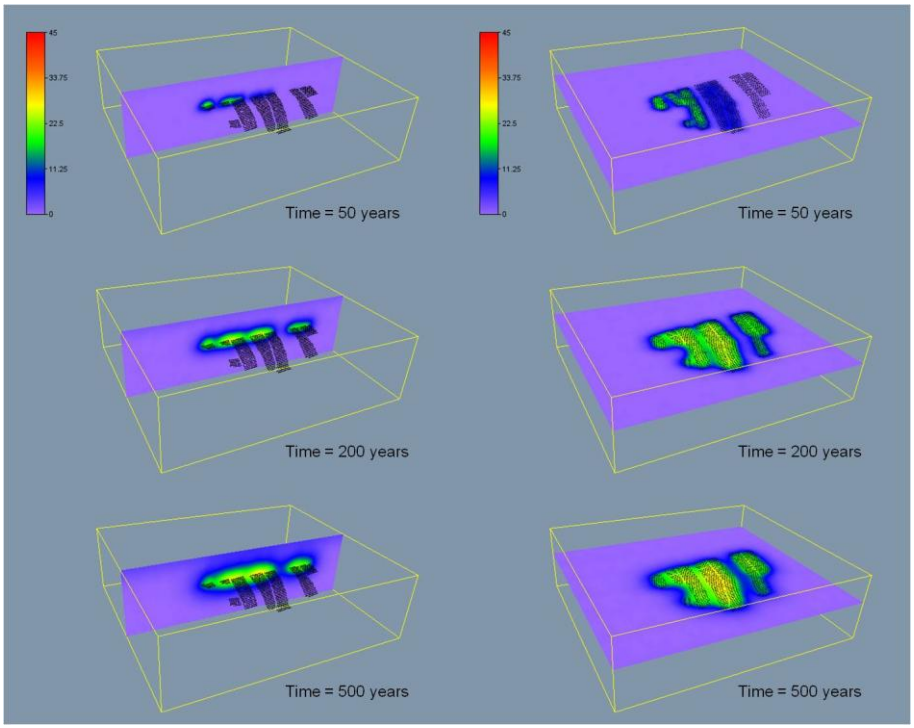

Figure 7-2. Distribution of rock temperature increase at 50 years, 200 years, and 500 years after start of sequential panel heating shown on a vertical section (left) and on a horizontal section (right) at the depth of the repository.

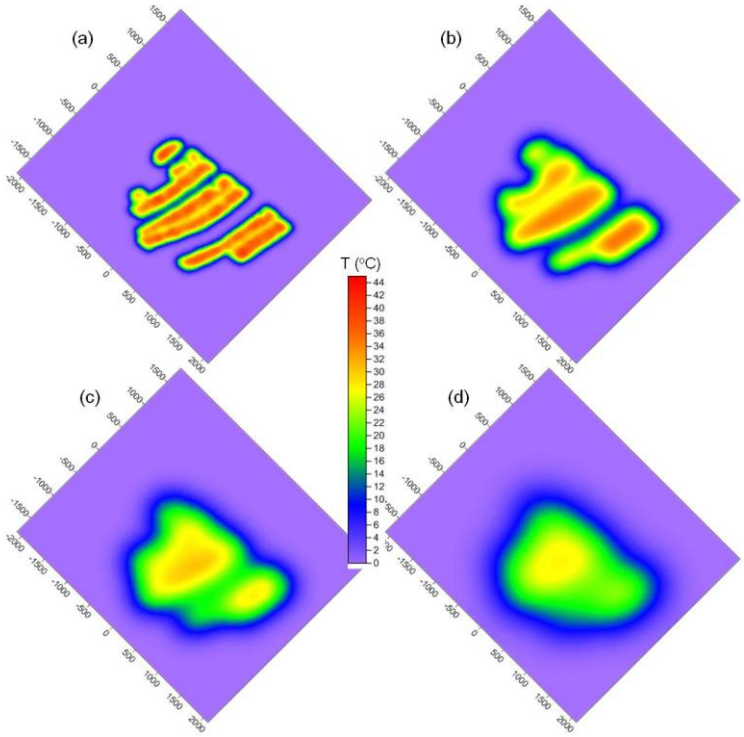

Figure 7-3. Distribution of rock temperature increase at the depth of the repository at (a) 50 years, (b) 200 years, (c) 500 years, and (d) 1000 years after start of simultaneous panel heating from the 2D modelling (modified from Fig.19 in Yoon et al. 2016a).

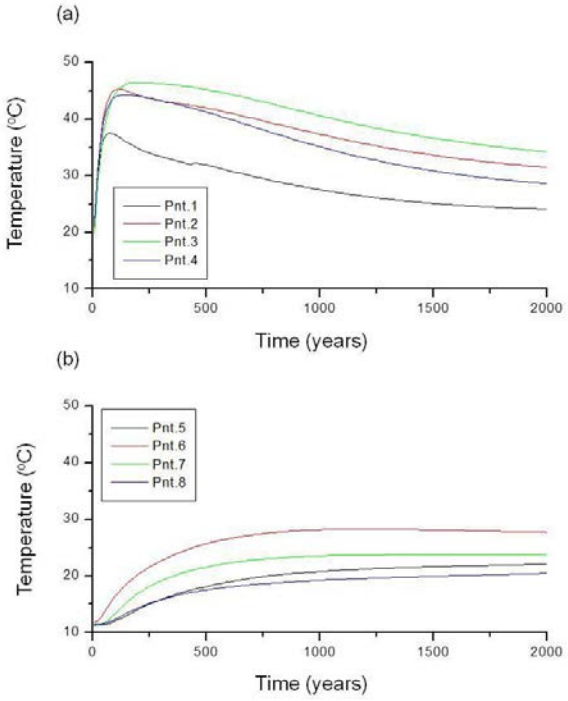

Figure 7-4. Temporal changes in the rock temperature monitored at the selected points (see, Fig.4-9): (a) at the center of the panels, (b) at outskirt of the panels, resulting from simultaneous panel heating.

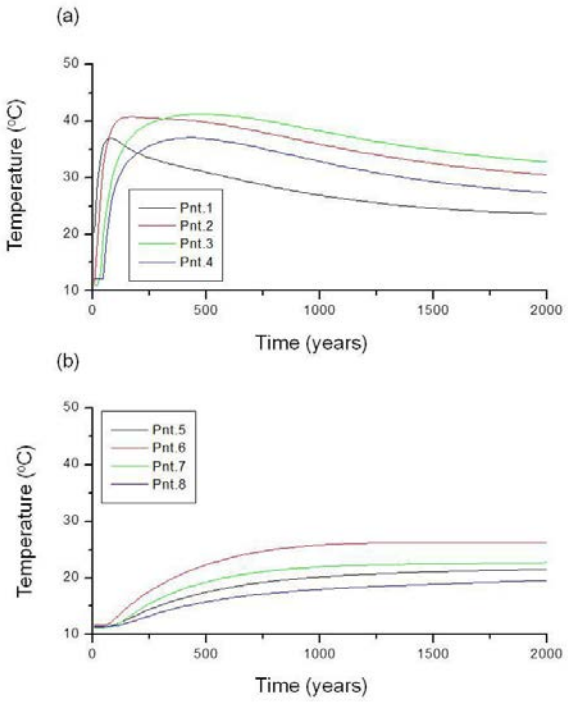

Figure 7-5. Temporal changes in the rock temperature monitored at the selected points (see, Fig.4-9): (a) at the center of the panels, (b) at outskirt of the panels, resulting from sequential panel heating.

7.2. Thermally induced repository fracture shear displacement

Rock temperature increase results in thermal expansion of the rock mass and therefore induces displacement of the embedded fractures. The thermally induced shear displacements of the repository fracture resulting from simultaneous panel heating are shown in Figure 7-6. What is presented in the figure is the average and the standard deviation of the median shear displacements of the repository fractures (those located within the panels and crossing the repository depth). The upper figure is the result of multiple segmented fracture representation (before adjusting with slip volume ratio, $V_{slip,ratio}$, Section 5.3) and the bottom figure is the result of single planar idealization (after adjusting with slip volume ratio). The fracture shear displacement induced by the sequential panel heating is shown in Figure 7-7.

The results show that the thermally induced shear displacements increases rapidly in the early period of the heating (<200 years). At 200 years, the displacement records the peak and then starts decreasing slowly. This is due to the fact that the temperature in the panel area decreases from 200 years.

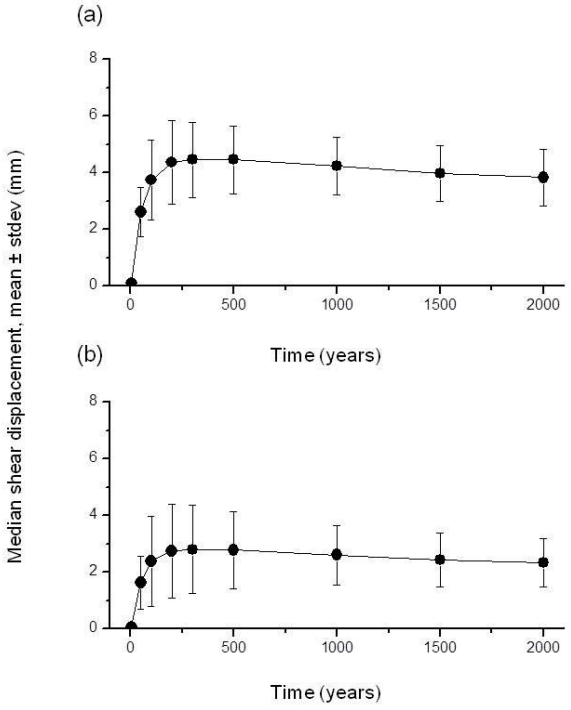

Figure 7-6. Temporal changes of the average and the standard deviation of the median slip displacements of the repository fractures: (a) multiple segmented fracture calculation and (b) single planar idealization calculation, induced by simultaneous panel heating.

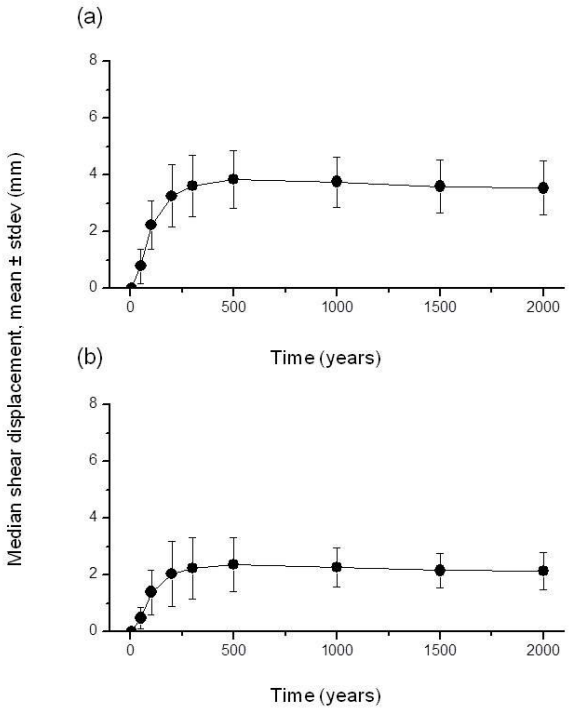

Figure 7-7. Temporal changes of the average and the standard deviation of the median slip displacements of the repository fractures: (a) multiple segmented fracture calculation and (b) single planar idealization calculation, induced by sequential panel heating.

7.3. Summary and discussion

Figure 7-8 shows one result from the 2D modelling of Yoon et al. (2016a), where twenty fractures are randomly selected from the sets of fractures that are within and outside of the panel footprints, and their shear displacements are plotted with time. The figure shows that the shear displacements of the fractures located within the panels increase rapidly during the early time of the heating and reach the maximum at 100 years. The displacements then decrease during the time between 200 and 500 years, and show steady decrease in the long-term.

The fractures located outside the panels show lower rates of displacement increase and reach maximum at 200 years or after. Their displacements then stay at constant values or increase steadily in the long term. It should be noted that the results shown here are the median values of the smooth joint shear displacement comprising the repository fractures.

Comparison between the 3D modelling results (Figs.7-6 and 7-7) and the 2D modelling results (Fig.7-8) demonstrates a qualitative similarity, i.e. rapid increase in early stage of heating (<100-200 years) and long-term slow decrease for the fractures located within the footprints of the panels. The shear displacements of the fractures located outside the footprints of the panels increase slowly in the early stage of the repository heating and show steady increase in the long-term. Slight different in the displacement magnitudes is due to the difference in the fracture complexity and the heat power curves used in the 3D modelling.

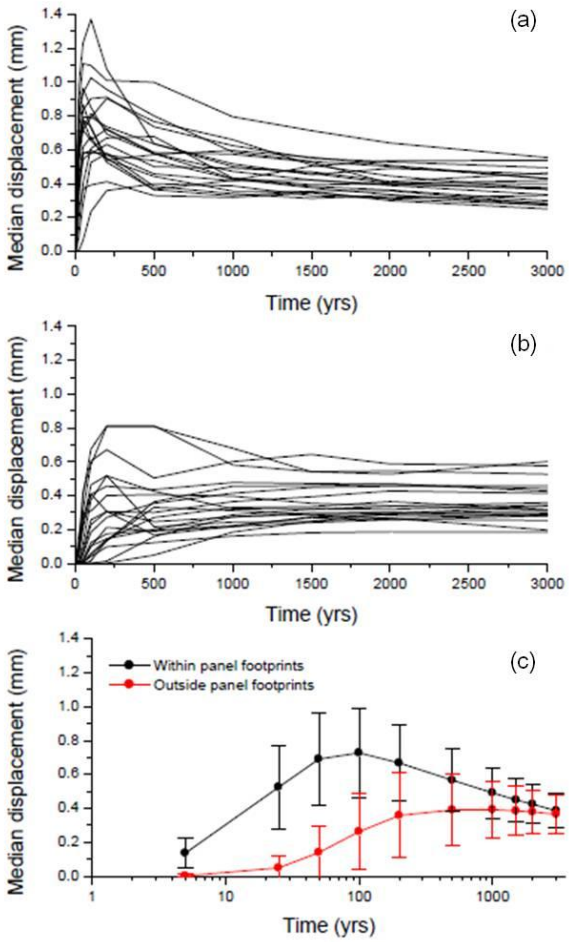

Figure 7-8. Temporal changes of the median shear displacement of 20 randomly chosen fractures (a) within and (b) outside the panel footprints, (c) average and standard deviation of the median displacement of the fractures resulting from 2D modelling study of Yoon et al. (2016a).

The difference can be explained as follows. Firstly, the canister heat power curve used in the 3D modelling is different from that in the 2D modelling. As shown in Figure 4-8, the full-size canister heat power curve (black) was modified to the red one by series of sensitivity analyses. In the 2D modelling study (Yoon et al. 2016a), it was done by varying the parameters, a_i and t_i, in Eqn. (4-5) (see Table 2 in Yoon et al. 2016a), so that the temperature increase distribution resulting from the 2D modelling becomes closer to the results of Hökmark et al. (2010) both in qualitative and quantitative ways (see Fig.4-11). Using the full-size canister heat power curve (black), the fall time of the heat power is significantly delayed which can be more visible in the linear time scale plot as shown in Figure 7-9. In the linear time scale, the modified curve shows that the heat power is almost zero from time t = 100 years, whereas the original curve shows that the heat power is 500 W and decreases slowly over several hundred years. This may be the one reason why the fracture shear displacements show peak at 200-300 years in the 3D modelling.

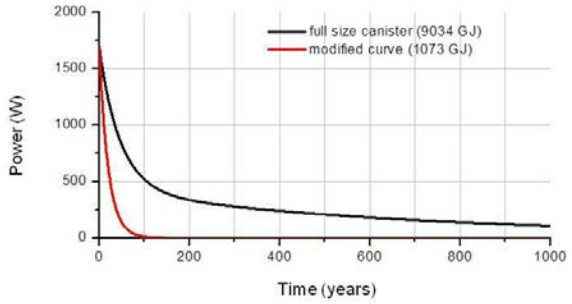

Figure 7-9. Thermal power curve of a full size canister according to SKB (black curve) and the modified one for the PFC2D modelling (red curve) show in a linear time scale plot (identical to Fig.4-8).

Second reason for the long-term steady increase in the shear displacements of the fractures located outside of the panel footprints in the 3D modelling is the fracture density of the DFN, its degree of connectivity, and the dimensionality. In the 3D modelling, the total number of embedded fractures is 685 and they are highly connected and intersecting (Fig.4-5a). However, in the 2D model, total number of the embedded fractures is half of the 3D model (345) and they are distributed on a plane (Fig.4-5b). In the 3D model, heat generated from the panel particles distributes in 3D space with longer time. As shown in Figure 7-4 and Figure 7-5, the temperature increases steadily at the outside the panels. Such temperature increases in the outside of the panels affect the deformations of the fractures, as shown in Figure 7-10 and Figure 7-11, which trigger back the movement of the fractures within the panels. This could be a possible reason for the very slow decrease in the shear displacements of the fractures located within the panel footprints. The results demonstrated that the presence of fractures outside of the panels has influence to the movements of the fractures inside the panels. Also, the temperature increases propagating to above and to below the repository depth results in different levels of thermal stress as the stress field is depth dependent. This could affect the deformation of the fractures that are located above and below the repository depth which also trigger back the movements of the fractures in the panels. Such 3D effect was not taken into account in the 2D modelling, and the reasons explained above could have resulted in differences in the results.

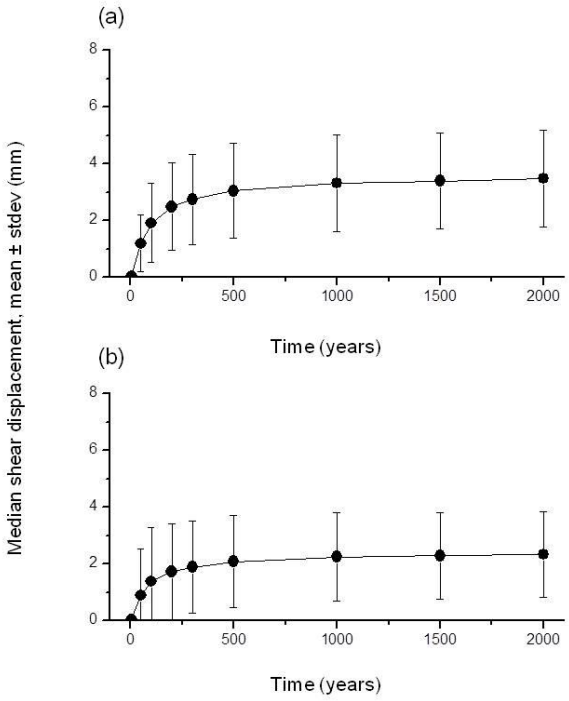

Figure 7-10. Temporal changes of the average and the standard deviation of the median shear displacements of the fractures located outside the panel footprints induced by simultaneous panel heating: (a) multiple segmented and (b) single planar idealization.

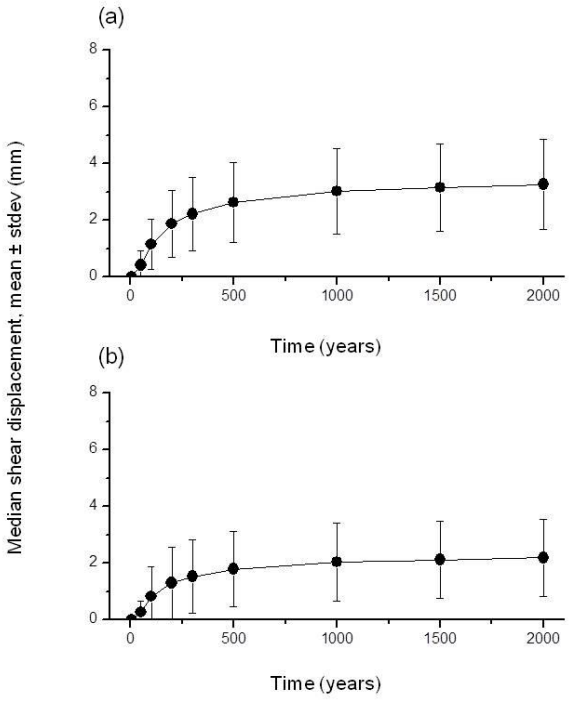

Figure 7-11. Temporal changes of the average and the standard deviation of the median shear displacements of the fractures located outside the panel footprints induced by sequential panel heating: (a) multiple segmented and (b) single planar idealization.

8. Modelling of fault activation and the impact to the repository fractures

We present, in this Chapter, the results of modelling cases where the faults near to the repository are activated under different *in-situ* stress conditions and their seismic impact on the repository fractures is investigated. For some of the modelling cases conducted in this study, we compare the results with those of 2D modelling studies by Yoon et al. (2014, 2017).

8.1. Local Scale Model Simulation

8.1.1. Activation of ZFMWNW0809A under present day *in-situ* stress condition

This modelling case concerns activation of ZFMWNW0809A under present day *in-situ* stress condition. Figure 8-1 shows the coseismic slip distribution of the activated fault. The slip distribution demonstrates that larger slip is concentrated at the inner part of the deformation zone and decreases toward the fault ends. However, the slip is significantly lower at the right part of the deformation zone. This is due to the fact that the deformation zone is intersected by ZFMENE0060A and the slip propagation is shielded by the intersecting fault (slip arrest). From the shear displacements of the smooth joints that compose the fault plane, we chose the median value for a representative slip of the activated fault. The slip of the activated fault is 0.35 m, and the calculated activation magnitude (moment magnitude) is Mw 5.39 using the following equation (Hanks and Kanamori 1979).

$$M_w = \frac{2}{3}\log(GAd_{median}) - 6 \qquad \text{Eqn. (8-1)}$$

where, G is shear modulus (GPa), A is fault surface area (m^2), and d_{median} is median displacement (m) value of the activated fault.

Slip of the repository fractures induced by ZFMWNW0809A activation is shown in Figure 8-2 where the red and green dots correspond to the results of multiple segmented representation and single planar idealization, respectively. Average slip of the repository fractures are 0.420 m and 0.279 m for multiple segmented representation and single planar idealization, respectively. The results are summarized in Table 8-7.

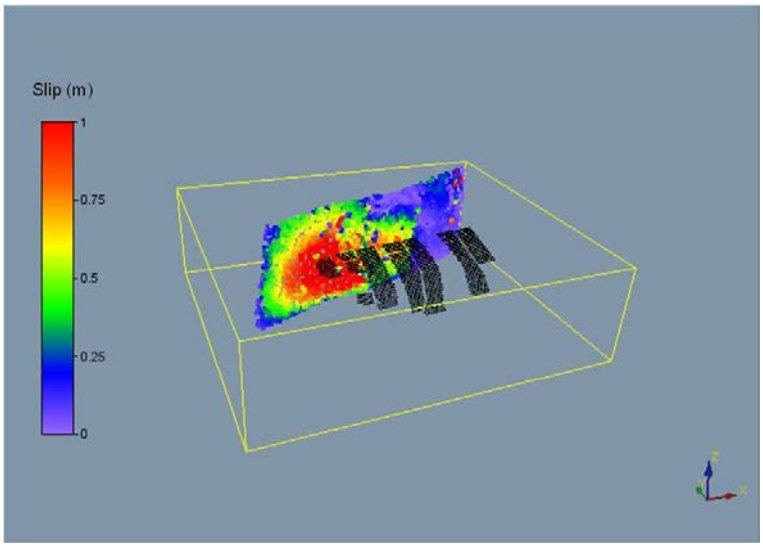

Figure 8-1. Distribution of coseimic slip of ZFMWNW0809A activated under present day *in-situ* stress condition.

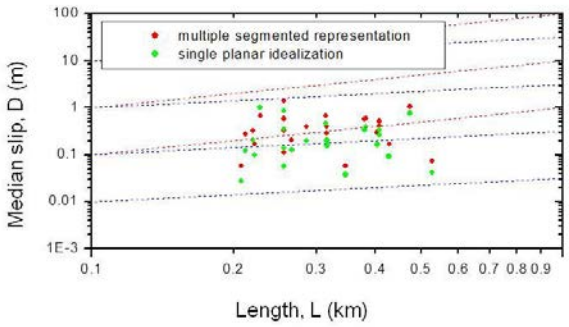

Figure 8-2. Distribution of median slip displacements of the repository fractures (red: multiple segmented representation, green: single planar idealization) induced by activation of ZFMWNW0809A under present day *in-situ* stress condition and comparison with linear length-displacement scaling relations, $D = cL^n$ (red: c = 1e-1, 1e-2, 1e-3 and n = 1; blue: c = 1e-1, 1e-2, 1e-3 and n = 0.5).

8.1.2. Activation of ZFMWNW0809A under glacial ice cover forebulge stress condition

This modelling case concerns activation of ZFMWNW0809A under the effect of forebulge induced by the ice cover. Figure 8-3 shows the coseismic slip distribution of the activated fault. Different patter of slip distribution is observed. The difference may be due to different *in-situ* stress condition, i.e. lowered minimum horizontal stress, which does not lead to concentration of stress at specific location on the fault plane. Slip of the activated fault is 0.15 m, and the calculated activation magnitude is Mw 5.14 (Table 8-7).

Slip of the repository fracture induced by ZFMWNW0809A activation is shown in Figure 8-4 where the red and green dots correspond to the results of multiple segmented representation and single planar idealization, respectively. Average slip

of the repository fractures are 0.035 m and 0.020 m for the multiple segmented representation and single planar idealization, respectively (Table 8-7).

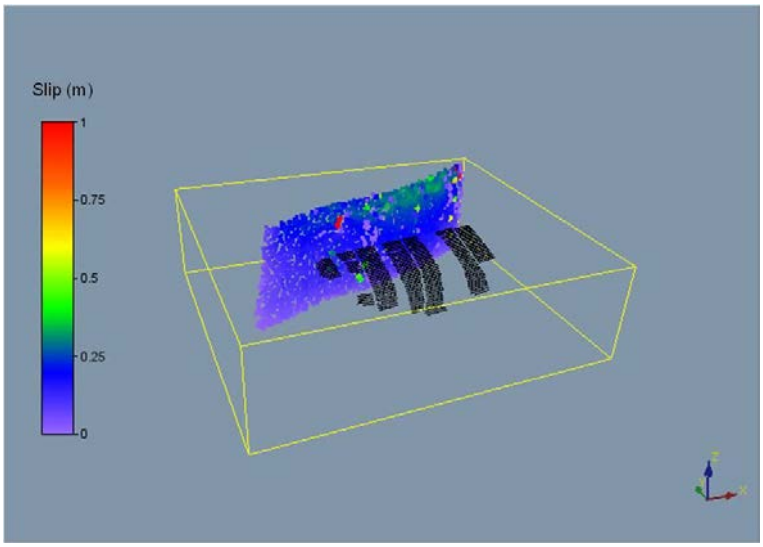

Figure 8-3. Distribution of coseismic slip of ZFMWNW0809A activated under glacial ice cover forebulge stress condition.

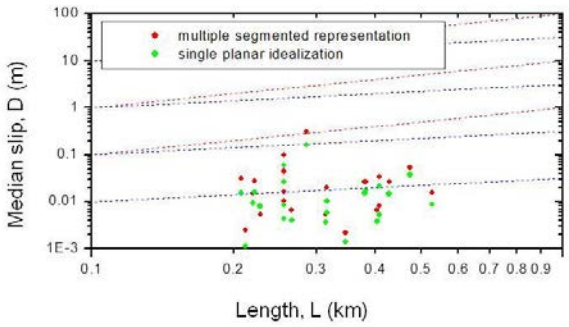

Figure 8-4. Distribution of median slip displacements of the repository fractures (red: multiple segmented representation, green: single planar idealization) induced by activation of ZFMWNW0809A under glacial ice cover forebulge stress condition and comparison with linear length-displacement scaling relations, $D = cL^n$ (red: c = 1e-1, 1e-2, 1e-3 and n = 1; blue: c = 1e-1, 1e-2, 1e-3 and n = 0.5).

8.2. Regional Scale Model Simulation

8.2.1. Activation of ZFMWNW0001 (Singö fault) under present day *in-situ* stress condition

In this modelling case, we simulate Singö fault earthquake occurring under present day *in-situ* stress condition. Figure 8-5 shows the slip magnitudes of the smooth joints that construct the deformation zones. The figure shows that relatively large slip concentrates on the activating fault plane, ZFMWNW0001, and induces relatively large slip at the top of ZFMA2 and ZFMA3, which are gently dipping and crossing the activated fault. On the surface of the activated fault, there exist a large slip contrast at the traces of intersections with ZFMA3 and ZFMA1. Table 8-1 lists the slip of ZFMWNW0001 (primary) and the other faults (secondary), and their magnitudes. The activated slip of ZFMWNW0001 is 0.72 m, and the calculated magnitude is Mw 6.05 (Table 8-7).

The magnitudes of the secondary faults are calculated using Equation 8-1. We assumed that the activation of primary fault is of brittle faulting character and used G = 30 GPa in Equation 8-1. However, for the secondary faults, we used G = 1 GPa following the parameter suggested by Glamheden et al. (2007) where the rock mass deformation properties of the rock in the core of the zone are E_m = 2.5 GPa and v = 0.45. From E_m and v, the calculated G = 1 GPa.

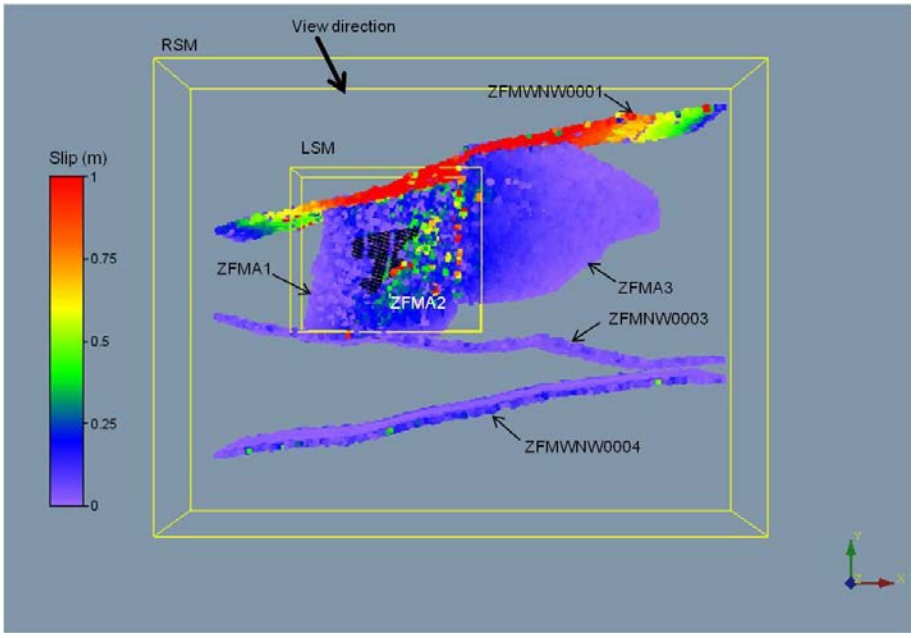

Figure 8-5. Distribution of coseismic slip of the deformation zones in the RSM induced by full plane activation of ZFMWNW0001 under present day *in-situ* stress condition.

Table 8-1. Fault slip and the ratio of secondary to primary fault slip, and the activation magnitudes.

Activation	Deformation zone	Rupture area (km^2)	Slip (m)	Slip ratio[1]	Magnitude (Mw)
Primary[2]	ZFMWNW001 (full plane)	55.14	0.72	NA	6.05
Secondary[3]	ZFMA1	38.36	0.11	0.15	4.42
	ZFMA2	18.34	0.12	0.17	4.23
	ZFMA3	31.48	0.06	0.08	4.18
	ZFMNW0003	55.87	0.03	0.04	4.15
	ZFMWNW0004	52.80	0.02	0.03	4.02

[1] Slip ratio = Secondary fault activation slip / Primary fault activation slip
[2] Assumed brittle activation with shear modulus, *G* = 30 GPa
[3] Shear modulus, *G* = 1 GPa

Slip of the repository fracture induced by activation of ZFMWNW0001 is shown in Figure 8-6, where the multiple segmented representation and single planar idealization results are presented by red and green dots, respectively. Average slip of the repository fractures are 0.037 m and 0.024 m for the multiple segmented representation and single planar idealization, respectively.

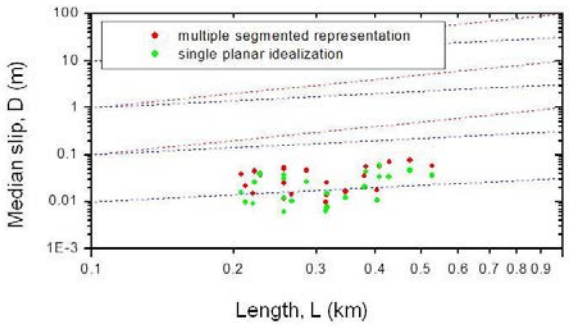

Figure 8-6. Distribution of median slip displacements of the repository fractures (red: multiple segmented representation, green: single planar idealization) induced by full plane activation of ZFMWNW0001 under present day *in-situ* stress condition and comparison with linear length-displacement scaling relations, $D = cL^n$ (red: c = 1e-1, 1e-2, 1e-3 and n = 1; blue: c = 1e-1, 1e-2, 1e-3 and n = 0.5).

8.2.2. Activation of ZFMWNW0001 (Singö fault) under glacial ice cover forebulge stress condition

In this modelling case, we simulate activation of Singö fault under the effect of forebulge induced by the glacial ice cover (glaciations), which makes the *in-situ* stress field more anisotropic. Figure 8-7 shows the coseismic slip magnitudes of the smooth joints composing the deformation zones. The figure shows that relatively large slip concentrates on the activating fault plane, ZFMWNW0001. Also, large slip contrast occurs at the traces of intersections with ZFMA3 and ZFMA1. The slip

magnitude concentrated on the fault plane is larger than those in the previous modelling, i.e. fault activation under present day *in-situ* stress condition. This is due to larger stress anisotropy (SH'/Sh' = 2.7, see Table 4-7) due to the effect of forebulge that lowers the magnitude of the minimum horizontal stress. The fault slip is 1.03 m and the calculated magnitude of activation is Mw 6.15 (Table 8-7).

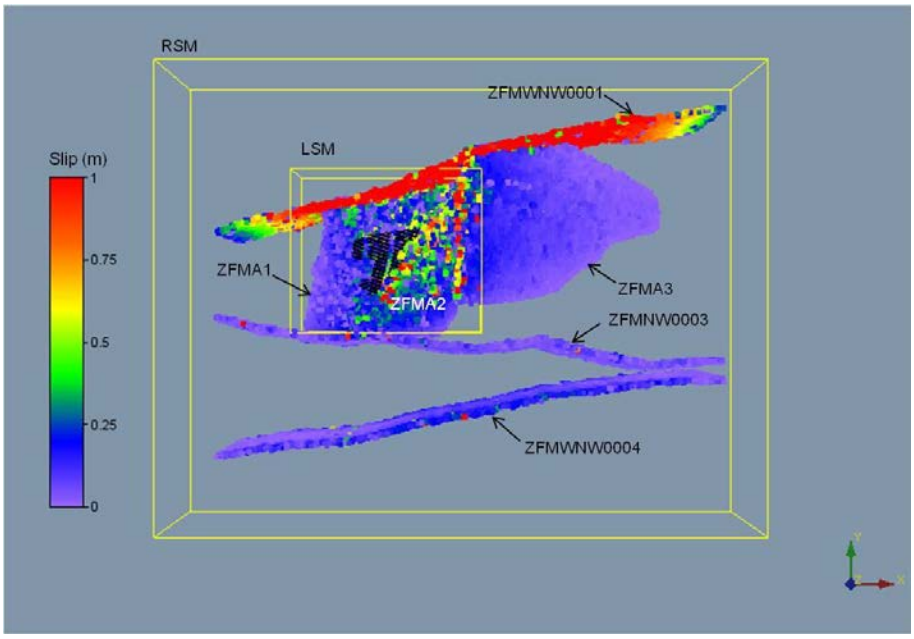

Figure 8-7. Distribution of coseismic slip of the deformation zones in the RSM induced by full plane activation of ZFMWNW0001 under glacial ice cover forebulge stress condition.

Table 8-3 lists the slip of the primary and secondary faults and their magnitudes. Similar to the previous modelling case, it is observed that the amount of slip of the faults near to and connected to the primary fault is larger than that of faults located at the opposite side of the repository (ZFMNW0003 and ZFMWNW0004).

Slip of the repository fracture induced by the activation is shown in Figure 8-8, where the multiple segmented representation and single planar idealization results are presented by red and green dots, respectively. Average slip of the repository fractures are 0.102 m and 0.068 m for the multiple segmented representation and single planar idealization, respectively.

Table 8-3. Fault slip and the ratio of secondary to primary fault slip, and the activation magnitudes.

Activation	Deformation zone	Rupture area (km^2)	Slip (m)	Slip ratio[1]	Magnitude (Mw)
Primary[2]	ZFMWNW001 (full plane)	55.14	1.03	NA	6.15
Secondary[3]	ZFMA1	38.36	0.17	0.17	4.54
	ZFMA2	18.34	0.14	0.14	4.27
	ZFMA3	31.48	0.07	0.07	4.23
	ZFMNW0003	55.87	0.04	0.04	4.23
	ZFMWNW0004	52.80	0.06	0.06	4.33

[1] Slip ratio = Secondary fault activation slip / Primary fault activation slip
[2] Assumed brittle activation with shear modulus, *G* = 30 GPa
[3] Shear modulus, *G* = 1 GPa

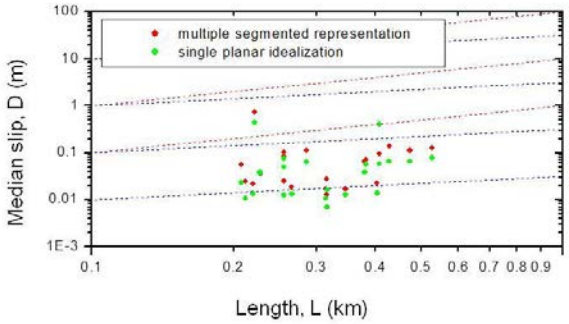

Figure 8-8. Distribution of median slip displacements of the repository fractures (red: multiple segmented representation, green: single planar idealization) induced by full plane activation of ZFMWNW0001 under glacial ice cover forebulge stress condition and comparison with linear length-displacement scaling relations, $D = cL^n$ (red: c = 1e-1, 1e-2, 1e-3 and n = 1; blue: c = 1e-1, 1e-2, 1e-3 and n = 0.5).

8.2.3. Activation of ZFMA2 under present day *in-situ* stress condition

In this modelling case, we simulate activation of ZFMA2, which is gently dipping above the repository rock volume, occurring under present day *in-situ* stress condition. Figure 8-9 shows the slip magnitudes of the smooth joints that compose the deformation zones. The figure shows that relatively large slip concentrates at the top of ZFMA2.

Table 8-4 lists the slip of ZFMA2 (primary) and the other faults (secondary), and their magnitudes. The activated slip of ZFMA2 is 0.32 m and the calculated magnitude is Mw 5.50.

Slip of the repository fracture induced by the activation of ZFMA2 is shown in Figure 8-10, where the multiple segmented representation and single planar idealization results are presented by red and green dots, respectively. Average slip of

the repository fractures are 0.037 m and 0.024 m for the multiple segmented representation and single planar idealization, respectively.

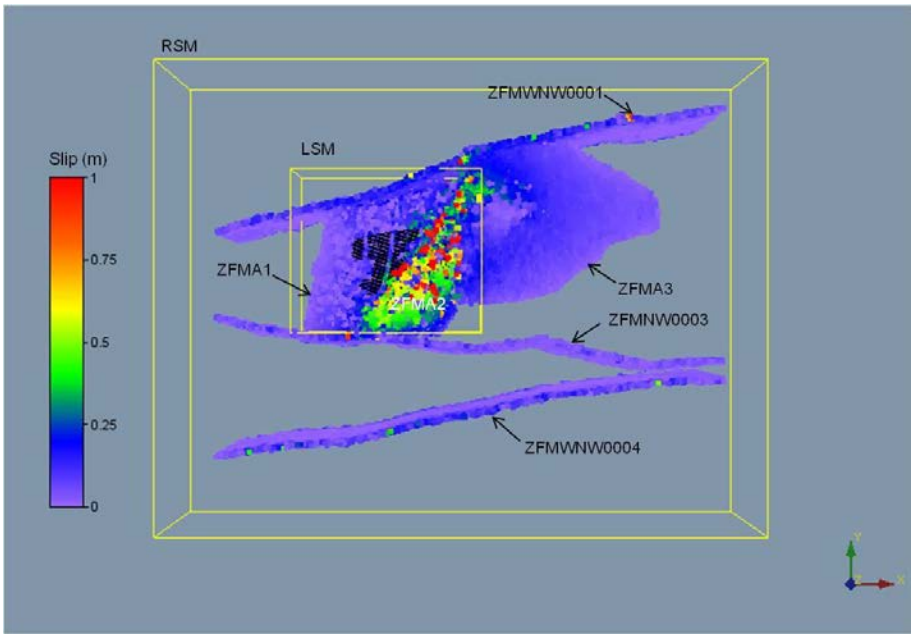

Figure 8-9. Distribution of coseismic slip of the deformation zones in the RSM induced by full plane activation of ZFMA2 under present day *in-situ* stress condition.

Table 8-4. Fault slip and the ratio of secondary to primary fault slip, and the activation magnitudes.

Activation	Deformation zone	Rupture area (km^2)	Slip (m)	Slip ratio[1]	Magnitude (Mw)
Primary[2]	ZFMA2 (full plane)	18.34	0.32	NA	5.50
Secondary[3]	ZFMA1	38.36	0.08	0.25	4.32
	ZFMA3	31.48	0.08	0.25	4.27
	ZFMNW0003	55.87	0.02	0.06	4.03
	ZFMWNW0001	55.14	0.03	0.09	4.15
	ZFMWNW0004	52.80	0.02	0.06	4.02

[1] Slip ratio = Secondary fault activation slip / Primary fault activation slip
[2] Assumed brittle activation with shear modulus, G = 30 GPa
[3] Shear modulus, G = 1 GPa

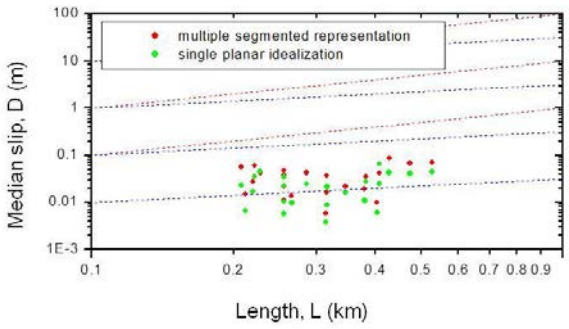

Figure 8-10. Distribution of median slip displacements of the repository fractures (red: multiple segmented representation, green: single planar idealization) induced by full plane activation of ZFMA2 under present day *in-situ* stress condition and comparison with linear length-displacement scaling relations, $D = cL^n$ (red: c = 1e-1, 1e-2, 1e-3 and n = 1; blue: c = 1e-1, 1e-2, 1e-3 and n = 0.5).

8.2.4. Activation of ZFMA3 under present day *in-situ* stress condition

In this modelling case, we simulate activation of ZFMA3, which is gently dipping above the repository rock volume but placed some distance from the repository, occurring under present day *in-situ* stress condition. Figure 8-11 shows the slip magnitudes of the smooth joints that compose the deformation zones. The figure shows that large slip concentrates at the top of ZFMA3, and the slip decreases with dipping towards the fault end. Table 8-5 lists the slip of ZFMA3 (primary) and the other faults (secondary), and their magnitudes. The activated slip of ZFMA3 is 0.44 m and the calculated moment magnitude is Mw 5.75. Compared to ZFMA1 which is also gently dipping but below the repository rock volume, the amount of induced slip of ZFMA2 (0.11 m) is larger than that of ZFMA1 (0.08 m). This is due to the fact that ZFMA2 is close to and connected to ZFMA3.

Slip of the repository fracture induced by full plane activation of ZFMA3 is shown in Figure 8-12, where the multiple segmented representation and single planar idealization results are presented by red and green dots, respectively. Average slip of the repository fractures are 0.031 m and 0.020 m for the multiple segmented representation and single planar idealization, respectively.

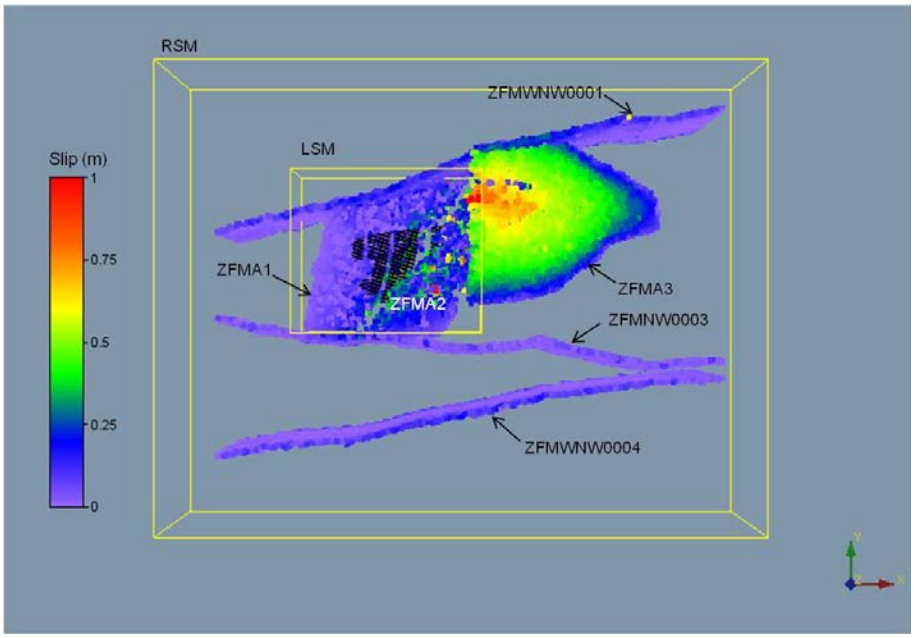

Figure 8-11. Distribution of coseismic slip of the deformation zones in the RSM induced by full plane activation of ZFMA3 under present day *in-situ* stress condition.

Table 8-5. Fault slip and the ratio of secondary to primary fault slip, and the activation magnitudes.

Activation	Deformation zone	Rupture area (km^2)	Slip (m)	Slip ratio[1]	Magnitude (Mw)
Primary[2]	ZFMA3 (full plane)	31.48	0.44	NA	5.75
Secondary[3]	ZFMA1	38.36	0.08	0.18	4.32
	ZFMA2	18.34	0.11	0.25	4.20
	ZFMNW0003	55.87	0.02	0.05	4.03
	ZFMWNW0001	55.14	0.03	0.07	4.15
	ZFMWNW0004	52.80	0.02	0.05	4.02

[1] Slip ratio = Secondary fault activation slip / Primary fault activation slip
[2] Assumed brittle activation with shear modulus, *G* = 30 GPa
[3] Shear modulus, *G* = 1 GPa

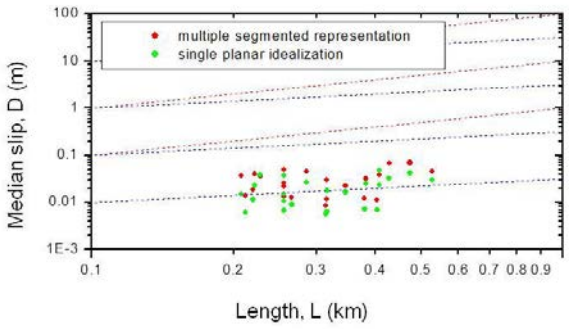

Figure 8-12. Distribution of median slip displacements of the repository fractures (red: multiple segmented representation, green: single planar idealization) induced by full plane activation of ZFMA3 under present day *in-situ* stress condition and comparison with linear length-displacement scaling relations, $D = cL^n$ (red: c = 1e-1, 1e-2, 1e-3 and n = 1; blue: c = 1e-1, 1e-2, 1e-3 and n = 0.5).

8.2.5. Activation of ZFMA3 under glacial ice cover retreat stress condition

In this modelling case, we simulate activation of ZFMA3 occurring under the effect of retreating ice cover. Figure 8-13 shows the coseismic slip magnitudes of the smooth joints that compose the deformation zones. The figure shows that relative large slip concentrates at the top of ZFMA3, and the slip decreases with dipping towards the fault ends. Comparing with the previous modelling, the slip magnitude is higher, which is due to the fact that the stress condition becomes more favorable for reverse faulting in the direction of maximum horizontal stress (SH'/Sv' = 5.4 and Sh'/Sv' = 2.9, see Table 4-7).

Table 8-6 lists the slip of ZFMA3 (primary) and the other faults (secondary), and their magnitudes. The activated slip of ZFMA3 is 0.63 m and the calculated moment magnitude is Mw 5.85.

Slip of the repository fracture induced by full plane activation of ZFMA3 is shown in Figure 8-14, where the multiple segmented representation and single planar idealization results are presented by red and green dots, respectively. Average slip of the repository fractures are 0.051 m and 0.033 m for the multiple segmented representation and single planar idealization, respectively. These slip displacements are almost double of those in the previous modelling case. The results demonstrate that instability of the gently dipping faults and its impact to the repository fractures is large at the time when the glacial ice cover retreats (an earthquake event during deglaciation).

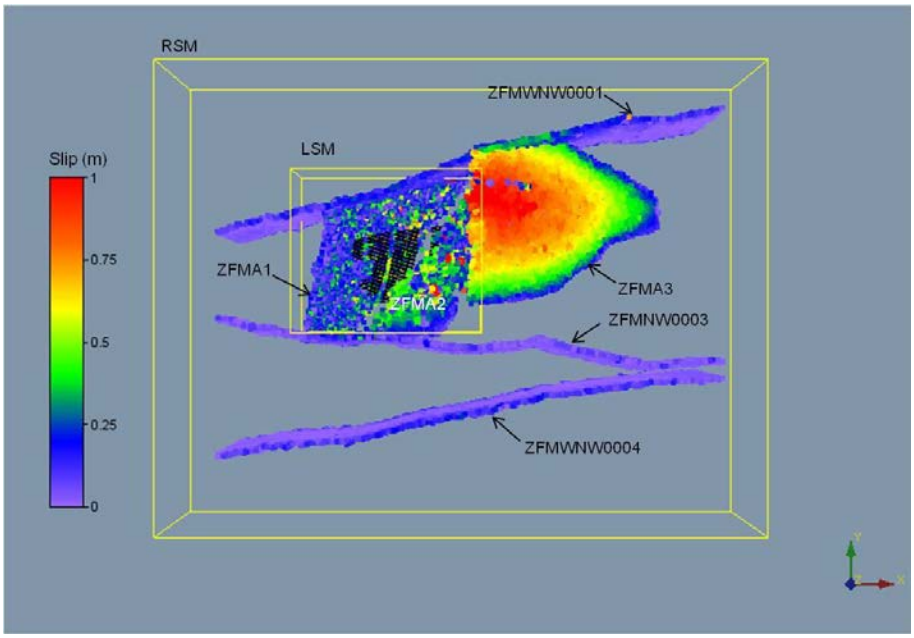

Figure 8-13. Distribution of coseismic slip of the deformation zones in the RSM induced by full plane activation of ZFMA3 under glacial ice cover retreat stress condition.

Table 8-6. Fault slip and the ratio of secondary to primary fault slip, and the activation magnitudes.

Activation	Deformation zone	Rupture area (km^2)	Slip (m)	Slip ratio[1]	Magnitude (Mw)
Primary[2]	ZFMA3 (full plane)	31.48	0.63	NA	5.85
Secondary[3]	ZFMA1	38.36	0.20	0.32	4.59
	ZFMA2	18.34	0.18	0.29	4.35
	ZFMNW0003	55.87	0.03	0.05	4.15
	ZFMWNW0001	55.14	0.04	0.06	4.23
	ZFMWNW0004	52.80	0.02	0.03	4.02

[1] Slip ratio = Secondary fault activation slip / Primary fault activation slip
[2] Assumed brittle activation with shear modulus, *G* = 30 GPa
[3] Shear modulus, *G* = 1 GPa

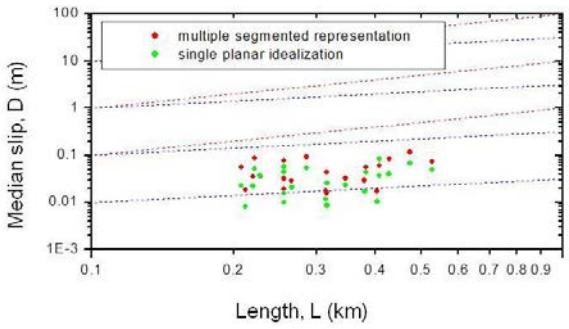

Figure 8-14. Distribution of median slip displacements of the repository fractures (red: multiple segmented representation, green: single planar idealization) induced by full plane activation of ZFMA3 under glacial ice cover retreat stress condition and comparison with linear length-displacement scaling relations, $D = cL^n$ (red: c = 1e-1, 1e-2, 1e-3 and n = 1; blue: c = 1e-1, 1e-2, 1e-3 and n = 0.5).

8.3. Summary and discussion

For some of modelling cases, we compare the results with those of the 2D modelling of Yoon et al. (2014). The first comparison concerns the repository fracture shear displacement induced by activation of ZFMWNW0809A under present day *in-situ* stress condition. Figure 8-15 compares two data sets. Grey dots are the shear displacements of the repository fractures that are computed from the 2D modelling study (Yoon et al. 2017) induced by full trace activation of ZFMWNW0809A under present day *in-situ* stress condition. Black dots are the results of the 3D modelling in this study. The results demonstrate that the shear displacements of the repository fractures in the 3D model are larger than those of the 2D model by maximum five orders of magnitudes, and in average by three orders of magnitudes. The reasons for such large difference are as follows.

Firstly, the fault activation magnitude in the 3D model is larger than that of 2D model (Mw 5.39 in 3D vs. Mw >4 in 2D, activation magnitude in 2D model is discussed later in Fig.8-16).

Secondly, the total number of fractures modelled in the 3D model (685) is larger than that of 2D model (347). Therefore, the connectivity and the complexity of the fracture network is significantly larger than that of 2D model, which could have resulted in overall larger slip of the fractures induced by the fault activation.

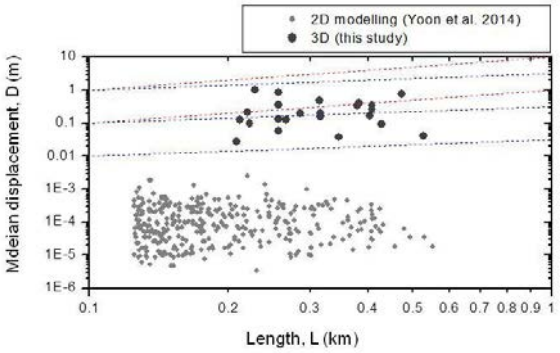

Figure 8-15. Comparison of the median slip displacements of the repository fracture induced by full trace activation of ZFMWNW0809A in 2D modelling (grey dots) and by activation in 3D modelling (black dots) and comparison with linear length-displacement scaling relations, $D = cL^n$ (red: c = 1e-1, 1e-2, 1e-3 and n = 1; blue: c = 1e-1, 1e-2, 1e-3 and n = 0.5).

Table 8-7. Median slip and magnitudes of the activated faults in the LSM and in the RSM under different stress conditions (RA: Rupture area of the active fault; D_{med}: Median slip of the active fault; Mw: Moment magnitude of the fault activation; $D_{f,med}$: Average of the median slip displacement of the repository fractures that are presented in the length vs. displacement plots: multiple segmented representation and single planar idealization).

	In situ stress	Primary fault	RA (km^2)	D_{med} (m)	Mw	$D_{f,med}$ (m)
LSM	Present day	ZFMWNW0809A (full plane)	11.42	0.35	5.39	0.420 0.279
	Ice cover forebulge	ZFMWNW0809A (full plane)	11.42	0.15	5.14	0.035 0.020
RSM	Present day	ZFMWNW0001 (full plane)	55.14	0.72	6.05	0.037 0.024
	Ice cover forebulge	ZFMWNW0001 (full plane)	55.14	1.03	6.15	0.102 0.068
	Present day	ZFMA2 (full plane)	18.34	0.32	5.50	0.037 0.024
	Present day	ZFMA3 (full plane)	31.48	0.44	5.75	0.031 0.020
	Ice cover retreat	ZFMA3 (full plane)	31.48	0.63	5.85	0.051 0.033

The 3D modelling results are compared in Figure 8-16 with the global tectonic earthquake fault data from Wells and Coppersmith (1994) and Manighetti et al. (2005) and the results of 2D modelling study of Yoon et al. (2017). The 2D modelling results are represented in three different variations by taking into account of three levels of ratios between the fault plane length (L) to the fault plane height (H), L/H = 1/1, 3/1, and 6/1, which are represented by black, red and blue diamonds.

The results of activation of ZFMWNW0809A, ZFMWNW0001, ZFMA2 are shown by different symbols (ZFMWNW0809A: triangle; ZFMWNW0001: square; ZFMA2: reversed triangle; ZFMA3: star) which all fit well to the regression lines of Wells and Coppersmith (1994).

The activation magnitude of ZFMWNW0809A in the 2D model is Mw 4.6 (grey diamond) with assumption that the fault size is 14.3 km^2 (Yoon et al. 2017). The assumed fault surface area is larger than that of the 3D fault model (11.42 km^2), but the activation magnitude is smaller than in the 3D model (black triangles). This is due to the fact that the ratio between the fault length and the height (L/H) is assumed 1:1 in the 2D modelling study. However, this assumption is considered unrealistic as most of the earthquake faults do not have L/H = 1:1 ratio (Yoon et al. 2017) but rather L/H = 3~6:1. Therefore, it is considered reasonable if the activation magnitude of ZFMWNW0809A is Mw 4.4 (red diamond) or below (blue diamond).

Figure 8-17 shows another set of results from 3DEC synthetic earthquake modelling under end-glacial stress conditions and for present day stress condition applied to Olkiluoto site in Finland (Fälth and Hökmark 2011, 2012). The figure shows also that the resulting moment magnitudes are above the area-magnitude regression by Wells and Coppersmith (1994) and Leonard (2010). The results of PFC3D modelling of activation of ZFMA2 are compared with those of 3DEC modelling (Fälth et al. 2015) in Table 8-8. Despite the difference in the numerical model, in the way of simulating a fault rupture and in other conditions, e.g. stress field, the magnitude and the slip displacement associated with activation of ZFMA2 are comparable.

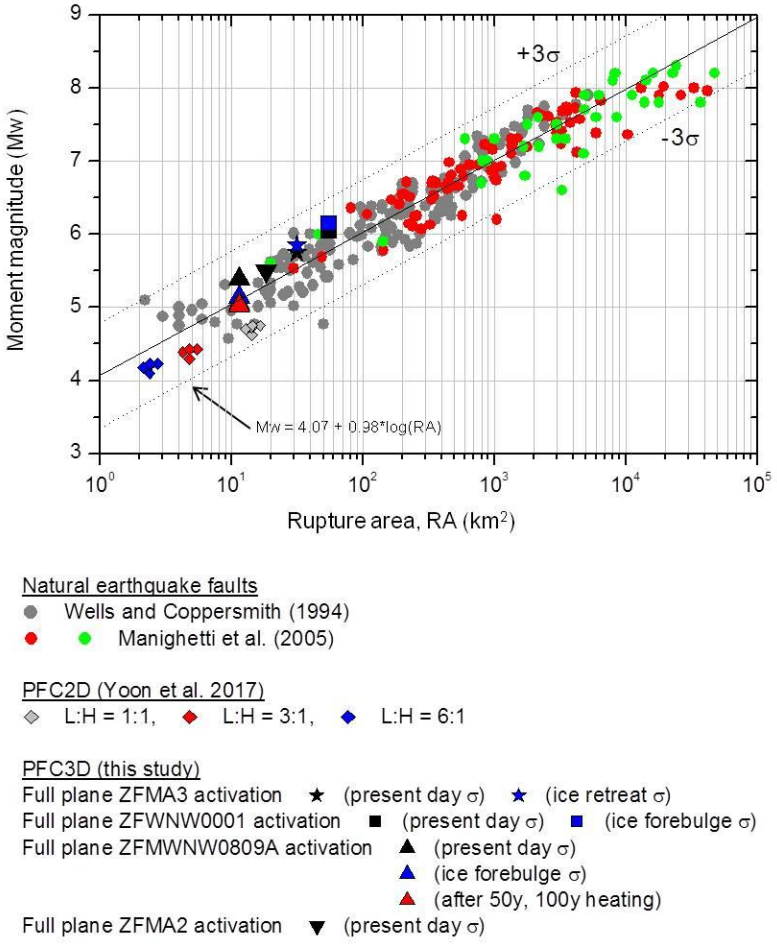

Figure 8-16. Relation between the fault rupture area (RA) and moment magnitude (Mw) of earthquake faults (Wells and Coppersmith 1994; Manighetti et al. 2005) and the results from the 2D modelling study of Yoon et al. (2017) and from the 3D modelling in this study.

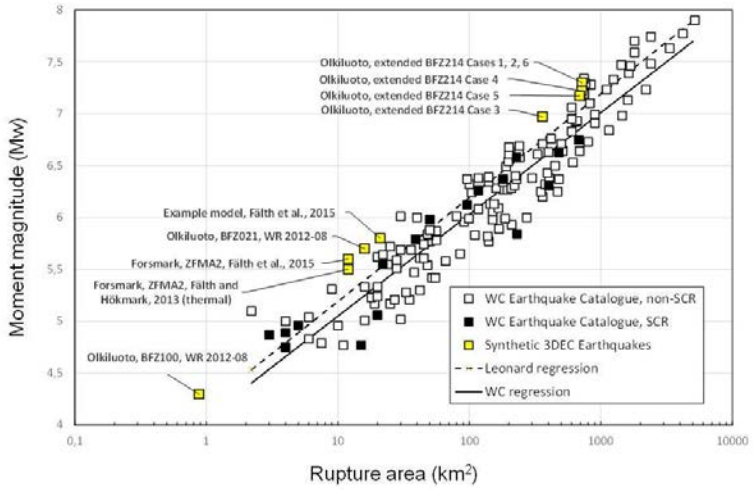

Figure 8-17. Results of 3DEC synthetic earthquake modelling by Fälth et al. (2011, 2012) plotted with data from Wells and Coppersmith (1994).

Table 8-8. Comparison of 3DEC (Fälth et al. 2015) and PFC3D modelling of ZFMA2 activation.

	3DEC	PFC3D
Fault rupture area, A (km^2)	12	18.34
Fault slip displacement, d (m)	0.97	0.32
Moment magnitude, Mw	5.6	5.50
Stress field	End-glacial	Present day
Reference	Fälth et al. (2015)	This study

Figure 8-18a shows the slip distribution of ZFMWNW0001 activated under present day *in-situ* stress condition. The entire fault plane was activated for this case. However, the figure shows a large contrast of slip distribution in the fault plane between the left and the right parts of the trace where the fault is intersected by ZFMA1. Such large contrast in slip distribution can be also found in other studies, e.g. Nixon et al. (2004), especially when the faults are intersected by neighboring faults as shown in Figure 8-18b.

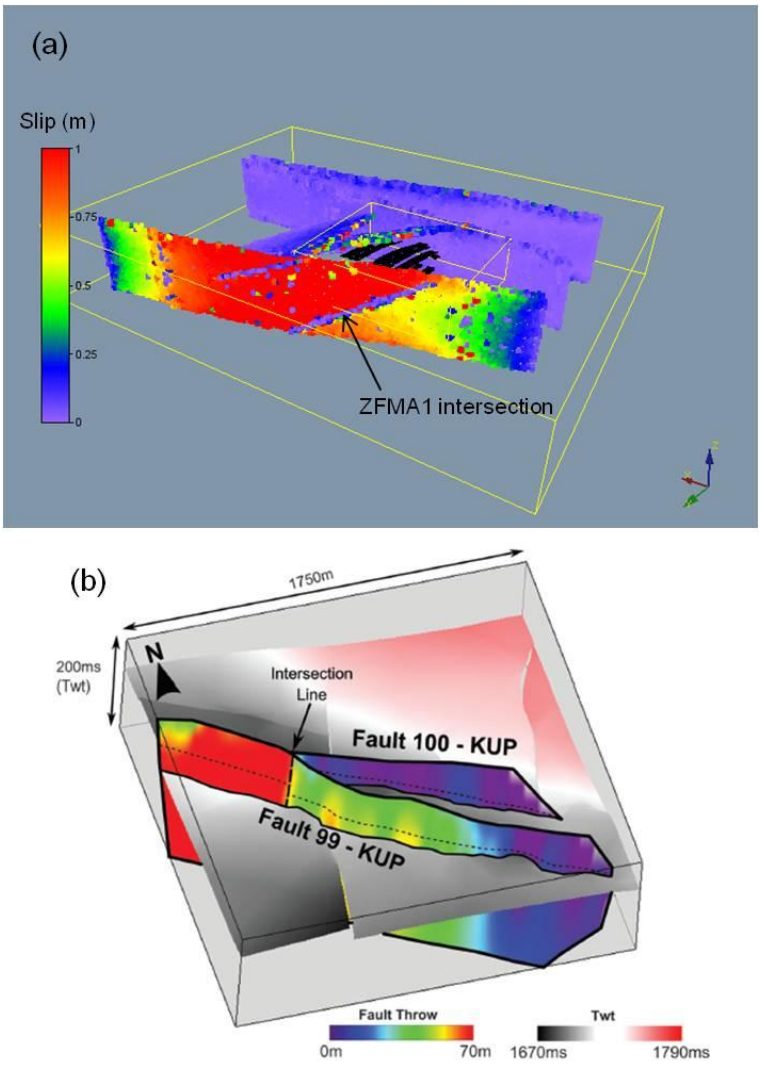

Figure 8-18. (a) Slip distribution of fault ZFMWNW0001 intersected by the gently dipping faults, (b) 3-D diagram showing the distribution of throw on the fault planes of a splay fault and its associated main fault (Nixon et al. 2014).

Temporal changes in the slip distribution are investigated. Figure 8-19 show temporal variation of slip distribution of ZFMWNW0809A after activation under present day *in-situ* stress condition. Although we simulated the full plane activation, the figure shows that the slip is concentrated at one spot and propagates outward. The high concentration of slip after activation is due to concentration of stress at one specific location (smooth joint) on the fault plane under the given stress field. However, the propagation of slip is blocked at the trace where the fault is intersected by ZFMENE0060A, which was similarly simulated in the RSM as shown in Figure 8-18a.

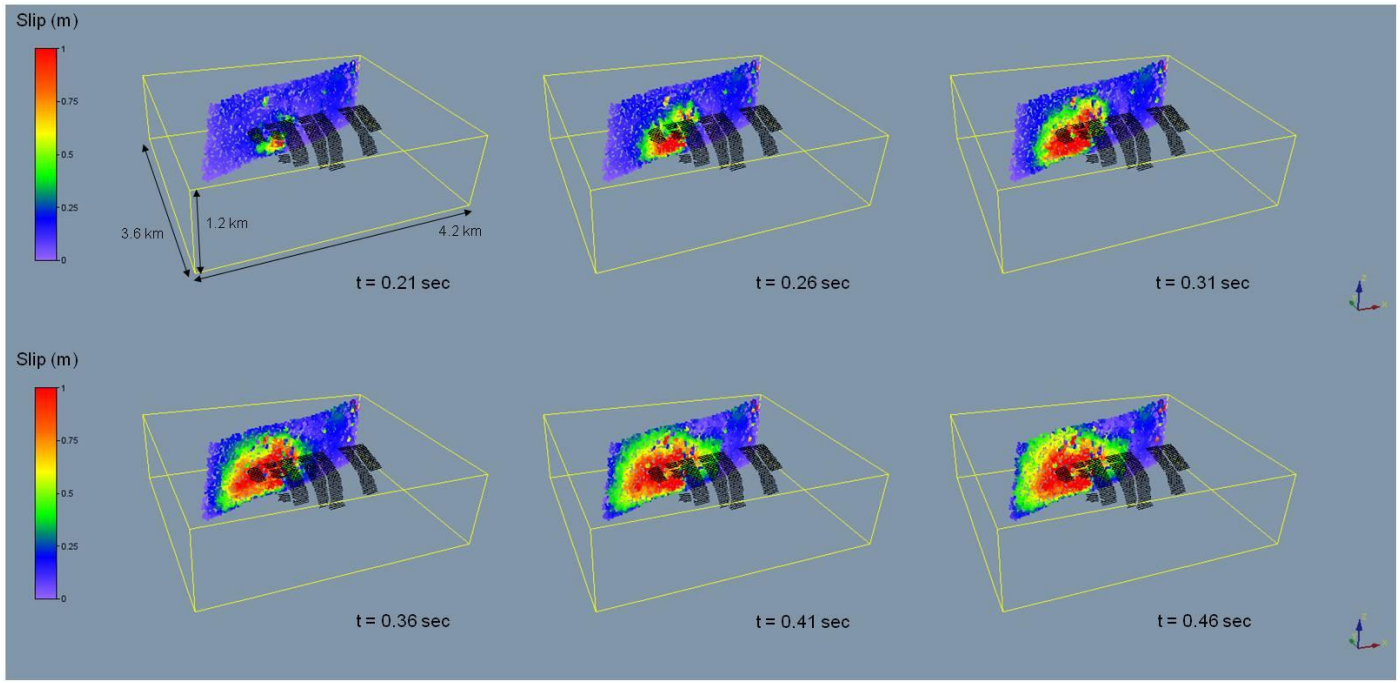

Figure 8-19. Temporal changes in the slip distribution of ZFMWNW0809A activated under present day *in-situ* stress condition.

Coseismic slip profiles of the activated faults are examined. Figure 8-20 shows the interpolated fields of the shear displacement of (a, b) ZFMWNW001 and (c, d) ZFMWNW0809A that are activated under the present day *in-situ* stress condition.

The fault slip at the depth of the repository is obtained by the scanlines and plotted in Figure 8-20b and 8-20d. The slip distribution of ZFMWNW0809A shows overall triangular and asymmetric pattern, and locally large increase and drop. This is also the case in the slip distribution of ZFMWNW0001, and especially at the location where ZFMWNW0001 intersects ZFMA1.

Such triangular and asymmetric slip patterns agree well with general slip profiles of earthquake faults shown in Figure 8-21 (Cappa et al. 2014). The simulated results also show high resemblance to the slip profiles of Landers earthquake and Hector Mine earthquake shown in Figure 5-19.

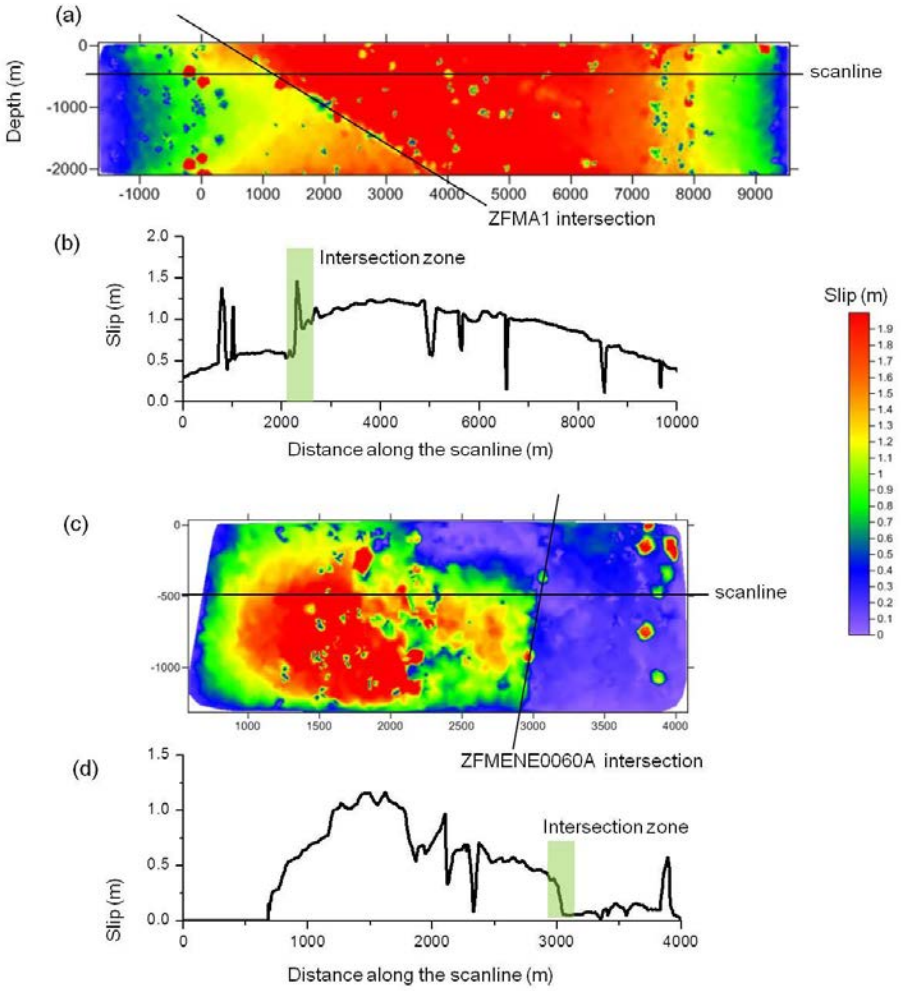

Figure 8-20. Interpolated fields of slip distribution of (a) ZFMWNW0001 and (c) ZFMWNW0809A after full plane activation under present day stress condition and slip profiles along the scanlines at the depth of the repository.

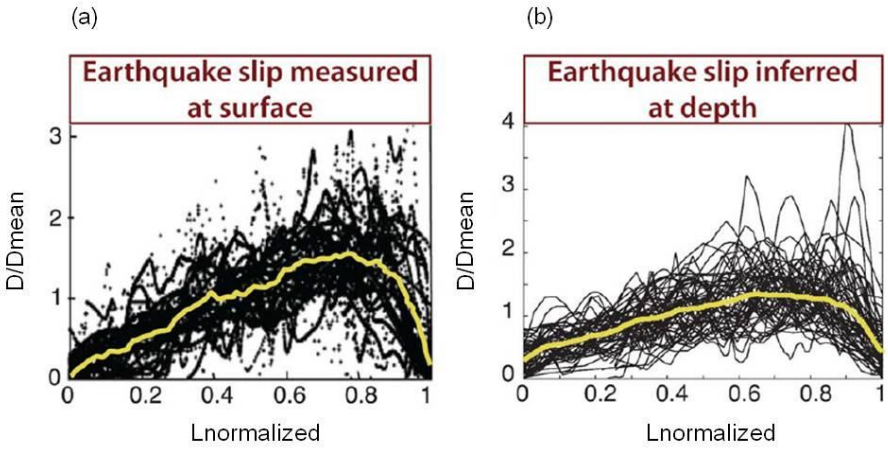

Figure 8-21. Earthquake slip profiles (normalized) (a) measured at the ground surface and (b) inferred at depth from the earthquake source inversion models for ca. 50 different historical earthquakes (Cappa et al. 2014).

9. Modelling of fault activation under repository heat and the impact on the repository fractures

9.1. LSM – Activation of ZFMWNW0809A under present day *in-situ* stress condition and after 50 years of simultaneous panel heating

This modelling case concerns activation of ZFMWNW0809A under present day *in-situ* stress condition and 50 years after start of simultaneous panel heating, i.e. 50 years after completion of canister depositions in all deposition holes.

Slip of the repository fracture induced by 50 years of repository heating is shown in Figure 9-1a where the red and the green dots correspond to the results of multiple segmented representation and single planar idealization, respectively.

Slip of the repository fracture induced by ZFMWNW0809A activation is shown in Figure 9-1b where the red and the green dots correspond to the results of multiple segmented representation and single planar idealization, respectively. Average slip of the repository fractures are 0.011 m and 0.007 m for the multiple segmented representation and single planar idealization, respectively.

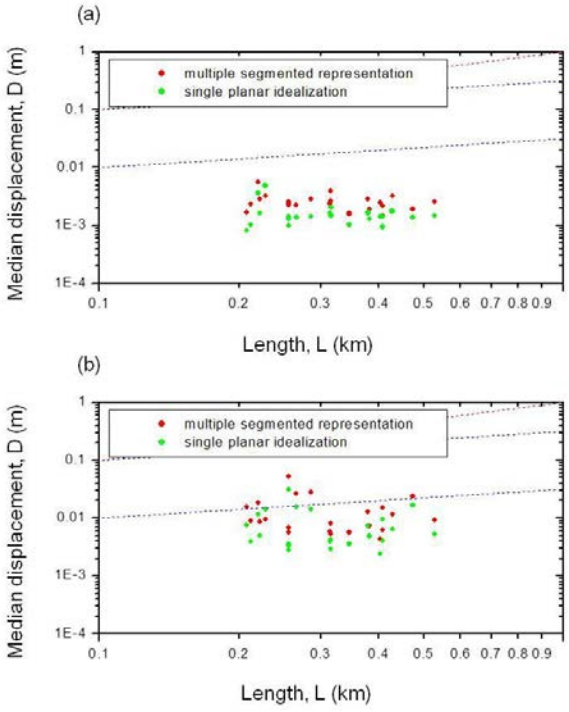

Figure 9-1. Distribution of the median slip displacements of the repository fractures (red: multiple segmented representation, green: single planar idealization) induced by (a) 50 years of simultaneous heating and by (b) activation of ZFMWNW0809A under present day *in-situ* stress condition.

The results show that the displacements of the repository fractures increase in three orders of magnitude. Based on the slip values of the smooth joints that compose the fault plane, the slip of the activated fault is 0.11 m, and the calculated activation magnitude is Mw 5.05 (Table 9-1).

9.2. LSM – Activation of ZFMWNW0809A under present day *in-situ* stress condition and after 100 years of simultaneous panel heating

This modelling case concerns activation of ZFMWNW0809A under present day *in-situ* stress condition and 100 years after start of simultaneous panel heating, i.e. 100 years after completion of canister depositions in all deposition holes.

Slip of the repository fracture induced by 100 years of repository heating is shown in Figure 9-2a where the red and the green dots correspond to the results of multiple segmented representation and single planar idealization, respectively.

Slip of the repository fracture induced by ZFMWNW0809A activation is shown in Figure 9-2b where the red and green dots correspond to the results of multiple segmented fractures and single planar idealization, respectively. Average slip of the repository fractures are 0.057 m and 0.001 m for the multiple segmented representation and single planar idealization, respectively. Based on the slip values of the smooth joints, the mean slip of the activated fault is 0.10 m, and the calculated activation magnitude is Mw 5.02 (Table 9-1).

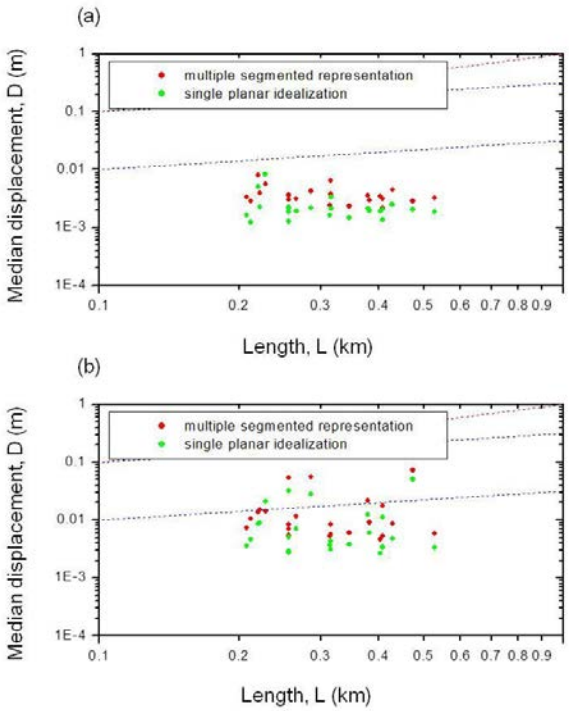

Figure 9-2. Distribution of the median slip displacements of the repository fractures (red: multiple segmented representation, green: single planar idealization) induced by (a) 100 years of simultaneous heating and by (b) activation of ZFMWNW0809A under present day stress condition.

9.3. Summary and discussion

The results presented in Chapter 9 show that the activation magnitude of ZFMWNW0809A after tens of years of repository heating is lowered than the activation magnitude without the repository heating (Table 9-1).

This is may be due to the fact that the initial stress field in the repository rock mass is disturbed by the deformation of the repository fractured induced by the heating. The disturbed stress field could also have effects on the nearby fault stability by changing the orientation of the maximum stress. We monitored the stress field at the center of the repository rock mass and presented the results in Table 9-2.

Table 9-1. Median slip and magnitudes of ZFMWNW0809A activation, average of the median slip displacement of the repository fractures that are presented in the length vs. displacement plots: multiple segmented representation and single planar idealization).

Activation of ZFMWNW0809	D_{med} (m)	Mw	$D_{f,med\text{-}multi}$ (m)	$D_{f,med\text{-}single}$ (m)
Present day without heating	0.35	5.39	0.420	0.279
Present day after 50 years of heating	0.11	5.05	0.011	0.007
Present day after 100 years of heating	0.10	5.02	0.057	0.001

In Table 9-2, we presented the maximum principal stress (S1), intermediate principal stress (S2) and minimum principal stress (S3) that are monitored by the measurement circle installed at the center of the repository rock volume. The increments in the principal stresses by the heating and the fault activation are also listed.

In case of activation of ZFMWNW0809A without the heating, the principal stresses at the repository rock mass dropped after the activation. The resulting principal stress ratios (S1/S3 and S2/S3) are more favorable for the slip of the repository fractures, than in the initial stress field.

In case of activation of ZFMWNW0809A after 50 years of the repository heating, the principal stresses increase due to thermal expansion of the rock mass induced by the repository heating. The increment in the maximum principal stress is the largest. The orientation of the maximum horizontal stress changes to N150°E after 50 years of the repository heating. Such 5° reorientation of the maximum stress could have resulted in different levels of instability of ZFMWNW0809A. This might be the reason for the lowered slip displacement of ZFMWNW0809A. In case of 100 years of the repository heating, the principal stresses in the repository rock mass increase larger than the case of 50 years of heating, and the orientation of the maximum stress changes to N150°E.

The results from the modelling cases demonstrate a possibility that the repository fracture may slip less when an earthquake occurred after the repository rock mass is heated for several tens or hundreds of years. However, more simulation runs and further analyses are required in this issue.

Table 9-2. Local stresses measured (using the measurement circle at the center of the repository rock volume at different stages in the heat and earthquake modelling scenarios (S1, S2, S3: maximum, intermediate, minimum principal stresses; ΔS1, ΔS2, ΔS3: increment (+) and decrement (-) in the stress magnitude after heating/earthquake).

Scenario	Stress (MPa)	Initial stress	After heating	After activation
Earthquake @ZFMWNW0809A	S1	33.7	NA	28.9 (-4.8)
	S2	17.1		14.4 (-2.7)
	S3	8.3		5.9 (-2.4)
	S1/S2	2.0		2.0
	S1/S3	4.1		4.9
	S2/S3	2.1		2.4
	S1 orientation	N145°E		N145°E
Heating + Earthquake @ZFMWNW0809A			50 year	
	S1(ΔS1)	33.7	40.1 (+6.4)	37.3 (-2.7)
	S2(ΔS2)	17.1	22.0 (+4.9)	18.0 (-4.0)
	S3(ΔS3)	8.3	10.0 (+1.7)	4.7 (-5.3)
	S1/S2	2.0	1.8	2.1
	S1/S3	4.1	4.0	8.0
	S2/S3	2.1	2.2	3.8
	S1 orientation	N145°E	N150°E	N145°E
			100 years	
	S1(ΔS1)	33.7	43.6 (+9.9)	40.0 (-3.6)
	S2(ΔS2)	17.1	24.1 (+7.0)	20.5 (-3.6)
	S3(ΔS3)	8.3	10.6 (+2.3)	6.9 (-3.7)
	S1/S2	2.0	1.8	2.0
	S1/S3	4.1	4.1	5.8
	S2/S3	2.1	2.3	3.0
	S1 orientation	N145°E	N150°E	N149°E

10. Discussion

In this Chapter, we compared this 3D modelling study with previous 3D and 2D modelling studies conducted in the past.

Differences between the modelling studies by SKB-Posiva and SSM

Both modelling studies performed by SKB-Posiva and SSM adopted a discrete element model. SKB-Posiva used 3DEC (3D Distinct Element Code) and SSM adopted PFC3D (Particle Flow Code 3D). Despite the similarities in the numerical modelling softwares, there are more differences than similarities between the two studies. The key differences between the two modelling studies are briefly summarized in the table below. Due to these key differences, benchmarking the results of SKB-Posiva studies was not possible.

Table 10-1. Differences in the modelling conditions between SKB-Posiva 3DEC studies and SSM PFC3D study.

	SKB-Posiva studies (3DEC)	SSM studies (PFC3D)
Fault representation	Planar and rectangular single fault plane with no coupling to the Forsmark site	Non-planar multiple fault planes with strong coupling to the Forsmark site
Earthquake event simulation	Initiated fault rupture at a predefined hypocenter and programmed to propagate outward to fault edges	Entire fault plane rupture by sudden release of the strain energy
Slip pattern	Parabolic (maxium slip at fault centre)	Triangular and asymmetric in general, but locally heterogeneous (increase/drop at fault-fault intersection)
Repository fracture	Isolated and uniformly spaced and oriented, planar fractures and fracture extension not allowed	Randomly oriented and spaced, intersecting non-planar fractures and fracture extension allowed

Large fracture slip induced by fault activation

In the earthquake modelling cases in this study, the results show that some of the fractures in the DFN slip more than the slip of the activated faults. It cannot be ruled out that the secondary displacement of the fractures was over-estimated. Like in other numerical codes, the results depend on mesh size in case of FEM (Finite Element Model), and particle (or block) size in case of DEM (Discrete Element Model). However, the reason for a large fracture slip induced by nearby fault activation could be that the fractures are represented heterogeneously and intersecting one another. It is possible that large secondary slip can occur on fractures located in a highly stressed area and oriented favorably for slip due to dynamic and static effects resulting from a fault rupture.

One additional model run was performed where the fractures are isolated and uniformly spaced as shown in Figure 10-1. In this reference model, 56 fractures that are dipping 45 degrees are implemented at the depth of the repository (-500 m) and their coseismic slips induced by the activation of ZFMA3 (blue trace) under the present day reverse faulting *in-situ* stress condition are investigated.

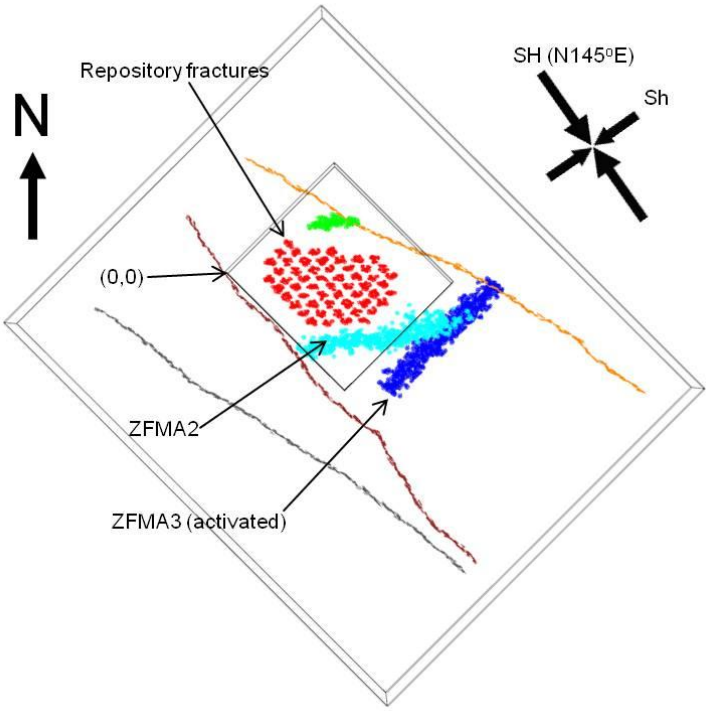

Figure 10-1. Top view of the reference model with 56 uniformly spaced fractures (red) of which the centers are located at the depth of the repository (-500 m) and favorably oriented for slip (striking in the orientation of maximum horizontal stress and dipping 45 degrees) by activation of ZFMA3 (blue trace) under present day reverse faulting *in- situ* stress condition.

The slip of the activated fault is 0.47 m, resulting in Mw 5.76. The secondary fracture slips induced by a fault rupture were found, in general, to be decreasing with the distance from the rupture source. Such trend can be seen in Figure 10-2b. Those distant fractures from ZFMA3 slip relatively less than those close to the rupture source (black star). The largest slip occurred at the fractures located underneath ZFMA2 (Fig.10-2a), and the movement of ZFMA2 is triggered by the primary fault activation (ZFMA3) as two deformation zones are connected. This result demonstrates that fault-fault connectivity and their triggered movement should be also considered in the seismic hazard assessment.

In Figure 10-3, we compare the two data sets. The red data set are the repository fracture slips resulting from activation of ZFMA3 under present day reverse faulting stress condition. The gray data set is the results of the reference modelling, where the fractures are isolated. The distributions of both data sets show that the fracture slips decrease generally with the distance from the seismic source. However as it shown in the graph, the slips of the repository fractures embedded in a DFN are generally larger than the slip of the isolated fractures.

The trend with decreasing secondary slip with increasing distance from the primary fault becomes more distinct if the fractures are isolated and in case of a single distant fault activation. When fractures are randomly oriented and intersecting, there are more uncertainties to consider for the analysis of fracture slip. In this study with random DFN set, it is difficult to analyze the dependency of the fracture length, orientation, and distance from rupture source on the induced secondary slip. Moreover, due to presence of neighboring faults connected to the primary fault and its effect by triggered movement, the level of uncertainty increases.

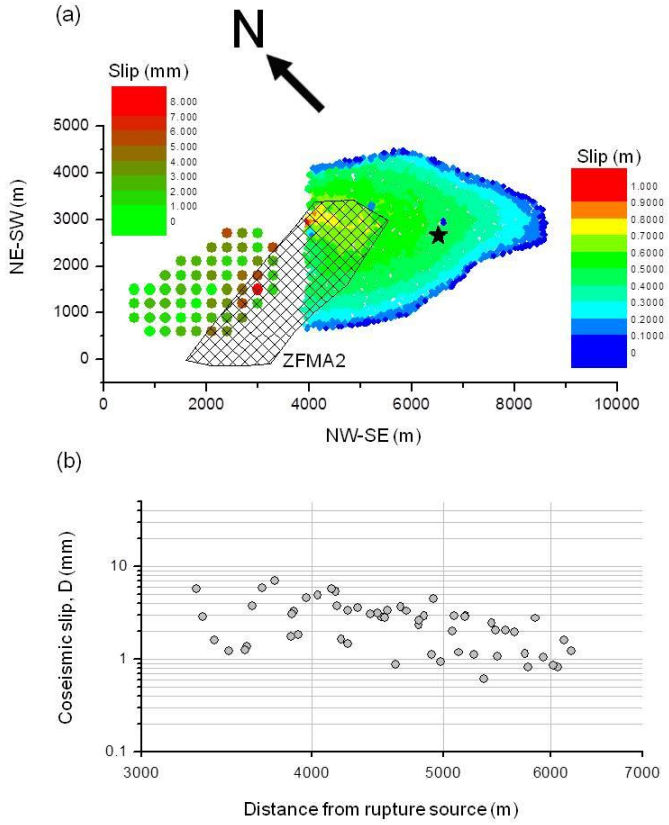

Figure 10-2. (a) Coseismic slip of the 56 repository fractures (left color bar, in mm-scale) induced by activation of ZFMA3 (right color bar, in m-scale) and (b) distribution of induced repository fracture slip with respect to the distance from the rupture source centre (black star). In (a), top view of ZFMA2 is shown by the black polygon.

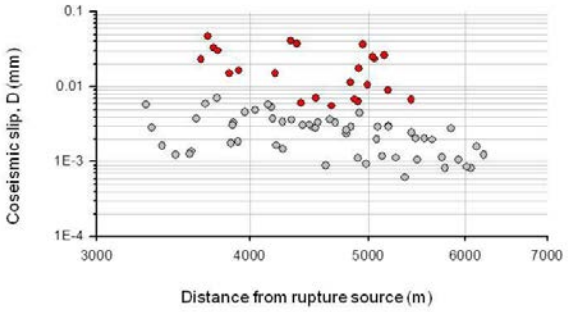

Figure 10-3. Distribution of the induced repository fracture slip with respected to the distance from the rupture source (red: ZFMA3 activation under present day reverse faulting stress condition; gray: ZFMA3 activation in the reference model).

Advantages and disadvantages of more complex 3D model and simpler 2D model

The 2D modelling studies of Yoon et al. (2014, 2016a, 2016b, 2017) has been extended to a 3D setting in this study.

One advantage of the 3D modelling study of this kind is that the data of rupture area vs. activation magnitude can be directly compared with the natural earthquake fault relation as shown in Figure 8-16. This result enhances the credibility of the modelling method by demonstrating that the modelled fault rupture source parameters follow the natural earthquake fault scaling relation.

Secondly, those gently dipping faults can be better represented in 3D. The impact of those gently dipping faults to the repository safety is considered important, especially during and after the deglaciation when the *in-situ* stress field at the depth of the repository becomes more unstable. A few gently dipping faults and their impacts to the repository fractures were analyzed in the 2D modelling (Yoon et al. 2014). However, the faults and the fractures were treated as line source and the impact of the full fault size was not properly taken into consideration. The 2D modelling results could only be compared with the natural earthquake fault data after certain assumptions on the fault length and fault width were established.

It was found during this 3D modelling study that the model generation and simulation run took significantly longer time compared to the 2D modellings. The reason could be that the 3D model is larger and contains much more particles and fractures in the DFN compared to 2D. However, this computation related challenges could be overcome by using newer version of the software PFC v5.

11. Recommendations for further study

In this Chapter, we continue discussion on several issues that we suggest for further study.

Width of damage zone of earthquake hosting deformation zones

A typical fault zone structure comprises a highly deformed core surrounded by a damage zone composed of rocks with higher fracture density and lower elastic modulus than the host rocks (Fig.11-1a). In mature faults, damage zones are 100 m to 400 m wide and have between 20% and 60% wave velocity reductions relative to their host rock (Huang and Ampuero 2011).

Width of damage zone, or sometimes called process zone, is a function of the length of the faults. Scaling data of the fracture (fault) process zone from laboratory and natural faults are presented in Zang and Stephansson (2010) in Figure 11-2. It is the general conclusion that the width of the process zone (and also the fracture toughness) scales with the length of the fracture.

SKB (2011) presented the information of the deformation zones intersecting an area corresponding to a 5 km radius circle centre at Forsmark. Table 11-1 lists the trace length, strike, dip, width of fault damage zone and estimated maximum magnitude using regressions in Wells and Coppersmith (1994) of five deformation zones modelled in the Regional Scale Model, except ZFMA1 (see Fig.4-2).

Table 11-1. Deformation zones modelled in the Regional Scale Model.

Deformation zone	Trace length (m)	Strike	Dip	Damage zone width (m)	Estimated maximum moment magnitude
ZFMA2	3,987	80	24	23	5.8
ZFMA3	3,234	46	22	22	5.7
ZFMWNW0001 (Singö)	30,000	120	90	200	6.8
ZFMNW0003 (Eckarfjärden)	30,000	139	85	53	6.8
ZFMWNW0004 (Forsmark)	70,000	125	90	160	7.2

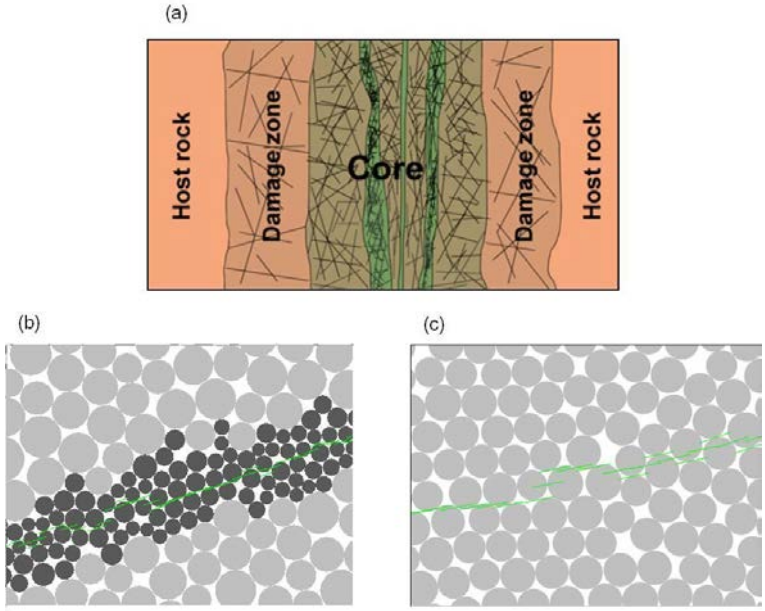

Figure 11-1. (a) Fault zone structure (Munier and Hökmark 2004), (b) PFC2D modelling of a fault zone (grey particles: host rock, dark grey particles: damage zone, green: core fractures modelled by smooth joints), and (c) alternative way of modelling a fault zone adopted in this study.

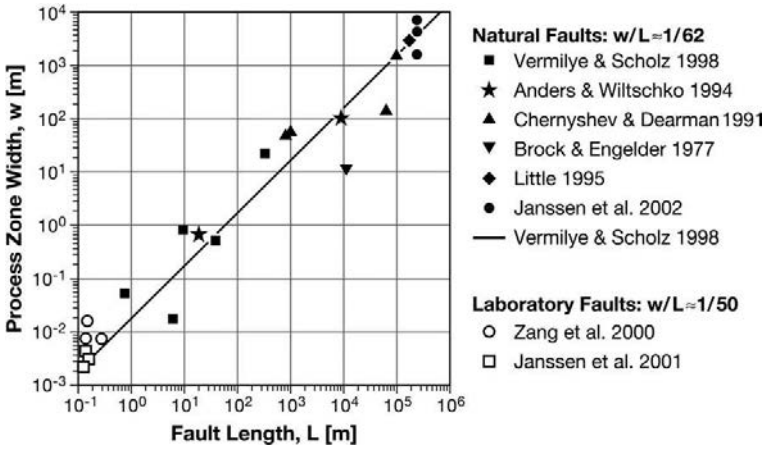

Figure 11-2. Relation between fracture length and width of process zone (damage zone) by Zang and Stephansson (2010).

In the 3D modelling of the deformation zones in both Local and Regional Scale Models, the damage zone of the faults is not explicitly modelled. This was discussed in the early stage of this study to model the damage zone of several large deformation zones, especially those included in the Regional Scale Model. The way to mimic the damage zone in PFC modelling is to distribute smaller sized particles close to the fault core fractures that are represented by the smooth joints as shown by the grey particles in Figure 11-1b. The stiffness and strength of the bonds at the contacts of the grey particles should be usually lower than those properties assigned to the contacts of the light grey particles which mimic the host rock mass. Such explicit modelling of the damage zone is not adopted in this study due to technical difficulty in handling a few millions of particles in one single model run. However,

as an alternative approach, due to step-over structure in representing a deformation zone using smooth joints (Fig.11-1c), structural heterogeneity was to some extent modelled.

Realistic representation of a fault damage zone is important as damage zone thickness has significant effects on earthquake rupture, seismic wave radiation and ground motions (Spudich and Olsen 2001). For further study, we suggest that the faults, at least limiting to a few major deformation zones, e.g. ZFMWNW0001, are modelled by explicitly mimicking the damage zone. Using a continuum based code, FLAC3D, Cappa et al. (2014) investigated the effect of pre-damaged state of the medium on the earthquake fault slip distributions. They found that a triangular and asymmetric slip profiles (Fig.8-24) can only be reproduced when a laterally heterogeneous pre-existing damage zone surrounds the ruptured faults. The highest on-fault slip develops in the most compliant region of the damage zone, and not necessarily at the earthquake hypocenter (red star), and the coseismic slip decreases in zones of stiffer damage (higher Young's modulus, Fig.11-3). The study by Cappa et al. (2014) emphasizes that off-fault pre-existing damage should be considered for a better description of earthquake ruptures.

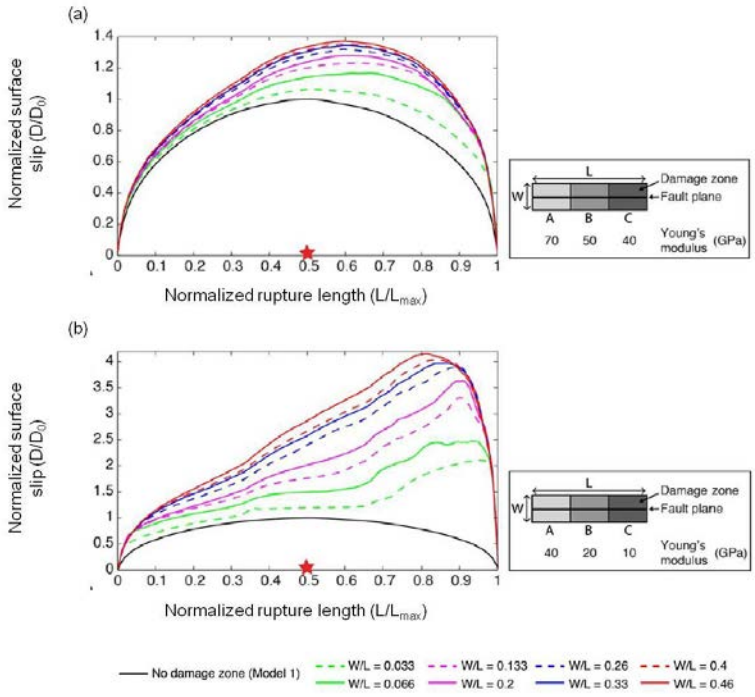

Figure 11-3. Calculated earthquake slip profiles at the surface as a function of rupture length (normalized) for a fault surrounded by a rectangular damage zone (from Cappa et al. 2014).

Having damage zone explicitly modelled is important for assessment of seismic hazard study of this kind, associated with fault displacement, i.e. PFDHA (Probabilistic Fault Displacement Hazard Assessment) of DFDHA (Deterministic Fault Displacement Hazard Assessment) where the coseismic slip profile of a fault hosting an earthquake event is used in the seismic design and performance assessment of key structures, e.g. pipe lines where a fault trace runs through (Cheng and Akkar 2017) or long deposition tunnels in a nuclear waste repository.

In case when a earthquake fault slip profile is estimated by a numerical code which is not able to take into account of fault damage zone, the slip profile of an earthquake fault will always show parabolic profile (black curve in Fig.11-3). The parabolic profile always gives the maximum displacement at the center. However, as pointed out by Cappa et al. (2014), and demonstrated in this study in Figure 8-23, a fault in nature is not planar and always intersected by neighboring faults and has complex and heterogeneity characteristics (e.g. step-over structure) in the off-fault direction, and therefore the slip profile is triangular, asymmetric and locally heterogeneous with sharp increase and drop of displacement especially at the fault intersections. For PFDHA or DFDHA, the results of hazard assessment could be misleading when the location of the maximum fault slip is falsely estimated.

Earthquake M>7

The magnitudes of the earthquake events simulated in this study are all under M<7 (see Table 8-7). These magnitudes are larger than those simulated in the 2D modelling studies of Yoon et al. (2014, 2016a, 2016b, 2017). Generation of Regional Scale Model which extends in length to maximum 16.5 km enabled modelling large major deformation zones, e.g. ZFMWNW0001. However, as documented in SKB (2010), the trace lengths of the major deformation zones forming the tectonic lense (Fig.3-3), e.g. ZFMWNW0001, ZFMNW0003, FZMWNW0004, are larger than the size of the Regional Scale Model. Therefore, it is beyond the scope of this study to investigate the effect of Mw >7 earthquake.

Horizontal stress orientation

In all the modelling cases, we assumed that the orientation of the maximum horizontal stress is N145°E, and does not change during the glaciations (forebulge, ice cover retreat). However, there are a few studies suggesting suggested that the glacial isostatic processes can lead to a totally new geodynamic regime with new orientation of the horizontal stresses (Mörner 2003, 2004). We suggest that more numerical modelling cases be conducted to investigate the effect of change in the maximum horizontal stress orientation on the repository fracture response to different earthquake sources. This should be an important issue to a seismic hazard assessment, as deviation from the suggested orientation of maximum horizontal stress, N145°E, could results in instability other deformation zones, such as ZFMENE0060A and ZFMENE0062A (see Fig.4-2), that are considered stable under the present day *in-situ* stress condition.

Discrete Fracture Network

The DFN embedded in the both models (Local Scale and Regional Scale) is one specific set of DFN among 10 realizations. To draw more general conclusions, we recommend additional simulations using other DFN realizations. Also, the mechanical properties of the fractures may be differently calibrated by taking different scaling laws for stiffness and length relations. We recommend using different DFN sets where only those fractures cutting the repository depth are embedded. This is to see the effect of level of fracture connectivity. As the DFN set we used here extends to the model surface, relatively large induced slip of the fractures at shallow depth could have further induced the slip of the fractures at the repository depth.

12. Conclusions

In this numerical modelling research project, we investigated the impacts of three possible scenarios relevant to the safety of the proposed underground repository at Forsmark Sweden for final disposal of spent nuclear fuels. For safety assessment of the repository, we focus on rock fracture shear displacements induced by: (1) heat generated from the canisters containing the spent nuclear fuels, (2) earthquake events occurring at nearby deformation zones, (3) earthquake events occurring at nearby deformation zones during the time when the repository is under heating.

A three-dimensional discrete element modelling code, Particle Flow Code 3D v4 (PFC3D v4) is chosen for the simulation. The code enables modeling of thermo-mechanical coupled process (conductive heat flow, resulting rock expansion and therefore thermal stress) and dynamic fracturing process (seismic wave generated from a rupturing source propagates and attenuates). Moreover, the code enables implementation of discrete fracture network in a heterogeneously modelled rock mass. Therefore, a discrete fracture embedded in the model is also heterogeneously represented.

We studied the possible impacts of heating to the repository fracture system. To do so, we developed a thermal-mechanical coupled simulation workflow and conducted two end-member scenarios: deposition of all waste canisters and closure at the same time, deposition of waste canisters in panel-by-panel sequence. We studied the possible impacts of earthquake events occurring at large deformation zones near the repository site. To simulate an earthquake event with magnitude close to 6 (or larger), we generated a large geological model of the Forsmark site where the major deformation zones are included and represented heterogeneously. In the earthquake modelling scenarios, the considered time span extends to 70k years from present to take into account of possible changes in the *in-situ* stress fields affected by future glaciation and deglaciation. Also, we studied the impact of an earthquake event during the time when the repository is under heating.

It should be noted that all the results of earthquake scenarios assume activation of faults that are close to the repository site (hypocenter distance < 5 km from the repository rock volume) of which the occurrence probability is very low. It implies that the modelling results in this study may serve for the most conservative level of seismic hazard and risk assessment.

Followings are the conclusions drawn from this study.

(1) The rock fractures modelled by PFC3D in this study have a multiple segmented structure and the shear loading induced displacement distribution deviates from parabolic profile that is modelled in an elastic continuum model.

(2) The heating induces shear displacements of the repository fractures. Rapid slip increase is observed during 50-100 years after start of heat release and shows slow decrease after 200 years. Due to fracture dilation, shear displacements are irreversible. The rock fractures that are located within the repository panels show almost no movements in the long term, whereas those outside the panel show steady increase.

(3) Under the present day *in-situ* stress condition at Forsmark site, an earthquake event occurring at fault ZFMWNW0809A (surface trace length: 3350 m) has a much more significant impact to the repository fractures than an earthquake event occurring at ZFMWNW0001 (Singö) deformation zone (surface trace length: 30 km). This is due to the fact that ZFMWNW0809A is located closer to the repository volume.

(4) It is found that the effect of glaciations and deglaciation have impacts to the repository safety. Under the effect of fore-bulging occurring in front of the approaching ice cover (during glacial period), the *in-situ* stress state becomes more anisotropic, which leads to higher instability potential for those steeply dipping deformation zones. Under this stress condition, the results show that the activation magnitude of ZFMWNW0001 (Singö) deformation zone increases from moment magnitude (Mw) of 6.05 (present day anisotropic stress field) to Mw 6.15 (higher anisotropic stress field formed by the effect of fore-bulging in front of the ice sheet). Under the effect of retreating ice sheet (during deglaciation), the *in-situ* stress state becomes more favorable for reverse faulting, which leads to higher instability potential for those gently dipping deformation zones. Under this condition, the results show that the activation magnitude of ZFMA3 slightly increases from Mw 5.75 to Mw 5.85.

(5) The impact of an earthquake event occurring during the early time of repository heating (50-100 years) can be less than the impact of an earthquake without the repository heating, due to the stress field disturbed by the heating. However, further studies are needed to draw a more conclusive statement.

(6) The scaling parameters of the simulated fault rupture agree well with the presented earthquake fault empirical scaling relations. Coseismic slip distributions of the activated faults show triangular and asymmetric pattern and sharp increase/drop of displacements especially at the locations of intersection with neighboring faults. The results show high resemblance to the observations of slip distribution of natural earthquake faults. The results demonstrate that the workflow we developed for simulation of dynamic fault rupture (earthquake event) on the basis of discrete element model and PFC3D v4 well capture the characteristics of the natural earthquake faults.

13. Acknowledgement

We would like to thank the Reference Group, Prof. Dr. Ove Stephansson (KTH & GFZ), Prof. Dr. Hilmar Bungum (NORSAR), Prof. Dr. Fabrice Cotton (GFZ) for their comments on the report and discussion on the results of this study. We thank Dr. Joel Geier (Clearwater Hardrock Consulting) for providing the DFN data sets. We thank Dr. Oliver Heidbach (GFZ) for his support in preparing the mesh data sets for the fault structure modelling. We are grateful to Dr. Flavio Lanaro who was formerly at SSM and developed the project. We are also grateful to Dr. Carl-Henrik Pettersson (SSM) for the comments and administrative support from SSM in finalizing the project.

14. References

Belardinelli ME, Cocco M, Coutant O, Cotton F. 1999. Redistribution of dynamic stress during coseismic ruptures: Evidence for fault interaction and earthquake triggering. J Geophys Res 104, 14925-14945.

Bödvarsson R, Lund B, Roberts R, Slunga R. 2006. Earthquake activity in Sweden Study in connection with a proposed nuclear waste repository in Forsmark or Oskarshamn, SKB R-06-67, Swedish Nuclear Fuel and Waste Management Co.

Cappa F, Perrin C, Manighetti I, Delor E. 2014. Off-fault long-term damage: a condition to account for generic, triangular earthquake slip profiles. Geochem Geophys Geosyst 15, 1476-1493.

Cheng Y, Akkar S. 2017. Probabilistic permanent fault displacement hazard via Monte Carlo simulation and its consideration for the probabilistic risk assessment of buried continuous steel pipelines. Earthq Eng Struct D 46, 605-620.

Choi JH, Jin K, Enkhbayar D, Davvasambuu B, Bayasgalan A, Kim YS. 2012. Rupture propagation inferred from damage patterns, slip distribution, and segmentation of the 1957 Mw 8.1 Gobi-Altay earthquake rupture along the Bogd fault, Mongolia. J Geophys Res 117, B12401

Claesson J, Probert T. 1997. Thermoelastic stress due to a rectangular heat source in a semi-infinite medium – Application for the KBS-3 repository. SKB Technical Report 97-26, SKB Swedish Nuclear Fuel and Waste Management Co.

Cowie PA, Scholz CH. 1992. Displacement-length scaling relationship for faults: data synthesis and discussion. J Struct Geol 14, 1149-1156.

Dedecker F, Cundall P, Billaux D, Groeger T. 2007. Evaluation of damage-induced permeability using a three-dimensional Adaptive Continuum/Discontinuum Code (AC/DC). Physics and Chemistry of the Earth 32, 681-690.

Fälth B, Hökmark H, Munier R. 2010. Effects of large earthquakes on a KBS-3 repository – Evaluation of modelling results and their implications for layout and design. SKB TR-08-11, SKB Swedish Nuclear Fuel and Waste Management Co.

Fälth B, Hökmark H. 2011. Modelling end-glacial earthquakes at Olkiluoto. Posiva Working Report 2011-13, Posiva Oy Finland.

Fälth B, Hökmark H. 2012. Modelling end-glacial earthquakes at Olkiluoto. Expansion of the 2010 study. Posiva Working Report 2012-08, Posiva Oy Finland.

Fälth B, Hökmark H, Lung B, Mai PM, Robers R, Munier R. 2015. Simulating earthquake rupture and off-fault fracture response: application to the safety assessment of the Swedish nuclear waste repository. Bull Seismol Soc Am 105, 134-151.

Glamheden R, Hansen LM, Fredriksson A, Bergkvist L, Markström I, Elfström M, 2007. Mechanical modelling of the Singö deformation zone – Site descriptive modelling Forsmark stage 2.1. SKB R-07-06, Swedish Nuclear Fuel and Waste Management Co.

Hanks TC, Kanamori H. 1979. A moment magnitude scale. J Geophys Res 84, 2348-2350.

Hökmark H, Lönnqvist M, Fälth B. 2010. THM-issues in repository rock Thermal, mechanical, thermo-mechanical and hydro-mechanical evolution of the rock at the Forsmark and Laxemar sites. SKB TR-10-23, Swedish Nuclear Fuel and Waste Management Co.

Huang Y, Ampuero JP. 2011. Pulse-like ruptures induced by low-viscosity fault zones. J Geophys Res 116, B12307.

Hudson JA, Cosgrove JW. 1997. Integrated structural geology and engineering rock mechanics approach to site characterization. Int J Rock Mech Min Sci 34, Paper 136.

Kim YS, Peacock DCP, Sanderson DJ. 2004. Fault damage zones. J Struct Geol 26, 503-517.

Lanaro F, Brewith R, Brunk J, Carlvik N, Hedberg B, Hedberg B, Mörtberg A, Ragnarsdotter Thor H, Zika H. 2015. Safe and responsible management of spent nuclear fuel and radioactive waste in Sweden. SSM Report 2015:32, Swedish Radiation Safety Authority.

Leonard M. 2010. Earthquake fault scaling: self-consistent relating of rupture length, width, average displacement, and moment release. Bull Seismol Soc Am 100, 1971-1988.

Lund B, Schmidt P, Hieronymus C. 2009. Stress evolution and fault stability during the Weichselian glacial cycle. SKB TR-09-15, SKB Swedish Nuclear Fuel and Waste Management Co.

Manighetti I, Campillo M, Sammis C, Mai PM, King G. 2005. Evidence for self-similar, triangular slip distributions on earthquakes: Implications for earthquake and fault mechanics. J Geophys Res 110, B05302.

Martin CD. 2007. Quantifying in situ stress magnitudes and orientations for Forsmark. Forsmark state 2.2., SKB R-07-26, Swedish Nuclear Fuel and Waste Management Co.

Mas Ivars D, Pierce ME, Darcel C, Reyes-Montes J, Potyondy DO, Young RP, Cundall A. 2011. The synthetic rock mass approach for jointed rock mass modelling. Int J Rock Mech Min Sci 48, 219-244.

Mas Ivars D, Bouzeran L. 2013. Final report on Synthetic Rock Mass (SRM) Fragmentation Analysis – Appendix 2 – Vein Calibration, El Teniente, Codelco.

McCalpin J. 2013. Seismology – Post-glacial seismicity and paeloseismology at Forsmark Initial review phase. SSM Technical Note 2013:34, Swedish Radiation Safety Authority.

Milliner CWD, Sammis C, Allam AA, Dolan JF, Hollingsworth J, Leprince S, Ayoub F. 2016. Resolving fine-scale heterogeneity of co-seismic slip and the relation to fault structure. Scientific Report 6, 27201.

Morris JP, Jocker J, Prioul R. 2013. Exploring alternative characterizations of fracture stiffness and their respective scaling behaviors, In: Proc of the 47th US Rock Mechanics / Geomechanics Symposium, San Francisco, 23-26 June 2013, paper ARM 13-197.

Mörner N-A. 2003. Paleoseismicity of Sweden – a novel paradigm. Contribution to the INQUA XVI Congress in Reno, Nevada, in 2003. ISBN-91-631-4072-1.

Mörner N-A. 2004. Active faults and paleoseismicity in Fennoscandia, especially Sweden. Primary structures and secondary effects. Tectonophysics 380, 139-157.

Munier R, Hökmark H. 2004. Respect distances, Rational and means of computation, SKB R-04-17, Swedish Nuclear Fuel and Waste Management Co.

Nixon CW, Sanderson DJ, Dee SJ, Bull JM, Humphreys RJ, Swanson MH. 2014. Fault interactions and reactivation within a normal-fault network at Milne Point, Alaska. AAPG Bulletin 98, 2081-2107.

Perrin C, Manighetti I, Ampuero J-P, Cappa F, Gaudemer Y. 2016. Location of largest earthquake slip and fast rupture controlled by along-strike change in fault structural maturity due to fault growth. J Geophys Res Solid Earth 121, 3666-3685.

Probert T, Claesson J. 1997. Temperature field due to time-dependent heat sources in a large rectangular grid. SKB Technical Report 97-27, SKB Swedish Nuclear Fuel and Waste Management Co.

Schlische RW, Young SS, Ackermann RV, Gupta A. 1996. Geometry and scaling relations of a population of very small rift related normal faults. Geology 24, 683-686.

Schultz RA, Okubo CH, Wilkins SJ, 2006. Displacement-length scaling relations for faults on the terrestrial planets. J Struct Geol 28, 2182-2193.

Segedin C. 1951. Note on a penny-shaped crack under shear. Proc of Mathematical Proceedings of the Cambridge Philosophical Society. Cambridge Univ Press.

Shen B. 2014. Development and applications of rock fracture mechanics modelling with FRACOD: A general review. Geosystem Engineering 17, 235-252.

SKB. 2011. Long-term safety for the final repository for spent nuclear fuel at Forsmark Main report of the SR-Site project. SKB TR-11-01, Swedish Nuclear Fuel and Waste Management Co.

Spudich P, Olsen K. 2001. Fault zone amplified waves as a possible seismic hazard along the Calaveras fault in central California. Geophys Res Lett 28, 2533-2536.

Stephends MB, Fox A, La Pointe P, Simeonov A, Isaksson H, Hermanson J, Öhman J. 2007. Geology Forsmark Site descriptive modelling Forsmark stage 2.2. SKB R-07-45, Swedish Nuclear Fuel and Waste Management Co.

Stephens MB, Follin S, Petersson J, Isaksson H, Juhlin C, Simeonov A. 2015. Review of the deterministic modelling of deformation zones and fracture domains at the site proposed for a spent nuclear fuel repository, Sweden, and consequences of structural anisotropy. Tectonophysics 653, 68-94.

Wells DL, Coppersmith KJ. 1994. New empirical relationships among magnitude, rupture length, rupture width, rupture area, and surface displacement. Bull Seismol Soc Am 84, 974-1002.

Yoon JS, Stephansson O, Min KB. 2014. Relation between earthquake magnitude, fracture length and fracture shear displacement in the KBS-3 repository at Forsmark Main Review Phase. SSM Technical Note 2014:59, Swedish Radiation Safety Authority.

Yoon JS, Stephansson O, Min KB. 2016a. Modelling of the thermal evolution of the KBS-3 repository at Forsmark and associated induced seismic activity. SSM Technical Note 2016:23, Swedish Radiation Safety Authority.

Yoon JS, Stephansson O, Zang A, Min KB, Lanaro F. 2016b. Numerical modelling of earthquake and induced seismicity under various in situ stress conditions at Forsmark, Sweden, the site for a final repository of spent nuclear fuel. In: Proc of

the 7th Int Symp on In-Situ Rock Stress – RS2016 Symposium, May 2016, Tampere, Finland.

Yoon JS, Stephansson O, Zang A, Min KB, Lanaro F. 2017. Discrete bonded particle modelling of fault activation near a nuclear waste repository site and comparison to static rupture earthquake scaling laws. Int J Rock Mech Min Sci 98, 1-9.

Zang A, Stephansson O. 2010. Stress Field of the Earth's Crust. Springer Netherlands, Springer Science+Business Media B.V.

2019:15

The Swedish Radiation Safety Authority has a comprehensive responsibility to ensure that society is safe from the effects of radiation. The Authority works to achieve radiation safety in a number of areas: nuclear power, medical care as well as commercial products and services. The Authority also works to achieve protection from natural radiation and to increase the level of radiation safety internationally.

The Swedish Radiation Safety Authority works proactively and preventively to protect people and the environment from the harmful effects of radiation, now and in the future. The Authority issues regulations and supervises compliance, while also supporting research, providing training and information, and issuing advice. Often, activities involving radiation require licences issued by the Authority. The Swedish Radiation Safety Authority maintains emergency preparedness around the clock with the aim of limiting the aftermath of radiation accidents and the unintentional spreading of radioactive substances. The Authority participates in international co-operation in order to promote radiation safety and finances projects aiming to raise the level of radiation safety in certain Eastern European countries.

The Authority reports to the Ministry of the Environment and has around 300 employees with competencies in the fields of engineering, natural and behavioural sciences, law, economics and communications. We have received quality, environmental and working environment certification.

Strålsäkerhetsmyndigheten
Swedish Radiation Safety Authority

SE-171 16 Stockholm
Solna strandväg 96

Tel: +46 8 799 40 00
Fax: +46 8 799 40 10

E-mail: registrator@ssm.se
Web: stralsakerhetsmyndigheten.se

Ale Tryckteam AB, Bohus, 2019